Enabling Multidimensional Ion Mobility Separations Using Structures for Lossless Ion Manipulations

Benjamin Zercher

A dissertation

Submitted in partial fulfillment of the

Requirements for the degree of

Doctor of Philosophy

University of Washington

2023

Reading Committee:

Matthew F. Bush, Chair

Frantisek Tureček

Dan Fu

Program Authorized to Offer Degree:

Chemistry

University of Washington

Abstract

Enabling Multidimensional Ion Mobility Separations Using Structures for Lossless Ion Manipulations

Benjamin Zercher

Chair of the Supervisory Committee:

Associate Professor Matthew F. Bush

Department of Chemistry

This dissertation describes the development and application of multidimensional ion mobility (IM) techniques using the modular Structures for Lossless Ion Manipulations (SLIM) architecture. IM is an analytical technique in which charged ions are separated in a neutral background gas under the influence of an applied electric field. IM separates ions based on their size, shape, and charge. IM was paired to mass spectrometry (MS), an analytical technique that determines an ion's mass to charge (m/z) ratio. To provide context for multidimensional techniques described in this dissertation, Chapter 1 provides an overview of next-generation IM instrumentation that enables both multidimensional and ultrahigh-resolution IM separations. The following chapters describe experimental efforts to realize multidimensional experiments on a modular IM instrument that utilizes the Structures for Lossless Ion Manipulations (SLIM) architecture. Chapter 2 investigates the structural stability of native-like protein ions, which are

ions generated from non-denaturing solution conditions that exhibit compact structures that can retain memory of solution-phase structure. Using time-dependent, multidimensional IM experiments, individual charge states of native-like protein ions were mobility-selected and trapped for varying periods of time (up to 14 s). Structural dynamics during ion trapping were probed in a second dimension of IM. While some native-like ions exhibited structural dynamics, the unfolding that was observed was less extensive than complete unfolding, demonstrating that ions can retain memory of the solution-phase structure for remarkably long times in the gas phase. These results inform applications of next-generation IM instrumentation that could potentially separate ions using much longer timescales.

In Chapter 3, a new strategy for multidimensional IM separations on instruments that use electrostatic gradients is presented. In this strategy, the potentials of trapped ions are "reset" between dimensions of IM, which allows for increased flexibility in the application of electrostatic gradients to different regions of the instrument. Potential-resetting experiments were compared to standard tandem IM experiments, which demonstrated that ions are neither lost nor activated in this strategy. We propose to use this strategy on the final implementation of the modular instrument described here, in which the installation of four additional SLIM modules will create a "cyclic" path to enable flexible experiments. As the experiments described herein are performed using electrostatic gradients, it is possible to determine an ion's mobility directly from experimental observables without calibration. The conversion of collision cross section values from nitrogen to estimated helium values is then described in Chapter 4, further increasing the utility in cross-platform comparison of IM results.

Dedication

To Mom and Dad

Acknowledgements

The work presented in this dissertation (as well as the additional research documented elsewhere) would not have been possible without my advisor, Matt Bush. It has been an honor to work with such a brilliant scientist, and he has forever changed how I approach abstract problems. I also want to acknowledge Matt's mentorship in "soft" skills – public presentations, writing, design – and his leadership style that allows researchers to explore different areas. I have always appreciated Matt's dedication to holistic personal development rather than simply assigning tasks to further his own research goals. While on the topic of mentorship, I would also like to acknowledge my mentors from Butler University who were so instrumental in my development as a scientist. I would like to thank Todd Hopkins, my undergraduate research advisor. I will always appreciate his patience and the extensive conversations that were had when the circularly polarized luminescence spectrometer was running. (How do they get the prices at Aldi so cheap?) In reality, I didn't just have one mentor at Butler – I had an entire department who was invested in my success. My recent return to Butler to give a seminar on my graduate research is likely my most cherished moment of graduate school.

To my colleagues in the Bush lab, thank you all for being such a pleasure to work with through the years. To the Bush Lab alumni, I'd like to thank Rae Eaton for her patience in getting me started on this SLIM instrument. Meagan, thanks for both teaching me how to ski and also teaching me how to think critically about my own research. Daniele, thanks for being an early friend when I knew no one in Seattle and also fielding all of my questions about native MS. To current Bush lab members, keep at it. We made it through difficult times during the pandemic, and I feel like the horizons are bright with all of the exciting projects. Theresa, thanks for being a great friend during our shared years in the Bush Lab, and thanks for putting up with my stops to

your office for lengthy chats. And Cosmo says thanks for watching him when I am out of town. To Addison and Bruce, thanks for working with me during the last year. The stress of trying to finish meant I wasn't always at my best or most organized. I am excited to see where you both take this project.

I also would like to acknowledge my collaborators King Yabut and Nina Isoherranen. Although not documented in this thesis, I spent a lot of my final two years of graduate school analyzing fatty acid binding proteins using native mass spectrometry. This was a very engaging project that I would not have worked on had King not reached out via email. I am thankful for King's hard work in supplying protein samples, and for all of the thought-provoking meetings that were brought about by this collaboration – I can't wait to see where the project goes.

Finally, I would be remiss to not acknowledge my family and friends. I knew no one in Seattle when I moved out here to begin research, and I am thankful for the friends who have made this feel much more like home. Collin, Nolan, Michael, Kevin – thanks for the darts, and thanks for the support through this last year as I worked on my thesis. Parker, we came a long way from meeting in the hallway during orientation week, and I think this is just the start to the exciting things we are going to accomplish. I would also like to thank my family for constant positive support, even as my own outlook might have wavered. Amy, thanks for your willingness to come visit, and for coordinating trips home. To my dad, thanks for your weekly encouragement, as well as your visits. To my mom, I miss you every day, and thank you for being an example of resilience, passion, and selflessness. And last but not least, I would like to thank my wonderful girlfriend Allegra. Thanks for instilling in me a newfound confidence, and for pushing me to achieve my goals. I am beyond excited for what our future holds.

Table of Contents

Chapter 1: Enhancing the Depth of Analyses with Next-Generation IM Experiments

This chapter is reproduced with permission from Zercher, B.P.; Gozzo, T.A.; Wageman, AC; Bush, M.F. "Enhancing the Depth of Analyses with Next-Generation IM Experiments." *Annual Review of Analytical Chemistry* **2023.** Copyright 2023 Annual Reviews.

1.1 General Overview

Ion mobility spectrometry, or simply ion mobility (IM), was introduced more than 120 years ago[1] and now boasts a flourishing partnership with its younger sibling, mass spectrometry (MS). IM separates gaseous ions in the presence of an electric field, E, and a buffer gas; the steady-state velocity of the ion, v_D, is proportional to E according to the mobility of the ion, K:

$$K = \frac{v_D}{E} = \frac{L}{t_D E} \tag{1.1}$$

K can be determined from the ion's drift time, t_D, and the length, L, of the separation region. Note that t_D refers to the residence time of the ion in the separation region; researchers often report the arrival time (t_A) of ions at a detector that is located distal to the separation region [2]. Within the low-field limit, the ion-neutral collision cross section, Ω, can be determined from K using the Mason-Schamp equation[3,4]

$$\Omega = \frac{3ez}{16N}\left(\frac{2\pi}{\mu k_B T}\right)^{1/2}\frac{1}{K} \tag{1.2}$$

where e is the elementary charge, z is the charge state, N is the drift-gas number gas density, μ is the reduced mass of the ion-drift gas pair, k_B is the Boltzmann constant, and T is drift-gas temperature. Overviews of the fundamentals of IM are available elsewhere.[2,5] IM continues to be used widely as a standalone technique.[6–8] Technology for IM-MS has advanced rapidly in recent years, as highlighted in several reviews.[2,9–12]

Today, concerted research efforts have pushed IM to the precipice of a new generation of technology, as IM separations now access unprecedented performance and experimental flexibility.[13] To understand today's instrumentation, we provide a summary of selected IM technologies in Figure 1.1. In drift-tube IM, ions experience a uniform electrostatic field established by potentials created by a voltage divider network that are applied to a series of ring electrodes (Figure 1.1A).[14] Using drift-tube IM, Clemmer, Jarrold, Bowers, and Hill, among others, made pioneering contributions to our understanding of the structures of peptide and protein ions from single-component samples.[14–20] The ability of IM to separate similar structures depends on the resolving power, R_p, of the measurement, which exhibits the following relationship for drift-tube IM[3]

$$R_p = \frac{t_D}{t_{FWHM}} \sim \left(\frac{LE}{T}\right)^{1/2} \tag{1.3}$$

where t_{FWHM} is the full width at half maximum of the feature in drift time. Zimmerman and coworkers have reviewed implementations that optimize R_p.[21] Improving the R_p of drift tubes can create additional challenges. For example, increasing L at constant E is associated with greater radial diffusion and decreased transmission, which has since been addressed using electrostatic focusing[22,23] and RF confinement.[24] Increasing L also requires larger instrument footprints and the application of higher potentials due to the relationship between L and E. A complementary way to increase the information content of IM measurements is to increase dimensionality. Clemmer and coworkers pioneered IM-IM-MS, or tandem IM, by interfacing a series of drift tubes using mobility-selective ion funnels.[25,26]

Electrodynamic separations enable alternative strategies to increase the performance of IM measurements. In traveling-wave IM, a series of potentials is propagated down the length of an IM cell as a function of time (Figure 1.1C). Individual waves "push" ions down the length of

the device until the drag from gas collisions forces ions to "roll over" the wave. The propensity of ions to experience roll-over events decreases with increasing *K*, thus enabling mobility-dependent separations.[27] In contrast to drift-tube IM, absolute voltages depend on the amplitude of the traveling wave, rather than *L*. Another electrodynamic strategy is trapped IM spectrometry (TIMS), which utilizes a directional flow of gas to propel ions and a countering *E* gradient that impedes their progress (Figure 1.1F).[28] Under those conditions, ions reach an equilibrium position that depends on *K*. As the gradient is relaxed, ions are eluted in order of decreasing *K*.[29] The performance of the separation depends strongly on the rate of gradient change, *i.e.*, the scanning speed; TIMS can achieve high performance R_p without lengthening the physical length of the cell.[28]

Drift-tube, traveling-wave, and trapped IM were all first implemented using cells with a radial axis of symmetry (Figure 1.1). In addition to electrodynamic fields, recent IM devices have also benefited from alternative geometries. Structures for Lossless Ion Manipulations (SLIM) introduced a planar geometry using mated pairs of printed circuit boards; implementations have utilized both electrostatic[30] (Figure 1.1B) and traveling-wave[31] (Figure 1.1E) separations. The recently introduced Cyclic IM system makes innovative use of elements with planar and radial geometries.[32] The combination of new architectures and electrodynamic strategies forms the basis of next-generation IM instrumentation, pushing the boundaries of separation performance for biomolecular applications.

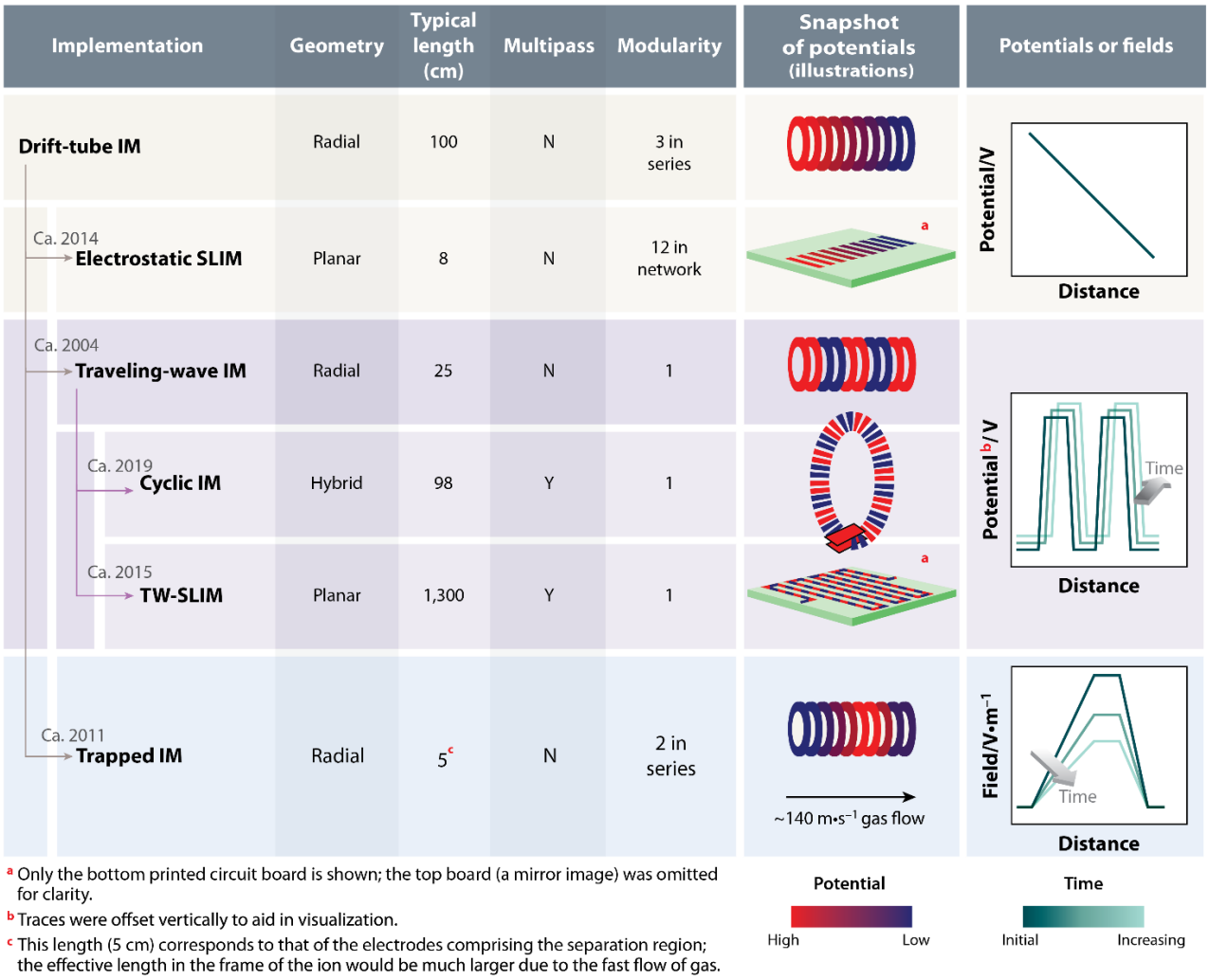

Figure 1.1. Summary of selected implementations of IM, including (A) drift tube IM, (B) electrostatic Structures for Lossless Ion Manipulations (SLIM)[30], (C) traveling-wave IM[27], (D) cyclic IM (cIM)[32], (E) traveling-wave SLIM [31], and trapped IM spectrometry (TIMS)[129]. To enable higher-performance experiments, technologies that have followed on from drift tubes have applied innovations in applied electric fields, electrode geometries, the ability to subject ions to multiple passes through the separator, and increased modularity/dimensionality. The years adjacent to the arrows correspond to the publications references above and do not consider earlier disclosures in patents or conference presentations.

IM performance is often reported using single-peak resolving power (R_p):

$$R_p = \frac{x}{\Delta x} \tag{1.4}$$

where x is the peak centroid and Δx is the width of the peak, usually defined as the full width at half-maximum (fwhm). Traditionally, the independent variable of the experiment, drift time, has been used to define R_p in IM, *i.e.*, R_p^t.[33] However, the broader adoption of electrodynamic separations has complicated the evaluation of this figure of merit. For one, electrostatic separations exhibit a linear relationship between t_D and K^{-1}, whereas electrodynamic separations exhibit a nonlinear relationship between those quantities. Many researchers report resolving powers in the **Ω** space, *i.e.*, R_p^{Ω}; this requires converting t_A to **Ω** using a calibration function.[34] The nonlinear relationship between t_D and **Ω** in a calibration function results in different values for R_p^t and R_P^{Ω}.[34] Additionally, R_p^t is not descriptive of IM separations that utilize electric field scanning, such as TIMS. Alternatively, the peak-to-peak resolution, $R_{p\text{-}p}$, has also been used to describe the separation of two analytes in IM[31,35]

$$R_{p-p} = 2\left|\frac{x_2 - x_1}{\Delta x_2 + \Delta x_1}\right| \tag{1.5}$$

where x_2 and x_1 are the centroid values and Δx_2 and Δx_1 are the widths, often fwhm, of the two peaks, usually in terms of arrival time. As next-generation instrumentation accesses unforeseen separation capabilities, one goal of this review is to provide clarity in the methods used to report resolution for different implementations of IM.

This review will focus on the applications of next-generation IM instrumentation to biomolecular analysis. This review complements recent reviews of fundamentals of the various IM techniques,[5,12,28,36,37] ultrahigh-resolution IM techniques,[21] and multidimensional IM separations.[13] We are motivated by the recent research thrust and commercialization of IM

instruments that redefine IM paradigms and access ultrahigh-resolution separations or multidimensional experiments. Specifically, we will focus on structures for lossless ion manipulations (SLIM), cyclic IM (cIM), and trapped ion mobility spectrometry (TIMS) as applied to a range of applications including glycomics, peptidomics, lipidomics, and proteomics. We will not consider techniques that filter based on mobility, *e.g.*, field asymmetric waveform ion mobility spectrometry (FAIMS, also referred to as differential mobility spectrometry),[38] overtone mobility spectrometry,[39,40] or differential mobility analysis.[41,42]

1.2 Structures for Lossless Ion Manipulations (SLIM)

Structures for Lossless Ion Manipulations (SLIM) uses mated pairs of printed circuit boards,[30] which are more amenable to large, complex designs and rapid prototyping than ring electrode approaches that require extensive fabrication and soldering. The initial implementations of SLIM used electrostatic potentials to separate ions.[30] The voltage gradient in electrostatic SLIM was designed to mimic that of a drift tube, but with planar symmetry. Early simulation-based work characterized the ion dynamics and electric potentials resultant from the interaction of electrostatic fields and superimposed RF potentials used for ion confinement.[43,44] Experimental work then used time-dependent potentials for mobility-resolved ion selection[45] and ion trapping[46,47] on electrostatic SLIM. These initial studies primarily analyzed relatively small molecular ions, *e.g.*, 500 to 1000 *m*/*z*,[46,47] but additional work used these strategies to determine Ω values of native-like protein ions with masses up to 145 kDa.[48] Follow-on studies have included the use of series and networks of modular electrostatic SLIM devices to enable tandem IM,[49] including time-dependent studies of native-like protein ions.[50]

Traveling-wave IM has also been implemented using the SLIM architecture (TW-SLIM).[31] Upon optimization of the traveling-wave profile, the TW-SLIM module maintained lossless transmission while exhibiting a R_p^t of 27.0 for the 622 *m*/*z* Agilent tuning mix ion.[31] Early studies also reported observations of ion "surfing",[27] wherein ions with sufficiently large *K* are transported between two waves at their velocity. Although no separation occurs, narrow peaks result in erroneously high R_p values as even the effects of longitudinal diffusion are limited.[31] Subsequently, separation quality was maintained on a TW-SLIM module that incorporated 90° turns.[51] This enabled the creation of long, compact, serpentine pathlengths; a SLIM module with a 13-m pathlength was introduced that exhibited 5-fold higher resolution compared to commercially available traveling-wave and drift-tube IM systems at that time.[52] To further decouple the pathlength from the overall size of the IM region, an ensuing modification enabled the recycling of ions for multiple passes around the 13-m device, referred to as serpentine ultralong path with extended routing (SUPER) SLIM.[53] The initial study reported peak-to-peak resolution for Agilent tunemix ions of *m*/*z* 622 and 922; after 40 passes on SUPER-SLIM, this yielded a 30-fold higher resolution compared to a commercially available drift tube.[53] Early applications of SUPER SLIM have been reviewed elsewhere.[54] The improvement of resolution afforded by longer separations using TW-SLIM devices is demonstrated in the comparison of different instrumental platforms in Figure 1.2. In Figure 1.2B, isomeric pentasaccharides are separated on the SUPER-SLIM system, revealing further conformational heterogeneity attributed to potential anomerism and sodium protonation sites that was unresolved on other platforms.[55] Additional recent work used SUPER SLIM to characterize drug loads of the heavy and light chains of a monoclonal antibody.[56] Figures 2C and 2D show a comparison between data obtained using drift-tube IM and SUPER-SLIM. Relative to drift-tube IM, SUPER-

SLIM separations better resolved the drug loads of both the light and heavy chains, potentially increasing analytical throughput relative to traditional LC separations.

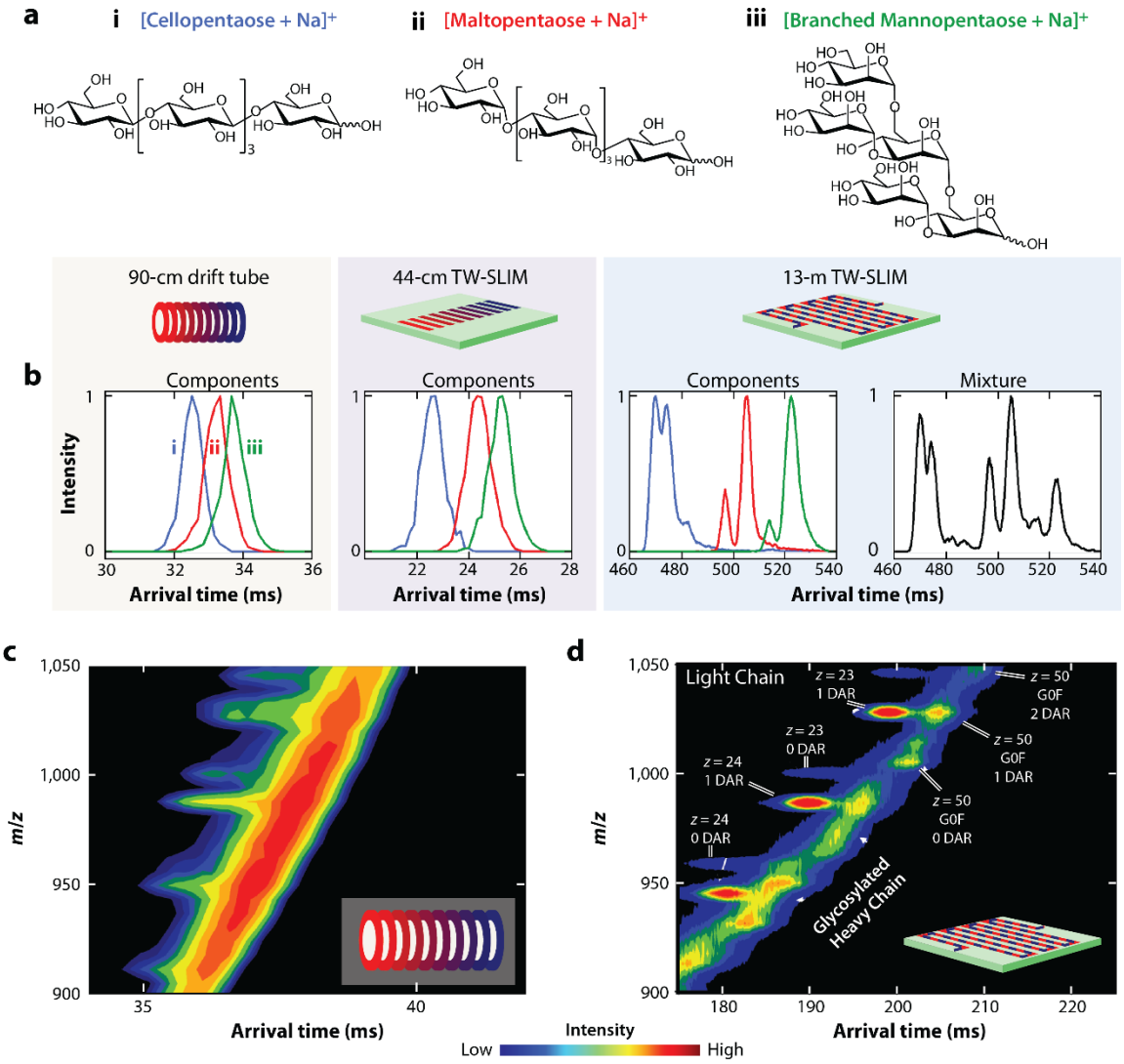

Figure 1.2. (A) Structures of selected isomeric pentasaccharides. The cartoons (reproduced from Figure 1.1) indicate the IM implementation used to measure the (B) arrival-time distributions of selected pentasaccharide ions. From left to right, the distributions were measured using a 90-cm drift tube, a 44-cm TW-SLIM device, a 13-m TW-SLIM device, and the same 13-m TW-SLIM device, respectively. Panel B is adapted

with permission from Reference 55; copyright 2016 John Wiley & Sons, Inc. IMS-MS heatmap of a reduced antibody-drug conjugate on a commercial 1-m drift-tube IM system (C) and a 4.5-m TW-SLIM system (D). Panels C and D are adapted with permission from Reference 56; copyright 2020 American Chemical Society. Minor modifications were made to the heatmap in (D) to clarify labeling. Abbreviations: DAR, drug:antibody ratio; G0F denotes glycosylation with N-linked glycan; IM, ion mobility; MS, mass spectrometry; TW-SLIM, traveling-wave structures for lossless ion manipulations.

One challenge of separations with extremely long pathlengths is that ions experience significant diffusion along the axis of separation; this results in low fluxes of ions that can hinder some experiments. Compression ratio ion mobility programming (CRIMP) was used to compress ions dispersed in time and space by utilizing a traditional traveling wave followed by a "stuttering" traveling wave.[57] This strategy was used in a 99-m separation that resolved peptide epimers of β-amyloid using SUPER SLIM.[58] Although the separation pathlength for recycled ions in SUPER SLIM is theoretically unlimited, the IM resolution is limited by the wrap-around effect, wherein higher *K* analytes begin to overtake lower *K* analytes. To address this, a multilevel SLIM device was constructed; ions are transported to different levels of the device using ion escalators, accessing a separation pathlength of 43.2 m and R_p^{Ω} of 560.[59] This system was then miniaturized such that the multilevel device had a pathlength of 1 m and achieved R_p^{Ω} of 131, which is 1.5x higher than a 78-cm drift-tube IM system.[60]

MOBILion Systems recently launched a system with a 13-m TW-SLIM module aimed at providing both high-resolution and high-throughput separations. On this instrument, isomeric and isobaric compounds that could not be separated by MS alone were separated and exhibited

R_p^{Ω} of more than 200.[61] TW parameters were optimized in terms of R_p while limiting ion surfing; these wave conditions also resulted in the lowest errors in the resulting calibrated Ω values.[61] This commercialized instrument has seen early application in the separation of isomeric gangliosides without the need for additional LC separation, which addresses an analytical bottleneck in runtimes for shotgun lipidomics.[62] This system has also been coupled with LC to quantify post-translational modifications of pharmaceutically relevant peptide therapeutics.[63] Specifically, the addition of the IM dimension enabled the separation of coeluting isomerized aspartic acid-containing peptides as well as a deamidation from a parent mAb peptide, both of which were unresolved by LC.[63] As the resolution and runtime of LC separations are inversely related, this study illustrates the potential utility of high-resolution IM to reduce runtimes for complex separations.

SLIM technologies have also been developed for specific application to glycans, whose characteristics of branching, anomerism, and heterogeneity pose challenges to traditional analysis methods. Rizzo and coworkers have combined TW-SLIM with cryogenic infrared action spectroscopy (cryo-IR) to differentiate and identify glycans. First, a 1.8-m TW-SLIM device with ion recycling capability coupled with a combination cryogenic ion trap/TOF mass spectrometer was used to separate and identify individual components of a mixture of epimers as well as a set of two tetrasaccharide isomers found in human milk.[64] α-$_D$-glucose was mobility separated at different time points to monitor the anomeric conversion to β-$_D$-glucose in real time according to the cryo-IR profiles, enabling the calculation of rate constants k_α and k_β in agreement with literature values.[65] Additionally, a spectral decomposition algorithm was developed to identify component glycans from mixtures, with potential for application to lower resolution mobility separations.[66]

Further instrumental innovations sought to increase the throughput and performance of the IM/cryo-IR workflow. A new instrument was introduced that incorporated a SLIM module with a 2-m on-board accumulation region that increased ion utilization efficiency, followed by a 10-m multipass TW-SLIM device that separated GRGDS and SDGRG ions at R_p^{Ω} values of up to ~1000.[67] Furthermore, principal component analysis was used to decrease the wavenumber range required for fingerprinting, reducing IR acquisitions to as little as 5 s.[67] This instrument was then used to separate, characterize, and identify positional isomers of an N-linked glycan associated with the crystallizable region of IgGs in a 60-m separation.[68] The two closest isomeric peaks in the arrival-time distribution were estimated to differ by 0.2-0.3% in terms of **Ω**, which is below the uncertainty of **Ω** values and precludes a database approach using **Ω** alone.[68] By adding orthogonality to the ultrahigh-resolution IM separation, the partnership of SLIM and cryo-IR offers exciting potential for glycan characterization.

The latest version of this platform also includes on-board trapping regions capable of collision induced dissociation (CID).[69] Following CID, ions can either be recycled for additional IM separation or directly analyzed by cryo-IR or MS.[69] For example, IR spectra of the C-fragment of the human milk oligosaccharide LNnT were compared with those measured for disaccharide standards, which indicated that the anomeric configuration of the glycosidic bond in the C-fragment was preserved during fragmentation.[69] This finding and others illustrate the effectiveness of the database approach: determining the structures of small intact glycans and glycan fragments by comparison to available standards enables the structural elucidation of larger and more complex glycan that usually lack appropriate standards.[70–72] For example, Figure 1.3 illustrates the application of this strategy to N-glycans G0-N and G1.[70] IR spectra of selected Y-fragments of G0-N were compared to relevant standards to determine isomeric identity.[70] The

IR spectra of the G0-N fragments were then used to identify fragments of the G1 glycan produced by post-IM CID (Figure 1.3).[70] The same approach was used to assign anomericity of larger glycans LNnT and maltopentaose by comparing the IR spectra of selected fragments to those of anomerically pure corresponding mass analytical standards.[71] Adding CID to the IM/cryo-IR workflow has enabled bottom-up sequencing and isomer identification of increasingly large glycans with more isomeric possibilities that were previously undifferentiable.

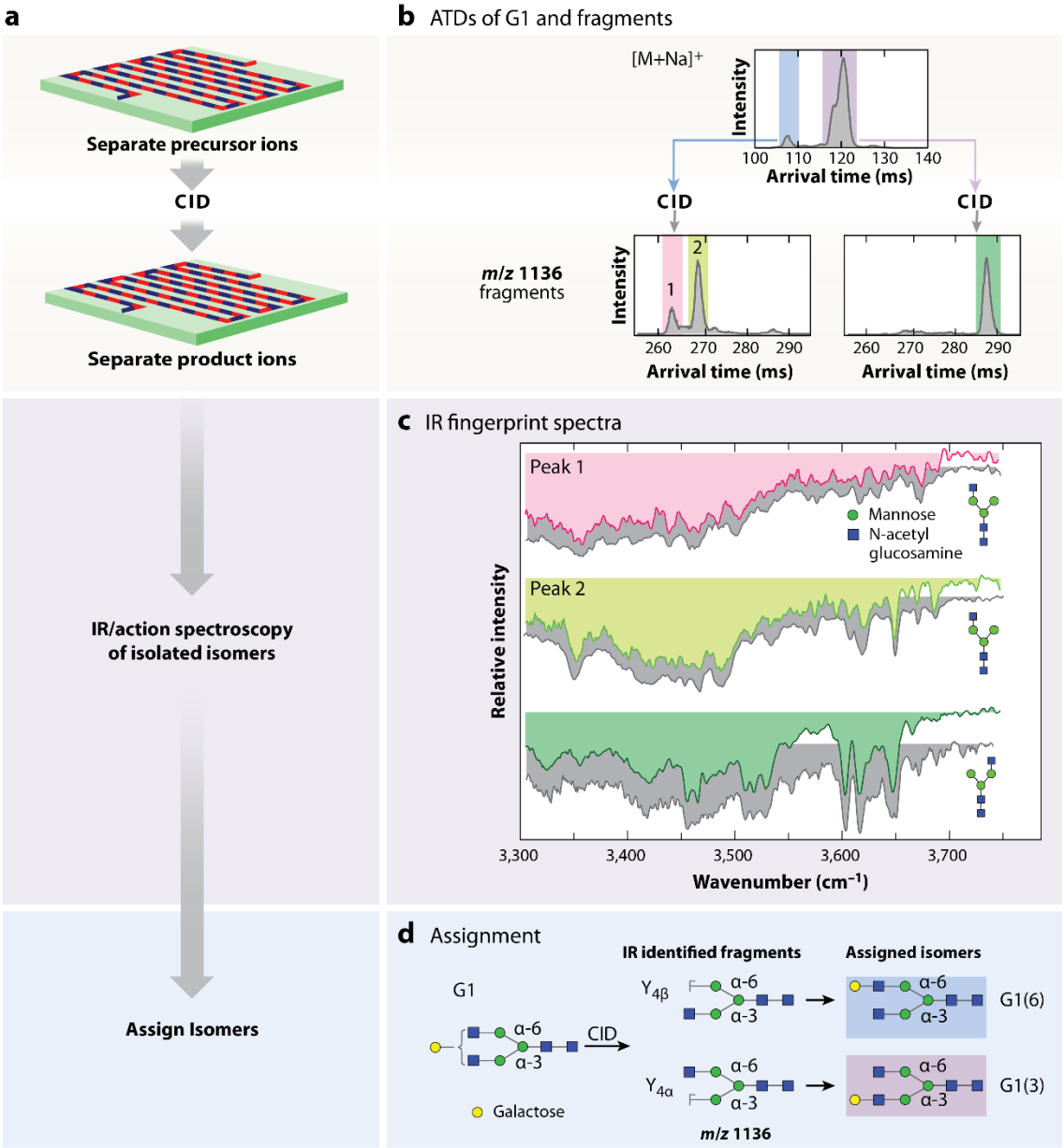

Figure 1.3. (A) Schematic representation of the IM/CID/cryo-IR workflow using the cartoons from Figure 1.1. (B) Arrival-time distribution of precursor G1 separated on a TW-SLIM device with a 10-m pathlength (*top*); peaks highlighted in *blue* and *purple* underwent CID, and *m*/*z* 1136 fragments underwent additional IM separation (*bottom*). (C) IR spectra of mobility-separated *m*/*z* 1136 fragments were recorded and matched to

database spectra (*gray*) of fragments from G0-N. Fragment IR spectra are color-coded to match mobility peaks from the arrival-time distributions for fragments in (B). (D) Structures of the *m/z* 1136 fragments were assigned based on reference spectrum comparison. Isomer structures are highlighted in *blue* and *purple* to match mobility peaks from G1 arrival time distribution in (B). Panels B, C, and D are reproduced with permission from Reference 70; copyright 2022 Royal Society of Chemistry. Abbreviations: ATD, arrival- time distribution; CID, collision-induced dissociation; IM, ion mobility; IR, infrared; TW-SLIM, traveling-wave structures for lossless ion manipulations.

1.3 Cyclic IM (cIM)

The Cyclic IM (cIM) system was introduced by Waters Corp. and incorporates many innovations for next-generation IM experiments.[32] Whereas most IM separations occur along the primary axis of the instrument, the cIM system incorporates a 98-cm, circular TW separator that is orthogonal to the primary axis. The interface of the IM separator and the primary axis consists of a pair of intersecting arrays of planar electrodes that control ion motion in that region. Ions can be subjected to an arbitrary number of passes around the cIM device to access increasingly high-resolution separations. Pre- and post-array ion stores enable mobility-based selection, storage, and activation of ions during various intervals of the experiment. The tunable resolution and flexible experimental modes overcome a traditional limitation of IM technologies, in which the geometry of the instrument imposes constraints on the pathlength and dimensionality of experiments.

The cIM system exhibits significantly improved resolution relative to previously commercialized traveling-wave IM instruments. The first- and second-generation hybrid quadrupole/traveling-wave IM/time-of-flight systems exhibited R_p^{Ω} values near 10[73] and 45[74], respectively. Using cIM, ions of GRGDS and SDGRG exhibited a R_p^{Ω} of ~350 after 16 passes.[32] As with SUPER SLIM, ion wrap-around can hinder the separation of two analytes as the higher-*K* ions overtake lower-*K* ions; mobility-based isolation was used to select SDGRG and subject it to additional passes around the cIM in the absence of GRGDS. R_p^{Ω} increased with the square root of the number of passes, consistent with expectations from theory, and reached ~750 after 100 passes.[32] Many subsequent studies using cIM report estimated R_p^{Ω} values based on those earlier measurements for GRGDS and SDGRG[32], rather than a value based on new observations for the analytes of interest.

The cIM system has been used to analyze many samples that were challenging to resolve using earlier IM systems. Acyl glucuronides are metabolites of nonsteroidal anti-inflammatory drugs (NSAIDs); their degradation yields biosynthetic isomers that are associated with adverse reactions. Unresolved using earlier traveling-wave IM systems, acyl glucuronide isomers were resolved using 8 passes of cIM.[75] Although these isomers can also be separated using HPLC, the cIM system enables much shorter analysis times that are amenable to high-throughput methods for highly reactive metabolites.[75] The cIM system was also used to distinguish α and β anomers of monosaccharides using 5 passes.[76] Chiral systems also present analytical challenges for characterization. In the analysis of a racemic thalidomide mixture, multipass cIM distinguished dimers based on their diastereomeric composition.[77] While unable to distinguish enantiomeric monomers, the ultrahigh resolving power of cIM ($R_p^{\Omega} > 400$) enabled differentiation by a self-

association mechanism, which could be leveraged in other systems to determine optical purity without the need for additional chiral modifiers.[77]

Carbohydrates are the subject of a focused research effort using high-resolution cIM separations to address analytical challenges owing to their high isomeric complexity. The cIM system was used to characterize the arrival-time distributions of oligosaccharides as a function of their group I metal adducts and degrees of polymerization.[78] cIM analyses ranging from 5 to 15 passes revealed that multiple features of the IM distribution arose due to α/β anomerism.[78] Further cIM characterization of oligosaccharides was pursued in the development of a library linking Ω distributions and IR spectra for a fingerprinting approach to determine oligosaccharide ring size.[79] Chemoenzymatically-synthesized disaccharides were characterized using 4 cIM passes to reveal unique features in the Ω distributions.[79] Additional studies on the structure of chemoenzymatically synthesized glycans utilized tandem LC-cIM-MS to identify 8 distinct conformations.[80] In another study, cIM was used to distinguish glycopeptide fragments to characterize the *O*-glycosylation of the SARS-CoV-2 spike protein; 5 passes were needed to separate different sialic acid linkages.[81]

In addition to the enhanced resolution provided by multipass experiments, ions can be subjected to collision-induced dissociation in the trap cell, the transfer cell, or upon injection or reinjection into the cIM region.[32,82] CID-cIM, which refers to activation prior to cIM, can be performed in the trap cell or upon injection into the cIM region. cIM-CID, which refers to activation after cIM, can be performed in the transfer cell. Because no additional separation takes place after activation, the arrival-time distributions of any fragmented or unfolded ions align with the associated precursors.[82] Finally, these approaches can be employed with tandem IM or IM^n, *e.g.*, cIM-CID-cIM, cIM-CID-cIM-CID, and CID-cIM-CID.

Different cIM and CID combinations reveal distinct information. In CID-cIM, fragment ions are separated in IM, and their own arrival-time distributions are recorded. This is useful when isomeric precursor ions yield similar product ion mass spectra, even when the products may have different structures. With pre-cIM fragmentation, isobaric fragments can be associated with specific drift times. For example, from the short reference peptide HLSDSR, an isomeric peptide mix was synthesized with site-specific modifications, including D and L enantiomeric amino acids.[83] With an ultra-performance liquid chromatography compatible method, the peptides were separated well in retention time-drift time space; however, if the peptide modifications were not known *a priori*, their sites could not be identified based on their retention time and t_D alone, or with a cIM-CID approach. With quadrupole selection, CID in the trap, and cIM separation, the shifts of the arrival-time distributions for fragments (relative to fragments of a reference peptide) were used to localize the modification site(s) for seven out of ten cases. Asp/iso-Asp and N-terminal modifications were not readily differentiated in these experiments and the authors suggest that electron-based dissociation methods or additional IM experiments may be beneficial.[83] Overall, this approach could speed up modification characterization in biopharmaceutical research.

Post-cIM activation takes advantage of the high-resolution IM separation of precursors, allowing unique fragmentation patterns to be linked to specific arrival-time distribution features and simplifying MS/MS spectral interpretation. For instance, cIM sufficiently resolved a standard mixture of isomeric methylated ribonucleotide variants, and post-cIM CID produced diagnostic product ions that unambiguously confirmed the location of those modifications.[84] Since methylation is a common post-transcriptional modification, cIM-CID was also applied to a biological mixture generated by exonuclease digestion of RNA from HeLa cells; the methyl-

cytidine isobars and methyl-adenine isobars were identified, highlighting the ability of this method to handle complex epitranscriptomic analyses.[84] Isobaric sets of mono- and disaccharides were also probed with this approach.[85] Because these small saccharides have similar mobilities, a derivatization step further enhanced the IM separation.[85] For each of the doubly derivatized monosaccharide standards, regio- and functional derivatization isomers were resolved by three cIM passes; however, some disaccharides had unresolved isomers due to wrap-around limitations. Diagnostic product ions helped determine derivatization sites from resolved isomers and their alignment with the arrival-time distributions for precursor helped to identify isomers for incompletely resolved features. Similarly, when considering a mixture of the sugar standards, those that were not fully resolved from one another in IM space could be distinguished by the cIM-CID fragment peaks.

Multiple stages of CID and cIM can be exploited to capture more information. For example, a selection of derivatized saccharides had asymmetric arrival-time distributions.[85] To investigate the possibility of interconversion of the mannose derivatives, each feature was isolated in a cIM-CID-cIM experiment and activated on reinjection to the cIM region. The resulting arrival-time distributions were the same as that measured prior to CID, and no additional peaks were observed, indicating the presence of other mannose isomers instead. cIM improves analysis of more complex biological samples in this way as well. *De novo* structural determination of mannosides from crude biological media was performed with the inclusion of heavy oxygen labeling for MS/MS interpretation.[86] cIM-CID elucidated the regioisomerism of the glycosidic bonds in the mannotriose and mannotetraose enzymatic products, whereas cIM-CID-cIM and cIM-CID-cIM-CID identified intrachain anomerism and verified that the anomericity was retained through multiple stages of fragmentation. This workflow revealed both

α and β linkages in the mannotetraose, a novel finding for the product of a single enzyme. Figure 1.4 shows a representation of the cIM-CID-cIM-CID mannotetraose analysis. Work towards *de novo* sequencing of the human milk glycome has also benefited from high resolution IM and multi-stage fragmentation.[87] In addition, because tandem IM shows more capacity for isomer resolution than tandem MS alone, a molecular networking strategy, similar to those used for MS/MS data mining, was employed to better sort oligosaccharides for glycomics.[88] cIM-CID-cIM was applied to a set of 33 penta- and hexasaccharides, and the resulting IM and MS data were used to create two networks. The resulting clusters and subclusters were compared, and the tandem IM network could be justified according to regioisomerism, epimerism, and anomerism, clearly sorting with sensitivity to isomeric structural features.[88] These novel ion manipulation strategies have been applied to the analysis of other carbohydrates[89,90] as well as the analysis of proteins,[91–95] synthetic polymers,[96] and crude oil.[97,98]

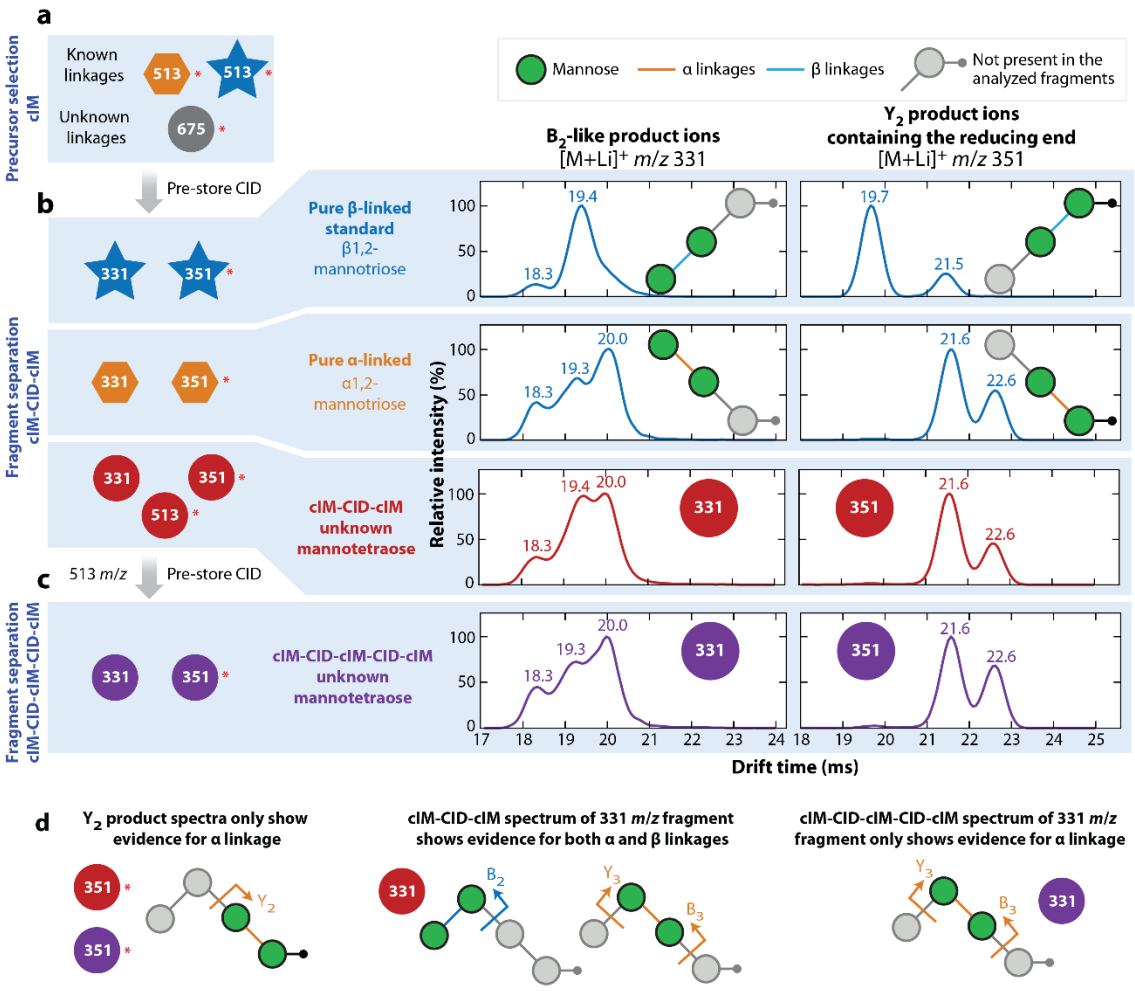

Figure 1.4. cIM-CID-cIM-CID-cIM scheme used to identify linkage anomericity of an intact, unknown mannotetraose (675 m/z). Red asterisks mark ions with the 18O-labeled reducing end. (A) In separate analyses, the intact mannotetraose (675 m/z, circles), a pure β-linked mannotriose standard (513 m/z, stars), and a previously characterized pure α-linked mannotriose (513 m/z, hexagons) underwent initial multipass cIM separations to isolate the major isoforms from contaminants and minor species. These precursor drift-time distributions are not shown. (B) The major isoforms were mobility-selected, then fragmented on reinjection to the cIM region from the pre-store array (CID). All analytes produced fragments at 331 and 351 m/z; these underwent a 4-pass cIM separation. Their

recorded drift-time distributions are shown on the right (cIM-CID-cIM). (C) The mannotetraose also produced a 513 m/z fragment (drift-time distribution not shown) that was mobility-selected and fragmented again, producing ions at 331 and 351 m/z. After another 4-pass cIM separation, drift-time distributions were recorded (cIM-CID-cIM-CID-cIM); they are shown on the right. (D) Assignments of mannotetraose fragments (arrows) and linkages (lines) made based on mobility data and fitting. The cIM-CID-cIM spectrum of 331 m/z fragments contained a mixture of α and β linkages, arising from both B2 fragments and isobaric Y3 + B3 sequential fragmentation products. The figure is adapted with permission from Reference 86; copyright 2021 American Chemical Society.

Many of the aforementioned studies focused on differentiating elementary units and small molecules towards the analysis of larger biomolecules. Enzymatic digestion-based protocols have also been used in combination with the high resolution and multifunctionality of the cIM system to accomplish proteomic and glycomic goals. For example, expanding into larger polysaccharide analyses, red algal cell walls were digested, resulting in octomeric oligoporphyrans, and multistage cIM with post-cIM fragmentation not only sequenced the porphyrans but localized the methyl ether and sulfate groups.[89] In a bottom-up proteomics approach, an IgG4 monoclonal antibody (mAb) with two noncanonical cysteine residues was tryptically digested and subjected to multipass IM.[99] The resulting disulfide-linked dipeptides were unambiguously identified by comparing high-resolution arrival-time distribution profiles with potential peptide isomers; the number and location of the linkages were determined with only high-resolution IM.[99] Similarly, for a therapeutic multispecific mAb, a middle-up approach in combination with a high-resolution cIM separation was necessary to confirm the presence of

two conformers and the location of the isomerism [91]. Isolating portions of the arrival-time distribution and subjecting those ions to additional stages of cIM also suggests that isomer interconversion was minimal.[91]

The cIM system is also being applied to the structural analysis of intact proteins. One challenge is that increasing the number of passes also increases the time available for structural isomerization during experiments. Analysis of native-like ions of cytochrome *c* (12 kDa monomer), β-lactoglobulin (16 kDa monomer), and concanavalin A (51 kDa dimer or 102 kDa tetramer) suggest that the mobilities of the low-mass proteins ions exhibit subtle changes over those timescales, but those of the high-mass protein ions do not.[100] Follow-on studies highlighted the unique capabilities of the cIM system to probe phenomena such as sequential unfolding, irreversible versus reversible unfolding, and interconversion during the separation.[92] Additionally, to investigate the conformational dynamics of even larger native-like and aggregated biomolecules with cIM, the transmission of intact proteins (1.5 MDa) and oligonucleotides (63 kDa) was demonstrated.[101] With the recent integration of complementary dissociation techniques, including electron-capture dissociation[90,94] and surface-induced dissociation,[95] the cIM system offers many exciting possibilities for hybrid, top-down MS experiments.

1.4 Trapped IM Spectrometry (TIMS)

Thus far, we have only discussed implementations of IM whose performance depends on the distance that ions traverse in the laboratory frame of reference, through single or multiple passes. In TIMS, a gas flow propels ions forward against a repulsive gradient of *E*.[102] Ions reach an equilibrium position that corresponds to where the electrostatic force equals the counteracting

drag force.[103] As the electric field gradient is decreased, ions of lower *K* elute from the device first as the drag force overcomes the now-reduced electrostatic force. High resolution separations can be achieved by tuning the scanning speed of the gradient;[21] note that under a given set of conditions lower-*K* ions will generally exhibit a larger value of R_p^{Ω}. TIMS separations have achieved R_p^{Ω} of ~400 in separating singly charged polybrominated diphenyl ether metabolites,[104] whereas a R_p^{Ω} of 295 was observed for an elongated conformer of 7+ ubiquitin.[105] Beyond tunable resolving power, TIMS boasts high sensitivity owing both to the radial confinement and higher capacities for ion accumulation, as well as the ability to measure **Ω** values in agreement with values determined using drift-tube IM.[37] These features, commercialized by Bruker Co., make TIMS an accessible and potent IM platform, as evidenced by the number of recent publications ranging in application from lipidomics,[106–109] glycomics,[110,111] proteomics,[112–116] and beyond. One particularly noteworthy application of TIMS is its synchronization with tandem MS to increase the sensitivity of both data-dependent[106] and data-independent[117] omics workflows. Previous reviews provide a more comprehensive summary of TIMS operation[28] and its various applications to biomolecules.[37]

Other next-generation innovations using TIMS have focused on adding orthogonality. In one study, TIMS was combined with surface-induced dissociation (SID), which enabled the charge state-dependent dissociation of protein complexes and the conformation-dependent dissociation of isobaric peptides.[118] In analyzing SID products, observed charge-state distributions and retention of bound ligands indicated that TIMS can probe native-like structures with properly tuned parameters.[118] A TIMS-electron capture dissociation workflow was used to characterize the post-translational modifications of histone tails.[119] TIMS was used to address analytical difficulties owing to the isobaric and isomeric nature of these post-translational

modifications, resolving different conformations such that subsequent electron capture dissociation revealed the location of the post-translational modifications.[119] TIMS was also combined with ultraviolet photodissociation, which was used to characterize isobaric and isomeric species at R_p^{Ω} values >100.[120] Another implementation of the TIMS platform coupled with electron excitation dissociation generated isomer-specific glycan fragments that were consistent across multiple observed conformations for individual glycans.[121] Taken as a whole, these studies illustrate the potential for TIMS to address shortcomings in top-down proteomics, lipidomics, and glycomics studies hindered by isomeric and isobaric species. Furthermore, the ability to vary the scanning speed enables the facile synchronization of TIMS separations with high-resolution, albeit lower duty cycle, mass analyzers such as Fourier-transform ion cyclotron resonance.[122]

The TIMS technology has been further advanced on prototype instruments in research laboratories. Fernandez-Lima and coworkers introduced a TIMS cell with an extended mass range enabled by convex electrodes that increase the penetration of the pseudo-potential well.[123] Ω values were obtained for a wide range of native-like proteins and protein complexes, ranging from ubiquitin to GroEL, and those values were consistent with those from drift-tube IM.[123] Since its introduction, this system has been used to elucidate the binding dynamics of an intrinsically disordered DNA-binding protein; results from collision-induced unfolding experiments exhibited evidence for increased protein stability upon DNA binding.[124]

Bleiholder and coworkers introduced TIMS-TIMS, or tandem TIMS;[125] implementations and early applications of this technology were reviewed recently.[126] Briefly, the first implementation consisted of two prototype TIMS devices, which will be referred to as TIMS-1 and TIMS-2, interfaced coaxially using ion apertures capable of collisional activation.[125] One

consideration for the coaxial device involves defining the gas flow between the devices; pressure differentials between TIMS-1 and TIMS-2 result in a tradeoff between resolution and ion activation.[126] More recently, the coaxial device was used to analyze the gas-phase structures of top-down protein fragments (Figure 1.5).[127] Following mobility-selection and fragmentation, **Ω** measurements in TIMS-2 revealed that top-down fragments exhibited structural heterogeneity and multiple conformations. Notably, the **Ω** distributions of the y_n^{4+} fragment series of ubiquitin show a compaction event upon the incorporation of a basic residue (Figure 1.5B).[127] Time-resolved, TIMS-2 measurements of the y_n^{4+} fragment series provide evidence for the formation of metastable conformations; ions that exhibited both compact and extended conformations underwent folding on the seconds timescale (Figure 1.5 C-E).[127] These experiments illustrate the potential of multidimensional IM experiments to inform the relationship between precursor and product ion structure in top-down proteomics. A more recent implementation interfaces two commercial TIMS devices orthogonally, separated by an ion trap to enable ultraviolet photodissociation.[128] Ion trap conditions were sufficiently soft to maintain native-like structures, which were then fragmented prior to TIMS-2 separations that enabled increased fragment identification.[128] Despite limitations of available activation methods accessible at tandem TIMS pressure regimes,[126] this approach is poised to offer unique insights for structural proteomics.

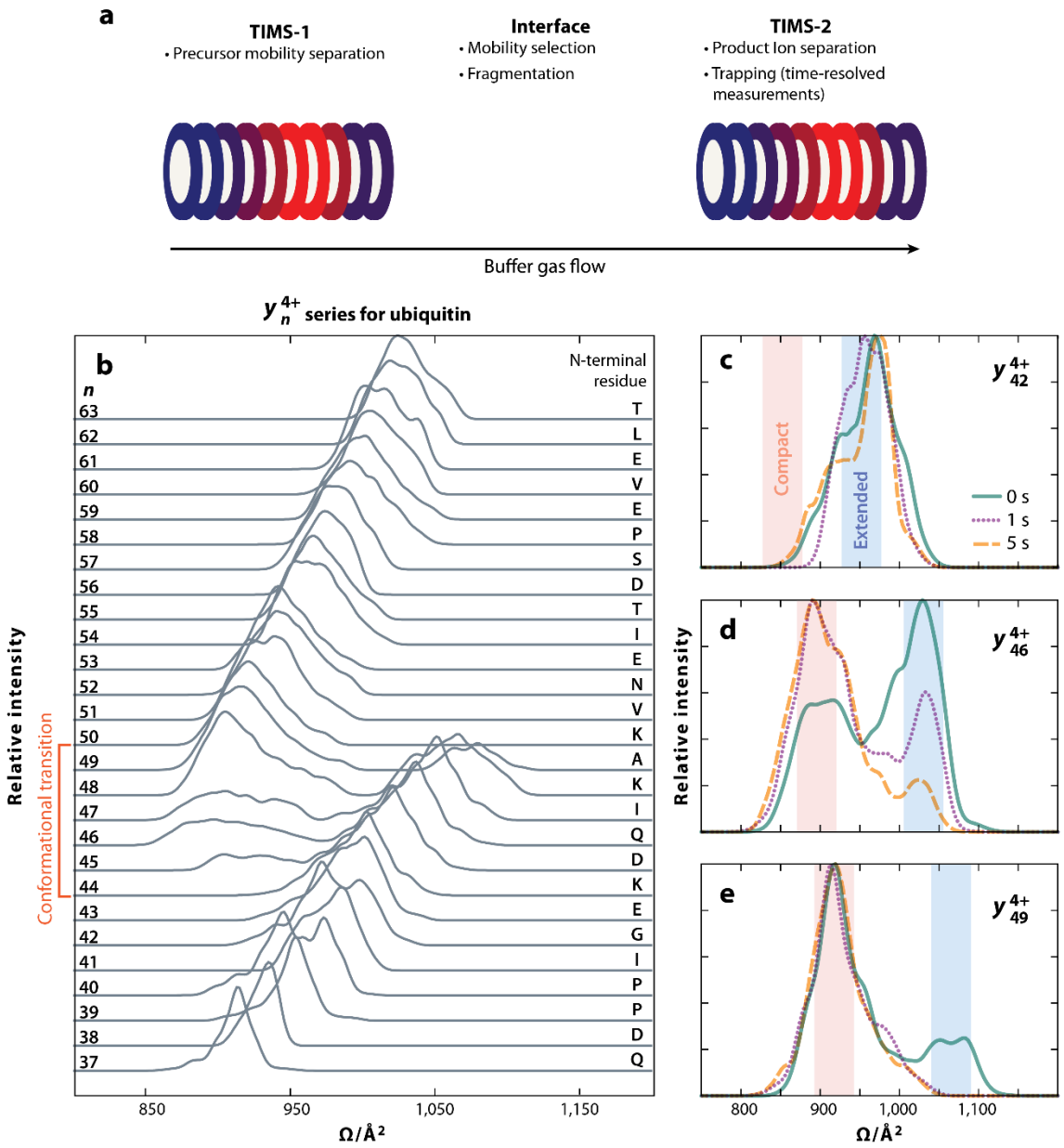

Figure 1.5. (A) Schematic of the tandem TIMS implementation reproduced using the cartoons from Figure 1.1; the system used for these experiments has been reported.[127] (B) IM spectra of the y_n^{4+} fragment series of ubiquitin. At y_{44}^{4+}, compaction is observed as the Ω values of the fragment ions decrease with increasing number of residues. Panels C, D, and E show the time-dependent IM distributions of selected ions of the fragment series. Whereas y_{42}^{4+} and y_{49}^{4+} remain primarily in extended and compact conformations

respectively, y_{46}^{4+} undergoes a time-dependent compaction that is evidence for gas-phase folding. Panels B-E are adapted with permission from Reference 127; copyright 2022 American Chemical Society. Abbreviations: IM, ion mobility; TIMS, trapped IM spectrometry.

1.5 Conclusions and Future Perspectives.

Sustained innovation continues to redefine the performance of IM-enabled experiments (Figure 1.1). These advances have already had great impacts on the ability of MS-based measurements to analyze isomeric and isobaric species, e.g., as evidenced by the extensive application of SLIM (Figures 1.2 and 1.3), cIM (Figure 1.4), and TIMS to glycans. Multidimensional experiments that activate ions between dimensions of IM increase information content by enabling conformer-dependent unfolding and fragmentation. This feature has been elegantly implemented on multiple platforms, including the SLIM/cryo-IR (Figure 1.3), cIM (Figure 1.4), and TIMS-TIMS (Figure 1.5) systems. Many initial applications of the next-generation technologies summarized in Figure 1.1 have focused on glycomics, lipidomics, and peptidomics. There has been a long-standing interest in using IM-MS as a high-throughput replacement for LC-MS. The applications described here demonstrate the effectiveness of IM to resolve the components of mixtures that had previously required LC and that had not been successfully separated using LC. We note that LC-MS methods benefit from the peak capacity of LC separations, as well as the ability of LC systems to manage samples and deliver eluent that is amenable to electrospray ionization (e.g., by desalting samples). For routine, high-throughput measurements, we propose that IM-enabled methods will benefit greatly from using LC, IM, and

MS in tandem, i.e., using fast, minimal LC to manage and prepare samples for ionization and then using next-generation IM experiments to add the necessary level of selectivity.

As expected, new innovations tend to reveal new challenges. For example, collisional activation may be insufficient to fragment many intact protein ions. Complementary methods of activation combined with high-resolution IM may be especially useful for differentiating the components that contribute to the congestion that is characteristic of top-down mass spectra. Instrument geometries that support multiple passes, including the cIM and some implementations of TW-SLIM, enable methods that increase the pathlength to achieve the required resolution for an application. However, multiple passes can also result in ion wrap-around, which can hinder data analysis or require the analysis to focus on progressively narrower mobility ranges while discarding other ions as the separation length is increased. IM separations using long geometries and/or multiple passes take longer to perform, which makes it more challenging to use the entire flux produced by the ion source and increases the likelihood of structural isomerization and ion chemistry during experiments. More generally, multidimensional experiments often yield complex data that resist simple analysis workflows. Nevertheless, we suspect that researchers will continue to innovate, that these and other challenges will be addressed, and that these next-generation IM technologies will fulfill even greater roles in biomolecular analysis in the years ahead.

1.6 Acknowledgements.

This work was supported by the National Institute of General Medical Sciences of the National Institutes of Health under award number R01GM130708 and by National Science

Foundation through award 2203513 from the Division of Chemistry, with partial co-funding from the Division of Molecular and Cellular Biosciences.

1.7 References

(1) Zeleny, J. VI. On the Ratio of the Velocities of the Two Ions Produced in Gases by Röntgen Radiation; and on Some Related Phenomena. Lond. Edinb. Dublin Philos. Mag. J. Sci. **1898**, 46 (278), 120–154. https://doi.org/10.1080/14786449808621173.

(2) Gabelica, V.; Shvartsburg, A. A.; Afonso, C.; Barran, P.; Benesch, J. L. P.; Bleiholder, C.; Bowers, M. T.; Bilbao, A.; Bush, M. F.; Campbell, J. L.; Campuzano, I. D. G.; Causon, T.; Clowers, B. H.; Creaser, C. S.; De Pauw, E.; Far, J.; Fernandez-Lima, F.; Fjeldsted, J. C.; Giles, K.; Groessl, M.; Hogan, C. J.; Hann, S.; Kim, H. I.; Kurulugama, R. T.; May, J. C.; McLean, J. A.; Pagel, K.; Richardson, K.; Ridgeway, M. E.; Rosu, F.; Sobott, F.; Thalassinos, K.; Valentine, S. J.; Wyttenbach, T. Recommendations for Reporting Ion Mobility Mass Spectrometry Measurements. Mass Spectrom. Rev. **2019**, 38 (3), 291–320. https://doi.org/10.1002/mas.21585.

(3) Revercomb, H. E.; Mason, E. A. Theory of Plasma Chromatography/Gaseous Electrophoresis. Review. Anal. Chem. **1975**, 47 (7), 970–983. https://doi.org/10.1021/ac60357a043.

(4) Mason, E.; McDaniel, W. Transport Properties of Ions in Gases; Wiley, 1988.

(5) Gabelica, V.; Marklund, E. Fundamentals of Ion Mobility Spectrometry. Curr. Opin. Chem. Biol. **2018**, 42, 51–59. https://doi.org/10.1016/j.cbpa.2017.10.022.

(6) Puton, J.; Namieśnik, J. Ion Mobility Spectrometry: Current Status and Application for Chemical Warfare Agents Detection. TrAC Trends Anal. Chem. **2016**, 85, 10–20. https://doi.org/10.1016/j.trac.2016.06.002.

(7) Ewing, R. A Critical Review of Ion Mobility Spectrometry for the Detection of Explosives and Explosive Related Compounds. Talanta **2001**, 54 (3), 515–529. https://doi.org/10.1016/S0039-9140(00)00565-8.

(8) Márquez-Sillero, I.; Aguilera-Herrador, E.; Cárdenas, S.; Valcárcel, M. Ion-Mobility Spectrometry for Environmental Analysis. TrAC Trends Anal. Chem. **2011**, 30 (5), 677–690. https://doi.org/10.1016/j.trac.2010.12.007.

(9) Kanu, A. B.; Dwivedi, P.; Tam, M.; Matz, L.; Hill, H. H. Ion Mobility-Mass Spectrometry. J. Mass Spectrom. **2008**, 43 (1), 1–22. https://doi.org/10.1002/jms.1383.

(10) Cumeras, R.; Figueras, E.; Davis, C. E.; Baumbach, J. I.; Gràcia, I. Review on Ion Mobility Spectrometry. Part 1: Current Instrumentation. The Analyst **2015**, 140 (5), 1376–1390. https://doi.org/10.1039/C4AN01100G.

(11) May, J. C.; McLean, J. A. Ion Mobility-Mass Spectrometry: Time-Dispersive Instrumentation. Anal. Chem. **2015**, 87 (3), 1422–1436. https://doi.org/10.1021/ac504720m.

(12) Dodds, J. N.; Baker, E. S. Ion Mobility Spectrometry: Fundamental Concepts, Instrumentation, Applications, and the Road Ahead. J. Am. Soc. Mass Spectrom. **2019**, 30 (11), 2185–2195. https://doi.org/10.1007/s13361-019-02288-2.

(13) Eldrid, C.; Thalassinos, K. Developments in Tandem Ion Mobility Mass Spectrometry. Biochem. Soc. Trans. **2020**, 48 (6), 2457–2466. https://doi.org/10.1042/BST20190788.

(14) Hoaglund, C. S.; Valentine, S. J.; Sporleder, C. R.; Reilly, J. P.; Clemmer, D. E. Three-Dimensional Ion Mobility/TOFMS Analysis of Electrosprayed Biomolecules. Anal. Chem. **1998**, 70 (11), 2236–2242. https://doi.org/10.1021/ac980059c.

(15) Wittmer, Doug.; Chen, Y. Hong.; Luckenbill, B. K.; Hill, H. H. Electrospray Ionization Ion Mobility Spectrometry. Anal. Chem. **1994**, 66 (14), 2348–2355. https://doi.org/10.1021/ac00086a021.
(16) Clemmer, D. E.; Hudgins, R. R.; Jarrold, M. F. Naked Protein Conformations: Cytochrome c in the Gas Phase. J. Am. Chem. Soc. **1995**, 117 (40), 10141–10142. https://doi.org/10.1021/ja00145a037.
(17) Wyttenbach, T.; von Helden, G.; Bowers, M. T. Gas-Phase Conformation of Biological Molecules: Bradykinin. J. Am. Chem. Soc. **1996**, 118 (35), 8355–8364. https://doi.org/10.1021/ja9535928.
(18) Shelimov, K. B.; Clemmer, D. E.; Hudgins, R. R.; Jarrold, M. F. Protein Structure in Vacuo : Gas-Phase Conformations of BPTI and Cytochrome c. J. Am. Chem. Soc. **1997**, 119 (9), 2240–2248. https://doi.org/10.1021/ja9619059.
(19) Liu, Y.; Clemmer, D. E. Characterizing Oligosaccharides Using Injected-Ion Mobility/Mass Spectrometry. Anal. Chem. **1997**, 69 (13), 2504–2509. https://doi.org/10.1021/ac9701344.
(20) Wu, C.; Siems, W. F.; Asbury, G. R.; Hill, H. H. Electrospray Ionization High-Resolution Ion Mobility Spectrometry−Mass Spectrometry. Anal. Chem. **1998**, 70 (23), 4929–4938. https://doi.org/10.1021/ac980414z.
(21) Kirk, A. T.; Bohnhorst, A.; Raddatz, C.-R.; Allers, M.; Zimmermann, S. Ultra-High-Resolution Ion Mobility Spectrometry—Current Instrumentation, Limitations, and Future Developments. Anal. Bioanal. Chem. **2019**, 411 (24), 6229–6246. https://doi.org/10.1007/s00216-019-01807-0.
(22) Gillig, K. J.; Ruotolo, B. T.; Stone, E. G.; Russell, D. H. An Electrostatic Focusing Ion Guide for Ion Mobility-Mass Spectrometry. Int. J. Mass Spectrom. **2004**, 239 (1), 43–49. https://doi.org/10.1016/j.ijms.2004.09.005.
(23) Silveira, J. A.; Gamage, C. M.; Blase, R. C.; Russell, D. H. Gas-Phase Ion Dynamics in a Periodic-Focusing DC Ion Guide. Int. J. Mass Spectrom. **2010**, 296 (1–3), 36–42. https://doi.org/10.1016/j.ijms.2010.07.019.
(24) Allen, S. J.; Bush, M. F. Radio-Frequency (Rf) Confinement in Ion Mobility Spectrometry: Apparent Mobilities and Effective Temperatures. J. Am. Soc. Mass Spectrom. **2016**, 27 (12), 2054–2063. https://doi.org/10.1007/s13361-016-1479-9.
(25) Koeniger, S. L.; Merenbloom, S. I.; Valentine, S. J.; Jarrold, M. F.; Udseth, H. R.; Smith, R. D.; Clemmer, D. E. An IMS−IMS Analogue of MS−MS. Anal. Chem. **2006**, 78 (12), 4161–4174. https://doi.org/10.1021/ac051060w.
(26) Merenbloom, S. I.; Koeniger, S. L.; Valentine, S. J.; Plasencia, M. D.; Clemmer, D. E. IMS−IMS and IMS−IMS−IMS/MS for Separating Peptide and Protein Fragment Ions. Anal. Chem. **2006**, 78 (8), 2802–2809. https://doi.org/10.1021/ac052208e.
(27) Giles, K.; Pringle, S. D.; Worthington, K. R.; Little, D.; Wildgoose, J. L.; Bateman, R. H. Applications of a Travelling Wave-Based Radio-Frequency-Only Stacked Ring Ion Guide. Rapid Commun. Mass Spectrom. **2004**, 18 (20), 2401–2414. https://doi.org/10.1002/rcm.1641.
(28) Ridgeway, M. E.; Lubeck, M.; Jordens, J.; Mann, M.; Park, M. A. Trapped Ion Mobility Spectrometry: A Short Review. Int. J. Mass Spectrom. **2018**, 425, 22–35. https://doi.org/10.1016/j.ijms.2018.01.006.

(29) Fernandez-Lima, F. A.; Kaplan, D. A.; Park, M. A. Note: Integration of Trapped Ion Mobility Spectrometry with Mass Spectrometry. Rev. Sci. Instrum. **2011**, 82 (12), 126106. https://doi.org/10.1063/1.3665933.
(30) Webb, I. K.; Garimella, S. V. B.; Tolmachev, A. V.; Chen, T.-C.; Zhang, X.; Norheim, R. V.; Prost, S. A.; LaMarche, B.; Anderson, G. A.; Ibrahim, Y. M.; Smith, R. D. Experimental Evaluation and Optimization of Structures for Lossless Ion Manipulations for Ion Mobility Spectrometry with Time-of-Flight Mass Spectrometry. Anal. Chem. **2014**, 86 (18), 9169–9176. https://doi.org/10.1021/ac502055e.
(31) Hamid, A. M.; Ibrahim, Y. M.; Garimella, S. V. B.; Webb, I. K.; Deng, L.; Chen, T.-C.; Anderson, G. A.; Prost, S. A.; Norheim, R. V.; Tolmachev, A. V.; Smith, R. D. Characterization of Traveling Wave Ion Mobility Separations in Structures for Lossless Ion Manipulations. Anal. Chem. **2015**, 87 (22), 11301–11308. https://doi.org/10.1021/acs.analchem.5b02481.
(32) Giles, K.; Ujma, J.; Wildgoose, J.; Pringle, S.; Richardson, K.; Langridge, D.; Green, M. A Cyclic Ion Mobility-Mass Spectrometry System. Anal. Chem. **2019**, 91 (13), 8564–8573. https://doi.org/10.1021/acs.analchem.9b01838.
(33) Baker, E. S.; Clowers, B. H.; Li, F.; Tang, K.; Tolmachev, A. V.; Prior, D. C.; Belov, M. E.; Smith, R. D. Ion Mobility Spectrometry—Mass Spectrometry Performance Using Electrodynamic Ion Funnels and Elevated Drift Gas Pressures. J. Am. Soc. Mass Spectrom. **2007**, 18 (7), 1176–1187. https://doi.org/10.1016/j.jasms.2007.03.031.
(34) Zhong, Y.; Hyung, S.-J.; Ruotolo, B. T. Characterizing the Resolution and Accuracy of a Second-Generation Traveling-Wave Ion Mobility Separator for Biomolecular Ions. The Analyst **2011**, 136 (17), 3534. https://doi.org/10.1039/c0an00987c.
(35) Davidson, K. L.; Bush, M. F. Effects of Drift Gas Selection on the Ambient-Temperature, Ion Mobility Mass Spectrometry Analysis of Amino Acids. Anal. Chem. **2017**, 89 (3), 2017–2023. https://doi.org/10.1021/acs.analchem.6b04605.
(36) Campuzano, I. D. G.; Giles, K. Historical, Current and Future Developments of Travelling Wave Ion Mobility Mass Spectrometry: A Personal Perspective. TrAC Trends Anal. Chem. **2019**, 120, 115620. https://doi.org/10.1016/j.trac.2019.115620.
(37) Jeanne Dit Fouque, K.; Fernandez-Lima, F. Recent Advances in Biological Separations Using Trapped Ion Mobility Spectrometry – Mass Spectrometry. TrAC Trends Anal. Chem. **2019**, 116, 308–315. https://doi.org/10.1016/j.trac.2019.04.010.
(38) Guevremont, R. High-Field Asymmetric Waveform Ion Mobility Spectrometry: A New Tool for Mass Spectrometry. J. Chromatogr. A **2004**, 1058 (1–2), 3–19. https://doi.org/10.1016/S0021-9673(04)01478-5.
(39) Merenbloom, S. I.; Glaskin, R. S.; Henson, Z. B.; Clemmer, D. E. High-Resolution Ion Cyclotron Mobility Spectrometry. Anal. Chem. **2009**, 81 (4), 1482–1487. https://doi.org/10.1021/ac801880a.
(40) Kurulugama, R. T.; Nachtigall, F. M.; Lee, S.; Valentine, S. J.; Clemmer, D. E. Overtone Mobility Spectrometry: Part 1. Experimental Observations. J. Am. Soc. Mass Spectrom. **2009**, 20 (5), 729–737. https://doi.org/10.1016/j.jasms.2008.11.022.
(41) Gamero-Castaño, M.; Fernández de la Mora, J. Mechanisms of Electrospray Ionization of Singly and Multiply Charged Salt Clusters. Anal. Chim. Acta **2000**, 406 (1), 67–91. https://doi.org/10.1016/S0003-2670(99)00596-6.

(42) Flagan, R. C. Continuous-Flow Differential Mobility Analysis of Nanoparticles and Biomolecules. Annu. Rev. Chem. Biomol. Eng. **2014**, 5 (1), 255–279. https://doi.org/10.1146/annurev-chembioeng-061312-103316.
(43) Tolmachev, A. V.; Webb, I. K.; Ibrahim, Y. M.; Garimella, S. V. B.; Zhang, X.; Anderson, G. A.; Smith, R. D. Characterization of Ion Dynamics in Structures for Lossless Ion Manipulations. Anal. Chem. **2014**, 86 (18), 9162–9168. https://doi.org/10.1021/ac502054p.
(44) Garimella, S. V. B.; Ibrahim, Y. M.; Webb, I. K.; Tolmachev, A. V.; Zhang, X.; Prost, S. A.; Anderson, G. A.; Smith, R. D. Simulation of Electric Potentials and Ion Motion in Planar Electrode Structures for Lossless Ion Manipulations (SLIM). J. Am. Soc. Mass Spectrom. **2014**, 25 (11), 1890–1896. https://doi.org/10.1007/s13361-014-0976-y.
(45) Webb, I. K.; Garimella, S. V. B.; Tolmachev, A. V.; Chen, T.-C.; Zhang, X.; Cox, J. T.; Norheim, R. V.; Prost, S. A.; LaMarche, B.; Anderson, G. A.; Ibrahim, Y. M.; Smith, R. D. Mobility-Resolved Ion Selection in Uniform Drift Field Ion Mobility Spectrometry/Mass Spectrometry: Dynamic Switching in Structures for Lossless Ion Manipulations. Anal. Chem. **2014**, 86 (19), 9632–9637. https://doi.org/10.1021/ac502139e.
(46) Zhang, X.; Garimella, S. V. B.; Prost, S. A.; Webb, I. K.; Chen, T.-C.; Tang, K.; Tolmachev, A. V.; Norheim, R. V.; Baker, E. S.; Anderson, G. A.; Ibrahim, Y. M.; Smith, R. D. Ion Trapping, Storage, and Ejection in Structures for Lossless Ion Manipulations. Anal. Chem. **2015**, 87 (12), 6010–6016. https://doi.org/10.1021/acs.analchem.5b00214.
(47) Chen, T.-C.; Ibrahim, Y. M.; Webb, I. K.; Garimella, S. V. B.; Zhang, X.; Hamid, A. M.; Deng, L.; Karnesky, W. E.; Prost, S. A.; Sandoval, J. A.; Norheim, R. V.; Anderson, G. A.; Tolmachev, A. V.; Baker, E. S.; Smith, R. D. Mobility-Selected Ion Trapping and Enrichment Using Structures for Lossless Ion Manipulations. Anal. Chem. **2016**, 88 (3), 1728–1733. https://doi.org/10.1021/acs.analchem.5b03910.
(48) Allen, S. J.; Eaton, R. M.; Bush, M. F. Analysis of Native-Like Ions Using Structures for Lossless Ion Manipulations. Anal. Chem. **2016**, 88 (18), 9118–9126. https://doi.org/10.1021/acs.analchem.6b02089.
(49) Eaton, R. M.; Allen, S. J.; Bush, M. F. Principles of Ion Selection, Alignment, and Focusing in Tandem Ion Mobility Implemented Using Structures for Lossless Ion Manipulations (SLIM). J. Am. Soc. Mass Spectrom. **2019**, 30 (6), 1115–1125. https://doi.org/10.1007/s13361-019-02170-1.
(50) Allen, S. J.; Eaton, R. M.; Bush, M. F. Structural Dynamics of Native-Like Ions in the Gas Phase: Results from Tandem Ion Mobility of Cytochrome c. Anal. Chem. **2017**, 89 (14), 7527–7534. https://doi.org/10.1021/acs.analchem.7b01234.
(51) Hamid, A. M.; Garimella, S. V. B.; Ibrahim, Y. M.; Deng, L.; Zheng, X.; Webb, I. K.; Anderson, G. A.; Prost, S. A.; Norheim, R. V.; Tolmachev, A. V.; Baker, E. S.; Smith, R. D. Achieving High Resolution Ion Mobility Separations Using Traveling Waves in Compact Multiturn Structures for Lossless Ion Manipulations. Anal. Chem. **2016**, 88 (18), 8949–8956. https://doi.org/10.1021/acs.analchem.6b01914.
(52) Deng, L.; Ibrahim, Y. M.; Hamid, A. M.; Garimella, S. V. B.; Webb, I. K.; Zheng, X.; Prost, S. A.; Sandoval, J. A.; Norheim, R. V.; Anderson, G. A.; Tolmachev, A. V.; Baker, E. S.; Smith, R. D. Ultra-High Resolution Ion Mobility Separations Utilizing Traveling Waves in a 13 m Serpentine Path Length Structures for Lossless Ion Manipulations Module. Anal. Chem. **2016**, 88 (18), 8957–8964. https://doi.org/10.1021/acs.analchem.6b01915.

(53) Deng, L.; Webb, I. K.; Garimella, S. V. B.; Hamid, A. M.; Zheng, X.; Norheim, R. V.; Prost, S. A.; Anderson, G. A.; Sandoval, J. A.; Baker, E. S.; Ibrahim, Y. M.; Smith, R. D. Serpentine Ultralong Path with Extended Routing (SUPER) High Resolution Traveling Wave Ion Mobility-MS Using Structures for Lossless Ion Manipulations. Anal. Chem. **2017**, 89 (8), 4628–4634. https://doi.org/10.1021/acs.analchem.7b00185.

(54) Garimella, S. V. B.; Nagy, G.; Ibrahim, Y. M.; Smith, R. D. Opening New Paths for Biological Applications of Ion Mobility - Mass Spectrometry Using Structures for Lossless Ion Manipulations. TrAC Trends Anal. Chem. **2019**, 116, 300–307. https://doi.org/10.1016/j.trac.2019.04.021.

(55) Deng, L.; Ibrahim, Y. M.; Baker, E. S.; Aly, N. A.; Hamid, A. M.; Zhang, X.; Zheng, X.; Garimella, S. V. B.; Webb, I. K.; Prost, S. A.; Sandoval, J. A.; Norheim, R. V.; Anderson, G. A.; Tolmachev, A. V.; Smith, R. D. Ion Mobility Separations of Isomers Based upon Long Path Length Structures for Lossless Ion Manipulations Combined with Mass Spectrometry. ChemistrySelect **2016**, 1 (10), 2396–2399. https://doi.org/10.1002/slct.201600460.

(56) Nagy, G.; Attah, I. K.; Conant, C. R.; Liu, W.; Garimella, S. V. B.; Gunawardena, H. P.; Shaw, J. B.; Smith, R. D.; Ibrahim, Y. M. Rapid and Simultaneous Characterization of Drug Conjugation in Heavy and Light Chains of a Monoclonal Antibody Revealed by High-Resolution Ion Mobility Separations in SLIM. Anal. Chem. **2020**, 92 (7), 5004–5012. https://doi.org/10.1021/acs.analchem.9b05209.

(57) Deng, L.; Garimella, S. V. B.; Hamid, A. M.; Webb, I. K.; Attah, I. K.; Norheim, R. V.; Prost, S. A.; Zheng, X.; Sandoval, J. A.; Baker, E. S.; Ibrahim, Y. M.; Smith, R. D. Compression Ratio Ion Mobility Programming (CRIMP) Accumulation and Compression of Billions of Ions for Ion Mobility-Mass Spectrometry Using Traveling Waves in Structures for Lossless Ion Manipulations (SLIM). Anal. Chem. **2017**, 89 (12), 6432–6439. https://doi.org/10.1021/acs.analchem.7b00189.

(58) Nagy, G.; Kedia, K.; Attah, I. K.; Garimella, S. V. B.; Ibrahim, Y. M.; Petyuk, V. A.; Smith, R. D. Separation of β-Amyloid Tryptic Peptide Species with Isomerized and Racemized L-Aspartic Residues with Ion Mobility in Structures for Lossless Ion Manipulations. Anal. Chem. **2019**, 91 (7), 4374–4380. https://doi.org/10.1021/acs.analchem.8b04696.

(59) Hollerbach, A. L.; Li, A.; Prabhakaran, A.; Nagy, G.; Harrilal, C. P.; Conant, C. R.; Norheim, R. V.; Schimelfenig, C. E.; Anderson, G. A.; Garimella, S. V. B.; Smith, R. D.; Ibrahim, Y. M. Ultra-High-Resolution Ion Mobility Separations Over Extended Path Lengths and Mobility Ranges Achieved Using a Multilevel Structures for Lossless Ion Manipulations Module. Anal. Chem. **2020**, 92 (11), 7972–7979. https://doi.org/10.1021/acs.analchem.0c01397.

(60) Hollerbach, A. L.; Norheim, R. V.; Kwantwi-Barima, P.; Smith, R. D.; Ibrahim, Y. M. A Miniature Multilevel Structures for Lossless Ion Manipulations Ion Mobility Spectrometer with Wide Mobility Range Separation Capabilities. Anal. Chem. **2022**, 94 (4), 2180–2188. https://doi.org/10.1021/acs.analchem.1c04700.

(61) May, J. C.; Leaptrot, K. L.; Rose, B. S.; Moser, K. L. W.; Deng, L.; Maxon, L.; DeBord, D.; McLean, J. A. Resolving Power and Collision Cross Section Measurement Accuracy of a Prototype High-Resolution Ion Mobility Platform Incorporating Structures for Lossless Ion Manipulation. J. Am. Soc. Mass Spectrom. **2021**, 32 (4), 1126–1137. https://doi.org/10.1021/jasms.1c00056.

(62) Wormwood Moser, K. L.; Van Aken, G.; DeBord, D.; Hatcher, N. G.; Maxon, L.; Sherman, M.; Yao, L.; Ekroos, K. High-Defined Quantitative Snapshots of the Ganglioside Lipidome Using High Resolution Ion Mobility SLIM Assisted Shotgun Lipidomics. Anal. Chim. Acta **2021**, 1146, 77–87. https://doi.org/10.1016/j.aca.2020.12.022.

(63) Arndt, J. R.; Wormwood Moser, K. L.; Van Aken, G.; Doyle, R. M.; Talamantes, T.; DeBord, D.; Maxon, L.; Stafford, G.; Fjeldsted, J.; Miller, B.; Sherman, M. High-Resolution Ion-Mobility-Enabled Peptide Mapping for High-Throughput Critical Quality Attribute Monitoring. J. Am. Soc. Mass Spectrom. **2021**, 32 (8), 2019–2032. https://doi.org/10.1021/jasms.0c00434.

(64) Ben Faleh, A.; Warnke, S.; Rizzo, T. R. Combining Ultrahigh-Resolution Ion-Mobility Spectrometry with Cryogenic Infrared Spectroscopy for the Analysis of Glycan Mixtures. Anal. Chem. **2019**, 91 (7), 4876–4882. https://doi.org/10.1021/acs.analchem.9b00659.

(65) Warnke, S.; Ben Faleh, A.; Scutelnic, V.; Rizzo, T. R. Separation and Identification of Glycan Anomers Using Ultrahigh-Resolution Ion-Mobility Spectrometry and Cryogenic Ion Spectroscopy. J. Am. Soc. Mass Spectrom. **2019**, 30 (11), 2204–2211. https://doi.org/10.1007/s13361-019-02333-0.

(66) Abikhodr, A. H.; Yatsyna, V.; Ben Faleh, A.; Warnke, S.; Rizzo, T. R. Identifying Mixtures of Isomeric Human Milk Oligosaccharides by the Decomposition of IR Spectral Fingerprints. Anal. Chem. **2021**, 93 (44), 14730–14736. https://doi.org/10.1021/acs.analchem.1c03190.

(67) Warnke, S.; Ben Faleh, A.; Rizzo, T. R. Toward High-Throughput Cryogenic IR Fingerprinting of Mobility-Separated Glycan Isomers. ACS Meas. Sci. Au **2021**, 1 (3), 157–164. https://doi.org/10.1021/acsmeasuresciau.1c00018.

(68) Dyukova, I.; Ben Faleh, A.; Warnke, S.; Yalovenko, N.; Yatsyna, V.; Bansal, P.; Rizzo, T. R. A New Approach for Identifying Positional Isomers of Glycans Cleaved from Monoclonal Antibodies. The Analyst **2021**, 146 (15), 4789–4795. https://doi.org/10.1039/D1AN00780G.

(69) Bansal, P.; Yatsyna, V.; AbiKhodr, A. H.; Warnke, S.; Ben Faleh, A.; Yalovenko, N.; Wysocki, V. H.; Rizzo, T. R. Using SLIM-Based IMS-IMS Together with Cryogenic Infrared Spectroscopy for Glycan Analysis. Anal. Chem. **2020**, 92 (13), 9079–9085. https://doi.org/10.1021/acs.analchem.0c01265.

(70) Bansal, P.; Ben Faleh, A.; Warnke, S.; Rizzo, T. R. Identification of N -Glycan Positional Isomers by Combining IMS and Vibrational Fingerprinting of Structurally Determinant CID Fragments. The Analyst **2022**, 147 (4), 704–711. https://doi.org/10.1039/D1AN01861B.

(71) Pellegrinelli, R. P.; Yue, L.; Carrascosa, E.; Ben Faleh, A.; Warnke, S.; Bansal, P.; Rizzo, T. R. A New Strategy Coupling Ion-Mobility-Selective CID and Cryogenic IR Spectroscopy to Identify Glycan Anomers. J. Am. Soc. Mass Spectrom. **2022**, 33 (5), 859–864. https://doi.org/10.1021/jasms.2c00043.

(72) Ben Faleh, A.; Warnke, S.; Bansal, P.; Pellegrinelli, R. P.; Dyukova, I.; Rizzo, T. R. Identification of Mobility-Resolved N -Glycan Isomers. Anal. Chem. **2022**, 94 (28), 10101–10108. https://doi.org/10.1021/acs.analchem.2c01181.

(73) Pringle, S. D.; Giles, K.; Wildgoose, J. L.; Williams, J. P.; Slade, S. E.; Thalassinos, K.; Bateman, R. H.; Bowers, M. T.; Scrivens, J. H. An Investigation of the Mobility Separation of Some Peptide and Protein Ions Using a New Hybrid Quadrupole/Travelling

Wave IMS/Oa-ToF Instrument. Int. J. Mass Spectrom. **2007**, 261 (1), 1–12. https://doi.org/10.1016/j.ijms.2006.07.021.

(74) Giles, K.; Williams, J. P.; Campuzano, I. Enhancements in Travelling Wave Ion Mobility Resolution: Enhancements in Travelling Wave Ion Mobility Resolution. Rapid Commun. Mass Spectrom. **2011**, 25 (11), 1559–1566. https://doi.org/10.1002/rcm.5013.

(75) Higton, D.; Palmer, M. E.; Vissers, J. P. C.; Mullin, L. G.; Plumb, R. S.; Wilson, I. D. Use of Cyclic Ion Mobility Spectrometry (CIM)-Mass Spectrometry to Study the Intramolecular Transacylation of Diclofenac Acyl Glucuronide. Anal. Chem. **2021**, 93 (20), 7413–7421. https://doi.org/10.1021/acs.analchem.0c04487.

(76) Peterson, T. L.; Nagy, G. Rapid Cyclic Ion Mobility Separations of Monosaccharide Building Blocks as a First Step toward a High-Throughput Reaction Screening Platform for Carbohydrate Syntheses. RSC Adv. **2021**, 11 (63), 39742–39747. https://doi.org/10.1039/D1RA08746K.

(77) Cooper-Shepherd, D. A.; Olivos, H. J.; Wu, Z.; Palmer, M. E. Exploiting Self-Association to Evaluate Enantiomeric Composition by Cyclic Ion Mobility–Mass Spectrometry. Anal. Chem. **2022**, 94 (23), 8441–8448. https://doi.org/10.1021/acs.analchem.2c01212.

(78) Williamson, D. L.; Bergman, A. E.; Nagy, G. Investigating the Structure of α/β Carbohydrate Linkage Isomers as a Function of Group I Metal Adduction and Degree of Polymerization as Revealed by Cyclic Ion Mobility Separations. J. Am. Soc. Mass Spectrom. **2021**, 32 (10), 2573–2582. https://doi.org/10.1021/jasms.1c00207.

(79) Favreau, B.; Yeni, O.; Ollivier, S.; Boustie, J.; Dévéhat, F. L.; Guégan, J.-P.; Fanuel, M.; Rogniaux, H.; Brédy, R.; Compagnon, I.; Ropartz, D.; Legentil, L.; Ferrières, V. Synthesis of an Exhaustive Library of Naturally Occurring Gal f -Man p and Gal p -Man p Disaccharides. Toward Fingerprinting According to Ring Size by Advanced Mass Spectrometry-Based IM-MS and IRMPD. J. Org. Chem. **2021**, 86 (9), 6390–6405. https://doi.org/10.1021/acs.joc.1c00250.

(80) Ropartz, D.; Fanuel, M.; Ollivier, S.; Lissarrague, A.; Benkoulouche, M.; Mulard, L. A.; André, I.; Guieysse, D.; Rogniaux, H. Combination of High-Resolution Multistage Ion Mobility and Tandem MS with High Energy of Activation to Resolve the Structure of Complex Chemoenzymatically Synthesized Glycans. Anal. Chem. **2022**, 94 (4), 2279–2287. https://doi.org/10.1021/acs.analchem.1c04982.

(81) Sanda, M.; Morrison, L.; Goldman, R. N- and O-Glycosylation of the SARS-CoV-2 Spike Protein. Anal. Chem. **2021**, 93 (4), 2003–2009. https://doi.org/10.1021/acs.analchem.0c03173.

(82) Ujma, J.; Ropartz, D.; Giles, K.; Richardson, K.; Langridge, D.; Wildgoose, J.; Green, M.; Pringle, S. Cyclic Ion Mobility Mass Spectrometry Distinguishes Anomers and Open-Ring Forms of Pentasaccharides. J. Am. Soc. Mass Spectrom. **2019**, 30 (6), 1028–1037. https://doi.org/10.1007/s13361-019-02168-9.

(83) Tomczyk, N.; Giles, K.; Richardson, K.; Ujma, J.; Palmer, M.; Nielsen, P. K.; Haselmann, K. F. Mapping Isomeric Peptides Derived from Biopharmaceuticals Using High-Resolution Ion Mobility Mass Spectrometry. Anal. Chem. **2021**, 93 (49), 16379–16384. https://doi.org/10.1021/acs.analchem.1c02834.

(84) Kenderdine, T.; Nemati, R.; Baker, A.; Palmer, M.; Ujma, J.; FitzGibbon, M.; Deng, L.; Royzen, M.; Langridge, J.; Fabris, D. High-Resolution Ion Mobility Spectrometry-Mass Spectrometry of Isomeric/Isobaric Ribonucleotide Variants. J. Mass Spectrom. **2020**, 55 (2), e4465. https://doi.org/10.1002/jms.4465.

(85) McKenna, K. R.; Li, L.; Baker, A. G.; Ujma, J.; Krishnamurthy, R.; Liotta, C. L.; Fernández, F. M. Carbohydrate Isomer Resolution via Multi-Site Derivatization Cyclic Ion Mobility-Mass Spectrometry. The Analyst **2019**, 144 (24), 7220–7226. https://doi.org/10.1039/C9AN01584A.

(86) Ollivier, S.; Tarquis, L.; Fanuel, M.; Li, A.; Durand, J.; Laville, E.; Potocki-Veronese, G.; Ropartz, D.; Rogniaux, H. Anomeric Retention of Carbohydrates in Multistage Cyclic Ion Mobility (IMS ^{n}): De Novo Structural Elucidation of Enzymatically Produced Mannosides. Anal. Chem. **2021**, 93 (15), 6254–6261. https://doi.org/10.1021/acs.analchem.1c00673.

(87) Peterson, T. L.; Nagy, G. Toward Sequencing the Human Milk Glycome: High-Resolution Cyclic Ion Mobility Separations of Core Human Milk Oligosaccharide Building Blocks. Anal. Chem. **2021**, 93 (27), 9397–9407. https://doi.org/10.1021/acs.analchem.1c00942.

(88) Ollivier, S.; Fanuel, M.; Rogniaux, H.; Ropartz, D. Molecular Networking of High-Resolution Tandem Ion Mobility Spectra: A Structurally Relevant Way of Organizing Data in Glycomics? Anal. Chem. **2021**, 93 (31), 10871–10878. https://doi.org/10.1021/acs.analchem.1c01244.

(89) Ropartz, D.; Fanuel, M.; Ujma, J.; Palmer, M.; Giles, K.; Rogniaux, H. Structure Determination of Large Isomeric Oligosaccharides of Natural Origin through Multipass and Multistage Cyclic Traveling-Wave Ion Mobility Mass Spectrometry. Anal. Chem. **2019**, 91 (18), 12030–12037. https://doi.org/10.1021/acs.analchem.9b03036.

(90) Oganesyan, I.; Hajduk, J.; Harrison, J. A.; Marchand, A.; Czar, M. F.; Zenobi, R. Exploring Gas-Phase MS Methodologies for Structural Elucidation of Branched N -Glycan Isomers. Anal. Chem. **2022**, 94 (29), 10531–10539. https://doi.org/10.1021/acs.analchem.2c02019.

(91) Deslignière, E.; Ollivier, S.; Ehkirch, A.; Martelet, A.; Ropartz, D.; Lechat, N.; Hernandez-Alba, O.; Menet, J.-M.; Clavier, S.; Rogniaux, H.; Genet, B.; Cianférani, S. Combination of IM-Based Approaches to Unravel the Coexistence of Two Conformers on a Therapeutic Multispecific MAb. Anal. Chem. **2022**, 94 (22), 7981–7989. https://doi.org/10.1021/acs.analchem.2c00928.

(92) Eldrid, C.; Ben-Younis, A.; Ujma, J.; Britt, H.; Cragnolini, T.; Kalfas, S.; Cooper-Shepherd, D.; Tomczyk, N.; Giles, K.; Morris, M.; Akter, R.; Raleigh, D.; Thalassinos, K. Cyclic Ion Mobility–Collision Activation Experiments Elucidate Protein Behavior in the Gas Phase. J. Am. Soc. Mass Spectrom. **2021**, 32 (6), 1545–1552. https://doi.org/10.1021/jasms.1c00018.

(93) Sisley, E. K.; Ujma, J.; Palmer, M.; Giles, K.; Fernandez-Lima, F. A.; Cooper, H. J. LESA Cyclic Ion Mobility Mass Spectrometry of Intact Proteins from Thin Tissue Sections. Anal. Chem. **2020**, 92 (9), 6321–6326. https://doi.org/10.1021/acs.analchem.9b05169.

(94) Shaw, J. B.; Cooper-Shepherd, D. A.; Hewitt, D.; Wildgoose, J. L.; Beckman, J. S.; Langridge, J. I.; Voinov, V. G. Enhanced Top-Down Protein Characterization with Electron Capture Dissociation and Cyclic Ion Mobility Spectrometry. Anal. Chem. **2022**, 94 (9), 3888–3896. https://doi.org/10.1021/acs.analchem.1c04870.

(95) Snyder, D. T.; Jones, B. J.; Lin, Y.-F.; Cooper-Shepherd, D. A.; Hewitt, D.; Wildgoose, J.; Brown, J. M.; Langridge, J. I.; Wysocki, V. H. Surface-Induced Dissociation of Protein Complexes on a Cyclic Ion Mobility Spectrometer. The Analyst **2021**, 146 (22), 6861–6873. https://doi.org/10.1039/D1AN01407B.

(96) Riches, E.; Palmer, M. E. Application of a Novel Cyclic Ion Mobility-mass Spectrometer to the Analysis of Synthetic Polymers: A Preliminary Evaluation. Rapid Commun. Mass Spectrom. **2020**, 34 (S2). https://doi.org/10.1002/rcm.8710.
(97) Rüger, C. P.; Le Maître, J.; Maillard, J.; Riches, E.; Palmer, M.; Afonso, C.; Giusti, P. Exploring Complex Mixtures by Cyclic Ion Mobility High-Resolution Mass Spectrometry: Application Toward Petroleum. Anal. Chem. **2021**, 93 (14), 5872–5881. https://doi.org/10.1021/acs.analchem.1c00222.
(98) Cho, E.; Riches, E.; Palmer, M.; Giles, K.; Ujma, J.; Kim, S. Isolation of Crude Oil Peaks Differing by m / z ∼0.1 via Tandem Mass Spectrometry Using a Cyclic Ion Mobility-Mass Spectrometer. Anal. Chem. **2019**, 91 (22), 14268–14274. https://doi.org/10.1021/acs.analchem.9b02255.
(99) Deslignière, E.; Botzanowski, T.; Diemer, H.; Cooper-Shepherd, D. A.; Wagner-Rousset, E.; Colas, O.; Béchade, G.; Giles, K.; Hernandez-Alba, O.; Beck, A.; Cianférani, S. High-Resolution IMS–MS to Assign Additional Disulfide Bridge Pairing in Complementarity-Determining Regions of an IgG4 Monoclonal Antibody. J. Am. Soc. Mass Spectrom. **2021**, 32 (10), 2505–2512. https://doi.org/10.1021/jasms.1c00151.
(100) Eldrid, C.; Ujma, J.; Kalfas, S.; Tomczyk, N.; Giles, K.; Morris, M.; Thalassinos, K. Gas Phase Stability of Protein Ions in a Cyclic Ion Mobility Spectrometry Traveling Wave Device. Anal. Chem. **2019**, 91 (12), 7554–7561. https://doi.org/10.1021/acs.analchem.8b05641.
(101) Harrison, J. A.; Pruška, A.; Bittner, P.; Muck, A.; Cooper-Shepherd, D. A.; Zenobi, R. Advancing Cyclic Ion Mobility Mass Spectrometry Methods for Studying Biomolecules: Toward the Conformational Dynamics of Mega Dalton Protein Aggregates. Anal. Chem. **2022**, 94 (36), 12435–12443. https://doi.org/10.1021/acs.analchem.2c02406.
(102) Michelmann, K.; Silveira, J. A.; Ridgeway, M. E.; Park, M. A. Fundamentals of Trapped Ion Mobility Spectrometry. J. Am. Soc. Mass Spectrom. **2015**, 26 (1), 14–24. https://doi.org/10.1007/s13361-014-0999-4.
(103) Hernandez, D. R.; DeBord, J. D.; Ridgeway, M. E.; Kaplan, D. A.; Park, M. A.; Fernandez-Lima, F. Ion Dynamics in a Trapped Ion Mobility Spectrometer. The Analyst **2014**, 139 (8), 1913–1921. https://doi.org/10.1039/C3AN02174B.
(104) Adams, K. J.; Montero, D.; Aga, D.; Fernandez-Lima, F. Isomer Separation of Polybrominated Diphenyl Ether Metabolites Using NanoESI-TIMS-MS. Int. J. Ion Mobil. Spectrom. **2016**, 19 (2–3), 69–76. https://doi.org/10.1007/s12127-016-0198-z.
(105) Ridgeway, M. E.; Silveira, J. A.; Meier, J. E.; Park, M. A. Microheterogeneity within Conformational States of Ubiquitin Revealed by High Resolution Trapped Ion Mobility Spectrometry. The Analyst **2015**, 140 (20), 6964–6972. https://doi.org/10.1039/C5AN00841G.
(106) Vasilopoulou, C. G.; Sulek, K.; Brunner, A.-D.; Meitei, N. S.; Schweiger-Hufnagel, U.; Meyer, S. W.; Barsch, A.; Mann, M.; Meier, F. Trapped Ion Mobility Spectrometry and PASEF Enable In-Depth Lipidomics from Minimal Sample Amounts. Nat. Commun. **2020**, 11 (1), 331. https://doi.org/10.1038/s41467-019-14044-x.
(107) Fincher, J. A.; Djambazova, K. V.; Klein, D. R.; Dufresne, M.; Migas, L. G.; Van de Plas, R.; Caprioli, R. M.; Spraggins, J. M. Molecular Mapping of Neutral Lipids Using Silicon Nanopost Arrays and TIMS Imaging Mass Spectrometry. J. Am. Soc. Mass Spectrom. **2021**, 32 (10), 2519–2527. https://doi.org/10.1021/jasms.1c00159.

(108) Helmer, P. O.; Nordhorn, I. D.; Korf, A.; Behrens, A.; Buchholz, R.; Zubeil, F.; Karst, U.; Hayen, H. Complementing Matrix-Assisted Laser Desorption Ionization-Mass Spectrometry Imaging with Chromatography Data for Improved Assignment of Isobaric and Isomeric Phospholipids Utilizing Trapped Ion Mobility-Mass Spectrometry. Anal. Chem. **2021**, 93 (4), 2135–2143. https://doi.org/10.1021/acs.analchem.0c03942.
(109) Tose, L. V.; Ramirez, C. E.; Michalkova, V.; Nouzova, M.; Noriega, F. G.; Fernandez-Lima, F. Coupling Stable Isotope Labeling and Liquid Chromatography-Trapped Ion Mobility Spectrometry-Time-of-Flight-Tandem Mass Spectrometry for De Novo Mosquito Ovarian Lipid Studies. Anal. Chem. **2022**, 94 (16), 6139–6145. https://doi.org/10.1021/acs.analchem.1c05090.
(110) Gao, Z.; Li, L.; Chen, W.; Ma, Z.; Li, Y.; Gao, Y.; Ding, C.-F.; Zhao, X.; Pan, Y. Distinguishment of Glycan Isomers by Trapped Ion Mobility Spectrometry. Anal. Chem. **2021**, 93 (26), 9209–9217. https://doi.org/10.1021/acs.analchem.1c01461.
(111) Przybylski, C.; Bonnet, V. Discrimination of Isomeric Trisaccharides and Their Relative Quantification in Honeys Using Trapped Ion Mobility Spectrometry. Food Chem. **2021**, 341, 128182. https://doi.org/10.1016/j.foodchem.2020.128182.
(112) Ogata, K.; Ishihama, Y. Extending the Separation Space with Trapped Ion Mobility Spectrometry Improves the Accuracy of Isobaric Tag-Based Quantitation in Proteomic LC/MS/MS. Anal. Chem. **2020**, 92 (12), 8037–8040. https://doi.org/10.1021/acs.analchem.0c01695.
(113) Charkow, J.; Röst, H. L. Trapped Ion Mobility Spectrometry Reduces Spectral Complexity in Mass Spectrometry-Based Proteomics. Anal. Chem. **2021**, 93 (50), 16751–16758. https://doi.org/10.1021/acs.analchem.1c01399.
(114) Borotto, N. B.; Graham, K. A. Fragmentation and Mobility Separation of Peptide and Protein Ions in a Trapped-Ion Mobility Device. Anal. Chem. **2021**, 93 (29), 9959–9964. https://doi.org/10.1021/acs.analchem.1c01188.
(115) Ihling, C. H.; Piersimoni, L.; Kipping, M.; Sinz, A. Cross-Linking/Mass Spectrometry Combined with Ion Mobility on a TimsTOF Pro Instrument for Structural Proteomics. Anal. Chem. **2021**, 93 (33), 11442–11450. https://doi.org/10.1021/acs.analchem.1c01317.
(116) Larson, E. J.; Roberts, D. S.; Melby, J. A.; Buck, K. M.; Zhu, Y.; Zhou, S.; Han, L.; Zhang, Q.; Ge, Y. High-Throughput Multi-Attribute Analysis of Antibody-Drug Conjugates Enabled by Trapped Ion Mobility Spectrometry and Top-Down Mass Spectrometry. Anal. Chem. **2021**, 93 (29), 10013–10021. https://doi.org/10.1021/acs.analchem.1c00150.
(117) Brunner, A.; Thielert, M.; Vasilopoulou, C.; Ammar, C.; Coscia, F.; Mund, A.; Hoerning, O. B.; Bache, N.; Apalategui, A.; Lubeck, M.; Richter, S.; Fischer, D. S.; Raether, O.; Park, M. A.; Meier, F.; Theis, F. J.; Mann, M. Ultra-high Sensitivity Mass Spectrometry Quantifies Single-cell Proteome Changes upon Perturbation. Mol. Syst. Biol. **2022**, 18 (3). https://doi.org/10.15252/msb.202110798.
(118) Panczyk, E. M.; Snyder, D. T.; Ridgeway, M. E.; Somogyi, Á.; Park, M. A.; Wysocki, V. H. Surface-Induced Dissociation of Protein Complexes Selected by Trapped Ion Mobility Spectrometry. Anal. Chem. **2021**, 93 (13), 5513–5520. https://doi.org/10.1021/acs.analchem.0c05373.
(119) Jeanne Dit Fouque, K.; Kaplan, D.; Voinov, V. G.; Holck, F. H. V.; Jensen, O. N.; Fernandez-Lima, F. Proteoform Differentiation Using Tandem Trapped Ion Mobility, Electron Capture Dissociation, and ToF Mass Spectrometry. Anal. Chem. **2021**, 93 (27), 9575–9582. https://doi.org/10.1021/acs.analchem.1c01735.

(120) Miller, S. A.; Jeanne Dit Fouque, K.; Ridgeway, M. E.; Park, M. A.; Fernandez-Lima, F. Trapped Ion Mobility Spectrometry, Ultraviolet Photodissociation, and Time-of-Flight Mass Spectrometry for Gas-Phase Peptide Isobars/Isomers/Conformers Discrimination. J. Am. Soc. Mass Spectrom. **2022**, 33 (7), 1267–1275. https://doi.org/10.1021/jasms.2c00091.

(121) Wei, J.; Tang, Y.; Ridgeway, M. E.; Park, M. A.; Costello, C. E.; Lin, C. Accurate Identification of Isomeric Glycans by Trapped Ion Mobility Spectrometry-Electronic Excitation Dissociation Tandem Mass Spectrometry. Anal. Chem. **2020**, 92 (19), 13211–13220. https://doi.org/10.1021/acs.analchem.0c02374.

(122) Benigni, P.; Porter, J.; Ridgeway, Mark. E.; Park, Melvin. A.; Fernandez-Lima, F. Increasing Analytical Separation and Duty Cycle with Nonlinear Analytical Mobility Scan Functions in TIMS-FT-ICR MS. Anal. Chem. **2018**, 90 (4), 2446–2450. https://doi.org/10.1021/acs.analchem.7b04053.

(123) Jeanne Dit Fouque, K.; Garabedian, A.; Leng, F.; Tse-Dinh, Y.-C.; Ridgeway, M. E.; Park, M. A.; Fernandez-Lima, F. Trapped Ion Mobility Spectrometry of Native Macromolecular Assemblies. Anal. Chem. **2021**, 93 (5), 2933–2941. https://doi.org/10.1021/acs.analchem.0c04556.

(124) Jeanne Dit Fouque, K.; Sipe, S. N.; Garabedian, A.; Mejia, G.; Su, L.; Hossen, M. L.; Chapagain, P. P.; Leng, F.; Brodbelt, J. S.; Fernandez-Lima, F. Exploring the Conformational and Binding Dynamics of HMGA2·DNA Complexes Using Trapped Ion Mobility Spectrometry–Mass Spectrometry. J. Am. Soc. Mass Spectrom. **2022**, 33 (7), 1103–1112. https://doi.org/10.1021/jasms.2c00101.

(125) Liu, F. C.; Ridgeway, M. E.; Park, M. A.; Bleiholder, C. Tandem Trapped Ion Mobility Spectrometry. The Analyst **2018**, 143 (10), 2249–2258. https://doi.org/10.1039/C7AN02054F.

(126) Liu, F. C.; Ridgeway, M. E.; Park, M. A.; Bleiholder, C. Tandem-Trapped Ion Mobility Spectrometry/Mass Spectrometry (t TIMS/MS): A Promising Analytical Method for Investigating Heterogenous Samples. The Analyst **2022**, 147 (11), 2317–2337. https://doi.org/10.1039/D2AN00335J.

(127) Liu, F. C.; Kirk, S. R.; Caldwell, K. A.; Pedrete, T.; Meier, F.; Bleiholder, C. Tandem Trapped Ion Mobility Spectrometry/Mass Spectrometry (TTIMS/MS) Reveals Sequence-Specific Determinants of Top-Down Protein Fragment Ion Cross Sections. Anal. Chem. **2022**, 94 (23), 8146–8155. https://doi.org/10.1021/acs.analchem.1c05171.

(128) Liu, F. C.; Ridgeway, M. E.; Winfred, J. S. R. V.; Polfer, N. C.; Lee, J.; Theisen, A.; Wootton, C. A.; Park, M. A.; Bleiholder, C. Tandem-trapped Ion Mobility Spectrometry/Mass Spectrometry Coupled with Ultraviolet Photodissociation. Rapid Commun. Mass Spectrom. **2021**, 35 (22). https://doi.org/10.1002/rcm.9192.

(129) Fernandez-Lima, F.; Kaplan, D. A.; Suetering, J.; Park, M. A. Gas-Phase Separation Using a Trapped Ion Mobility Spectrometer. Int. J. Ion Mobil. Spectrom. **2011**, 14 (2–3), 93–98. https://doi.org/10.1007/s12127-011-0067-8.

Chapter 2. Are the Gas-Phase Structures of Molecular Elephants Enduring or Ephemeral? Results from Time-Dependent, Tandem Ion Mobility

2.1 Abstract

The structural stability of biomolecules in the gas phase remains an important topic in mass spectrometry (MS) applications for structural biology. Here, we evaluate the structural stability of native-like protein ions using time-dependent, tandem ion mobility (IM). In tandem IM experiments, ions of interest are mobility-selected after a first dimension of IM and trapped for various periods of time, from 14 to 14 342 ms. Time-dependent collision cross section distributions are determined from separations in a second dimension of IM. In these experiments, monomeric protein ions exhibited structural changes specific to both protein and charge state, whereas large protein complexes did not undergo resolvable structural changes on the timescale of the experiment. We performed energy-dependent experiments, i.e., collision induced unfolding, as a comparison for time-dependent experiments to understand the extent of unfolding. Collision cross section values observed in energy-dependent experiments were significantly larger than those observed in time-dependent experiments, indicating that the structures observed in time-dependent experiments remain kinetically trapped and retain some memory of their solution-phase structure. Although the structural evolution should be considered for highly charged, monomeric proteins, these experiments demonstrate the remarkable stability of gas-phase biomolecules offering promise for their analysis in native mass spectrometry-enabled structural biology.

2.2 Introduction

Native mass spectrometry (MS) has emerged as a useful addition to the structural biology toolkit, both as a standalone technique as well as through recent integration with high-resolution imaging.[1] For example, MS can reduce sample heterogeneity in electron microscopy by mass-selecting and depositing ions from a native electrospray ion beam, enabling electron microscopy imaging of protein complexes.[2,3] Native electrospray beam deposition was also used to probe the flexibility of a monoclonal antibody with low-energy electron holography, a single-molecule imaging technique that requires ultrapure substrates.[4] Additionally, free-electron lasers probe solvent-free biomolecules;[5] an electrospray ionization source reduced nonvolatile contaminants to enable the analysis of 35-nm biomolecules, three orders of magnitude smaller than previously possible.[6] Beyond imaging techniques, ion mobility (IM) is a gas-phase structural technique that has experienced increased adoption in recent years.[7,8] In IM, charged ions undergo collisions with a neutral background gas as they traverse a drift region under the influence of an applied electric field. The amount of time spent in the drift region is inversely proportional to the ion's mobility (K), from which a collision cross section (Ω) value can be determined.[9] Results from IM-MS studies have been used to inform structural modeling,[10–12] characterize quaternary structure[13,14] and ligand-induced conformational changes,[15,16] and probe the transient species involved in protein-protein interactions and their folding intermediates.[17–19]

To increase the utility of IM-MS, next-generation IM measurements aim to differentiate previously unresolved structures by leveraging high-resolution and multidimensional separations. The resolving power of a single conformation in IM typically increases with the square root of the path length or separation time. For example, the Waters Cyclic IMS system can subject ions to an arbitrary number of passes through an off-axis ring to increase the path

length and thus the resolution of the separation.[20] Using multiple passes through a serpentine path, Structures for Lossless Ion Manipulations (SLIM)[21] has achieved resolving powers of ~400-600 over a 679.5 m pathlength separation.[22] These instrument architectures can also enable IM-IM, or tandem IM, in which two IM separations are separated by a mobility-dependent selection to increase the selectivity of the measurement. Initially demonstrated on sequential, serial IM components,[23–25] these new instrument geometries provide flexible tandem IM operation modes.[20,26] Furthermore, both the Waters Cyclic IMS and the SLIM architecture have the capability not only for IM-IM, but also for IM^n, where ions can be selected, activated, and analyzed by subsequent dimensions of IM.

Although it is generally accepted that native-like ions can be generated from gentle ionization sources,[27,28] there has been a concerted experimental effort devoted to understanding the structural evolution of biomolecules in the absence of solvent. IM-MS,[28–30] molecular dynamics simulations,[31–33] electron capture dissociation,[34,35] and hydrogen-deuterium exchange[36] have been used to analyze the structures and stabilities of gas-phase biomolecules. Relative to traditional, single-dimension IM, next-generation IM measurements access longer timescales, *e.g.*, hundreds of milliseconds and longer, which provide additional opportunity for the properties of ions to change during measurements. Based on a meta-analysis, Breuker and McLafferty proposed a timeline for the gas-phase unfolding of protein ions where after initial desolvation events, side-chain collapse stabilizes the native-like structure before the loss of hydrophobic and electrostatic interactions result in structural rearrangements to stable gas-phase structures.[37] That analysis suggests that the timescales associated with next-generation IM separations may result in significant to total loss of native structure.

The objective of this study is to characterize the retention of native-like structures over a wide range of timescales to provide context for the information content of next-generation IM measurements. Here, we survey the gas-phase structural stabilities of a wide range of native-like protein ions using time-dependent, tandem IM measurements. Analytes ranged from small monomeric proteins to large multimeric protein complexes. Apparent Ω values of ions are monitored in time-dependent, tandem IM experiments to determine how Ω values change with time. Complementary, energy-dependent experiments are used to understand potential unfolding pathways and the structural distributions of these ions at equilibrium.

2.3 Methods

2.3.1 Sample Preparation and Ionization. Proteins were purchased from Sigma-Aldrich. Native-like protein ions were generated using electrokinetic nanoelectrospray ionization[38] from 10 to 20 μM protein in aqueous 200 mM ammonium acetate adjusted to pH 7.0. IgG3 samples were also buffer exchanged using Micro Bio-Spin 6 columns (Bio-Rad, Hercules, CA) equilibrated with that same solution.

2.3.2 Time-dependent, Tandem IM. We recently reported a flexible, modular instrument for IM-MS comprised of 12 modules,[26] as shown and described in Figure 2.1. The modules were constructed using the structures for lossless ion manipulations (SLIM) architecture; their use for native IM-MS has been described previously.[26,39,40] Ion packets are prepared for time-dependent, tandem IM experiments by diverting 12.5 ms of the incident ion beam to a junction trap at the end of the first module (^{1}M). A junction trap is a potential well that confines ions when the input voltage of a board is biased relative to the output voltage of the preceding board.[41] The initial ion packet is released from the ^{1}M and is separated in the first dimension of IM (^{1}D), which consists

of the ^{2}M through the middle of the ^{7}M. Voltage modulation at the intersecting paths of the ^{7}M is used to divert ions of interest to the orthogonal path for further analysis, whereas other ions continue to a collection electrode at the end of the collinear path of the ^{7}M. In these experiments, the timing of those voltages is used to isolate ions of a single charge state based on their mobility in the ^{1}D. Selected ions are then trapped at the interface between the ^{7}M and ^{8}M for variable delay times, defined as the amount of time between ion selection and the beginning of the second dimension of IM (^{2}D).[40] After the delay time, ions are released from the junction trap by reducing the bias between the ^{7}M and ^{8}M. Ions are then separated along a path from the ^{8}M to the ^{12}M. In these experiments, the drift fields in the modules that comprise the ^{1}D were 4 V cm^{-1}. The drift field in the orthogonal region connecting the ^{7}M and ^{8}M was 3.75 V cm^{-1}, and the drift field in the ^{2}D was 5 V cm^{-1}. Drift fields were selected to optimize accuracy of Ω measurements while reducing voltages of components relative to ground. In these experiments, the TOF pusher was used as the master clock; delay times are the result of the timing of selection of specific precursor ions and its relation to a preset timing scheme used to manage digitizer memory. Additional information on the 12-module array, ion packet generation, and junction trapping conditions is provided in the *Supporting Information*.

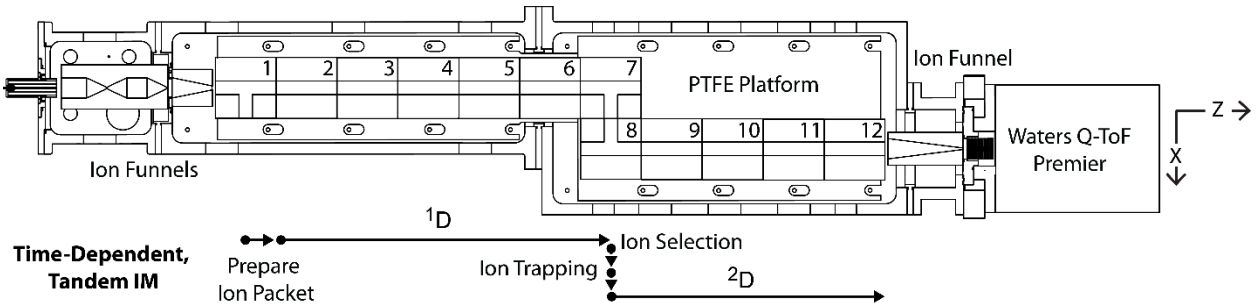

Figure 2.1. Schematic of the 12-module array used for these experiments, which was reported recently.[26] Ions generated at atmospheric pressure pass through a stainless-steel capillary heated to 80 °C (*far left*), a hourglass ion funnel, and a rectangular funnel prior to the array of 12 modules. Ions are transported through these modules using electrostatic fields, not traveling waves, and data analysis is like that of drift tubes. The first module (^{1}M), ^{7}M, and ^{8}M are tee modules, whereas the remaining modules are linear modules. Finally, ions pass through a circular ion funnel that interfaces with the mass analyzer. Ion packets are prepared on the ^{1}M, then separated in the first dimension of IM (^{1}D) prior to selection at the ^{7}M. Ions are then trapped at the interface between the ^{7}M and ^{8}M for varying periods of time before separation in a second dimension of IM (^{2}D) prior to mass analysis.

2.3.3 Collision-Induced Unfolding (CIU). Energy-dependent experiments were conducted on a Waters Synapt G2 HDMS hybrid mass spectrometer (Waters Co., Wilmslow, UK) modified with an RF-confining drift cell containing nitrogen gas, as described previously.[42] CIU was monitored as a function of the voltage drop used to accelerate ions into the collision cell prior to IM separation.

2.3.4 Determining Apparent Ω *Distributions*. Both experiments separate ions using electrostatic fields, not traveling waves, in nitrogen gas and data analysis is like that of drift

tubes. For time-dependent measurements, we derived a relationship between the applied drift field (*E*), the length of each region comprising the ^{2}D, the observed arrival times, and *K* as described in the *Supporting Information*. Distributions of *K* were converted to apparent Ω distributions using the Mason-Schamp equation.[9] For CIU experiments, we used field-dependent measurements to convert arrival-times to apparent Ω distributions as described previously.[43]

2.4 Results and Discussion

Current- and next-generation IM measurements access a wide range of timescales (*e.g.*, 10^{-3} to 10^{1} s). Therefore, it is increasingly important to understand the extent to which the structures of native-like ions evolve over these time scales. To this end, we used time-dependent, tandem IM to survey the gas-phase stabilities of a range of native-like ions. These analytes were selected to encompass a broad range of properties, including oligomeric state, mass, and collision cross sections (Ω) as shown in Figure 2.2. We first present the results from time- and energy dependent experiments, and then compare those results. To provide additional context for the time-dependent results, we report results from a kinetic model, compare those results to other rates/timescales reported previously, and discuss their broader implications.

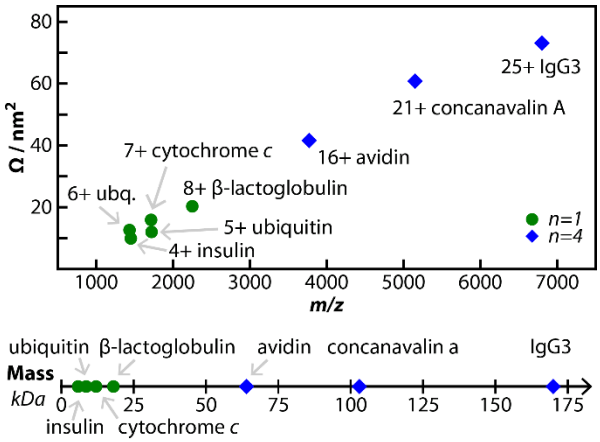

Figure 2.2 The properties of the native-like ions analyzed in these time-dependent, tandem IM experiments. (*Top*) Reported collision cross sections in nitrogen (Ω) of the selected charge states versus their *m*/*z* values; *n* represents the oligomeric state of the protein. Avidin and concanavalin A are homotetramers, whereas IgG3 is composed of two heavy and two light peptide chains that are connected through covalent and noncovalent interactions. (*Bottom*) The proteins analyzed in this study plotted by their mass.

2.4.1 Time-Dependent Analysis of Native-Like, Monomeric Protein Ions. Native-like ions of 5+ and 6+ ubiquitin, 4+ insulin, 7+ cytochrome *c*, and 8+ β-lactoglobulin were subjected to time-dependent, tandem IM experiments. Those results are shown in the positive intensity traces in Figure 2.3; the corresponding negative intensity traces are for complementary energy-dependent experiments that will be the focus of the next section. In time-dependent experiments, ions are separated in the first dimension of IM (^{1}D, Figure 2.1). Ions with the charge states of interest are selected at the seventh module (^{7}M) and trapped at the interface between the ^{7}M and ^{8}M as a function of time prior to release into the second dimension of IM (^{2}D). The effective temperatures of the trapped ions are estimated to be near, albeit somewhat above ambient temperature; the methodology[44] and results of those estimates are discussed in the *Supporting Information*. The delay time describes the time between selection and ^{2}D analysis.[40] For monomeric proteins, the longest delay times ranged from ~9-14 s. Maximum delay times were limited both by charge-transfer reactions that depleted the precursor ions, as well as nonspecific adduction that increased the mass of the selected ions and degraded the signal-to-noise ratio. Median Ω values, $\widetilde{\Omega}$, were determined from the cumulative distribution function of the apparent

Ω distributions. The $\widetilde{\Omega}$ extracted from the ion populations with the shortest delay times agree with Ω values reported previously for native-like ions,[42,45] indicating that the initial populations in these experiments maintain compact, native-like structures (see *Supporting Information*). Technical replicates of time-dependent experiments taken across multiple days show that these results are highly reproducible (Figure S2).

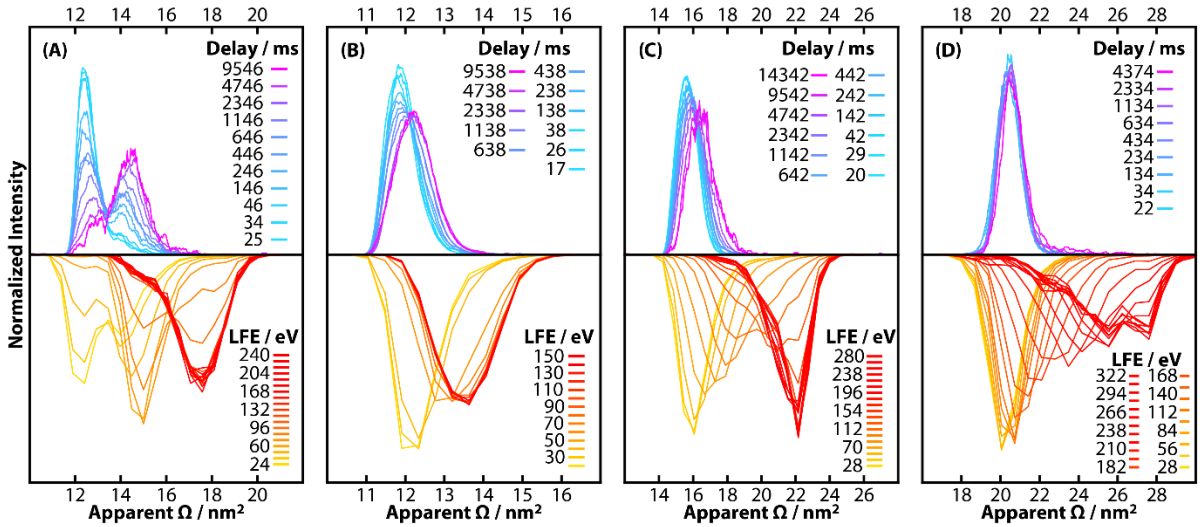

Figure 2.3. Apparent Ω distributions determined from time-dependent (positive intensity, cool color scheme) and energy-dependent (negative intensity, hot color scheme) experiments for (A) 6+ ubiquitin, (B) 5+ ubiquitin, (C) 7+ cytochrome *c*, and (D) 8+ β-lactoglobulin. In the panels for the time-dependent experiments (*top row*), the delay time describes the time between ion selection and ion mobility analysis in the ^{2}D. In the panels for the energy-dependent experiments (*bottom row*), results are plotted in terms of the laboratory-frame energy (LFE) for each experiment. 4+ insulin was characterized in both time-dependent and energy-dependent experiments; apparent Ω distributions were independent of both time and energy (Figure S1).

Three of the five monomeric analytes exhibit evidence for structural changes in these time-dependent experiments, *i.e.*, the apparent Ω distributions depended on the delay time. Figure 2.3A shows results for 6+ ubiquitin. At the shortest delay time, the initial ion population exhibits a compact population centered near 12.5 nm^2, as well as the presence of a small shoulder resulting from ions with larger Ω values. With increasing delay time, the compact population is depleted in favor of an extended population that exhibits a maximum $\tilde{\Omega}$ above 14 nm^2. After ~9 s of trapping, the extended population is predominant. The structural transition for 6+ ubiquitin appears to be a discrete transition between two structures that are well resolved in the ^{2}D.

Other monomeric proteins underwent more subtle structural changes. Figure 2.3B shows that the time-dependent apparent Ω distributions of 5+ ubiquitin shift monotonically towards larger $\tilde{\Omega}$ with increasing delay time. The initial population exhibits a $\tilde{\Omega}$ of 12.0 nm^2; after ~14 seconds of trapping in the gas-phase, that value increases to 12.3 nm^2. The apparent Ω distributions of 7+ cytochrome *c* also exhibit subtle changes with increasing delay times (Figure 2.3C). The $\tilde{\Omega}$ of the initial ion population is 15.7 nm^2, and increases to 16.6 nm^2 after ~14 s of trapping. These results for 7+ cytochrome *c* are consistent with previous data acquired in analogous experiments performed using a 6-module array.[40] Both 5+ ubiquitin and 7+ cytochrome *c* appear to evolve through a continuum of conformations or perhaps a small number of conformers that are not resolved in these IM experiments. Figure 2.3D shows that the initial ion population for 8+ β-lactoglobulin exhibits a $\tilde{\Omega}$ of 20.5 nm^2 and that the apparent Ω distributions appear to be largely independent of the delay time, even after 4 s. 4+ insulin (Figure S1) also did not undergo any significant changes in mobility as a function of delay time.

These time-dependent, tandem IM experiments show that the magnitude and timescales of the structural changes for these native-like, monomeric protein ions depend on the identity and

charge state of the ion. To evaluate the magnitude of these changes, we will characterize these same ions using energy-dependent IM experiments and then compare the results from the time- and energy-dependent experiments.

2.4.2 Energy-Dependent Analysis of Native-Like, Monomeric Protein Ions. Collision-induced unfolding (CIU) probes the structures of ions as a function of the energy deposited through collisional activation prior to IM analysis.[46,47] Activated ions can overcome isomerization barriers to form additional structures that appear to be stable for at least milliseconds.[47] Here, we will use CIU to characterize the same protein ions that were analyzed using time-dependent experiments, which did not include intentional collisional activation.

The apparent Ω distributions generated from CIU experiments are shown in negative, normalized intensities in Figure 2.3. Figure 2.3A shows that at the lowest-energy, 6+ ubiquitin exhibits a bimodal distribution with a more-compact population near 12.5 nm^2 and more-extended population centered near 14 nm^2. With increasing energy, the compact population is depleted in favor of more extended population centered near 15 nm^2. Finally, as the laboratory-frame energy is increased above 96 eV, the population centered near 15 nm^2 is depleted in favor of that centered near 18 nm^2. That distribution centered near 18 nm^2 persists with increasing energy until fragmentation occurs. The persistence of that distribution suggests those ions populated the gas-phase equilibrium (or quasi-equilibrium)[48] distribution of structures.

For 5+ ubiquitin and 7+ cytochrome *c*, the apparent Ω distributions widen and shift towards higher Ω values with increasing energy. For 5+ ubiquitin, the initial ion population is centered near 12 nm^2, whereas the most extended population is centered between 13 and 14 nm^2. For 7+ cytochrome *c*, the initial ion population observed near 16 nm^2 is depleted in favor of a distribution centered near 22 nm^2. For 8+ β-lactoglobulin, the initial population was centered

near 21 nm^2. The initial changes with increasing energy are small, but for laboratory-frame energies above 100 eV, much larger structures were observed. At the highest energies, a wide distribution was observed with a $\widetilde{\Omega}$ near 26 nm^2 and a maximum value near almost 28 nm^2. Whereas all other monomeric ions underwent structural evolution in these energy-dependent experiments, the apparent **Ω** distributions of 4+ insulin appears to be independent of energy (Figure S1).

2.4.3 Native-Like, Monomeric Protein Ions Can Retain Memories of their Original Structures for Many Seconds in the Gas Phase. The apparent **Ω** distributions from time-dependent experiments can be compared to those from energy-dependent experiments to provide context for the structural transitions observed in absence of intentional collisional activation. The change in $\widetilde{\Omega}$ is quantified by:

$$Relative\ \Omega = \frac{\widetilde{\Omega}_{final}}{\widetilde{\Omega}_{initial}} \tag{2.1}$$

where "initial" describes the ion population that experienced the shortest delay time or the lowest laboratory-frame energies and "final" describes the ion population that experienced the longest delay time or the highest laboratory-frame energies.

Figure 2.4 shows the relative **Ω** values from time-dependent and energy-dependent experiments for each of the monomeric proteins analyzed. Energy-dependent experiments resulted in relative **Ω** values of 100%, 110%, 136%, 134%, and 127% for 4+ insulin, 5+ ubiquitin, 6+ ubiquitin, 7+ cytochrome *c*, and 8+ β-lactoglobulin, respectively. These same proteins exhibited relative **Ω** values of 100%, 102%, 114%, 105%, and 101% in time-dependent experiments. 4+ insulin was the only monomeric protein that did not exhibit change during these experiments. This ion may adopt a stable distribution of structures prior to analysis, or alternatively, the changes that do occur do not affect the mobility of the ions. As no changes in

mobility are observed in energy-dependent experiments, 4+ insulin serves as a negative control for time-dependent experiments. For the other monomeric protein ions, energy-dependent experiments yield a greater increase in Ω than the corresponding time-dependent experiments. For example, 8+ β-lactoglobulin did not exhibit resolvable structural changes in time-dependent experiments but exhibited significant unfolding in energy-dependent experiments (Figure 2.3D). 6+ ubiquitin underwent a single discrete transition in time-dependent experiments, and then exhibited evidence for the formation of an even larger, gas-phase annealed structure in energy-dependent experiments (Figure 2.3A).

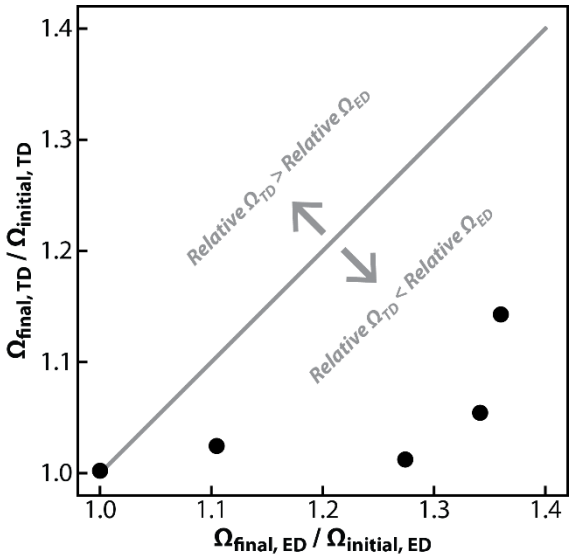

Figure 2.4. Relative Ω values in time-dependent (TD) experiments as a function of relative apparent Ω values from energy-dependent (ED) experiments for each monomeric protein ion studied. The plotted line has a slope of 1.

The large increases in apparent Ω observed in these energy-dependent experiments are consistent with increases in drift time reported in CIU experiments in the literature.[49] Since the ions at the highest energies in the CIU experiments exhibited similar apparent Ω distributions

over a wide range of energies, that suggests that a gas-phase equilibrium (or quasi-equilibrium)[48] distribution of structures was adopted in those experiments. Therefore, the $\widetilde{\Omega}_{final}$ values for the CIU experiments represent an upper limit; smaller $\widetilde{\Omega}_{final}$ values for the time-dependent experiments indicates that structures remain kinetically trapped and retain some memory of their original structures. From these results, it can be shown that native-like protein ions undergo time-dependent structural changes that are specific to both protein and charge state. However, the observable structural changes do not appear to correlate to a full rearrangement to larger, more stable gas-phase structures accessed in energy-dependent experiments. Although the time-dependent structural evolutions observed in our time-dependent experiments are significant and have implications for IM measurements of native-like ions, the small magnitude of those changes relative to the most-stable, gas-phase annealed structures points to a remarkably long memory of the native-like fold in the gas phase.

2.4.4 Native-Like Ions of Protein Complexes Appear to Have Mobilities that are Independent of Time for at Least a Second in the Gas Phase. Using time-dependent, tandem IM, we also characterized the gas-phase stabilities of 16+ avidin, 21+ concanavalin A, and 25+ IgG3. Avidin and concanavalin A are noncovalently bound homotetramers. IgG3 is comprised of two heavy and two light chains that are connected through covalent and noncovalent interactions; the gas-phase structures and dynamics of antibodies like IgG3 are of particular interest because of the potential applications of IM-MS in the development and characterization of biopharmaceuticals.[33,50,51] The apparent **Ω** distributions of these ions are shown in Figure 2.5 for delay times up to ~2 s. As with monomeric proteins, delay times were limited by charge-transfer reactions as well as non-specific adduction within the trap; higher mass species underwent more rapid charge reduction, consistent with larger **Ω** values (Figure 2.2), shorter mean free paths, and

concomitantly higher collision frequencies. Whereas the distributions for most monomeric proteins exhibited some degree of change as a function of time (Figure 2.3), the distributions for these larger native-like ions appear to be essentially independent of time. The apparent **Ω** distributions remain well overlaid and $\tilde{\Omega}$ vary by less than 1%, even after more than 1 s in the gas phase.

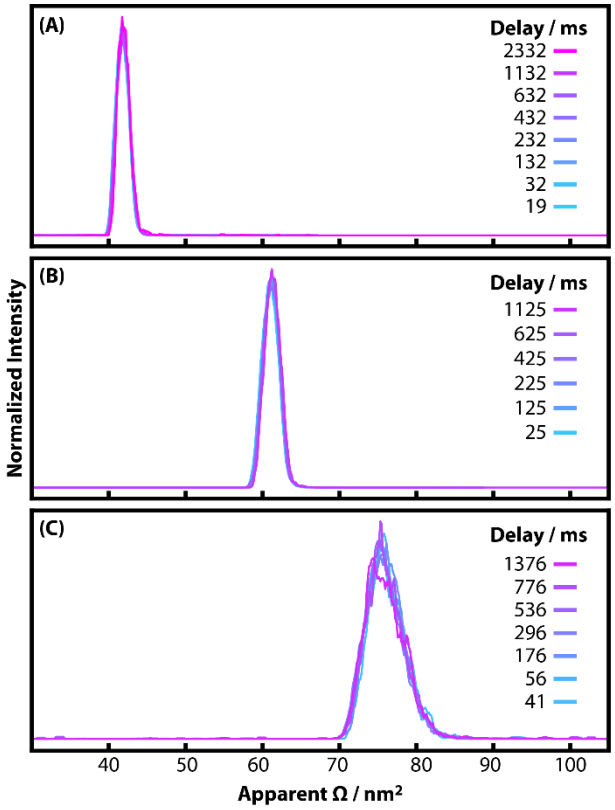

Figure 2.5. Apparent **Ω** distributions as a function of delay time for 16+ avidin (A), 21+ concanavalin A (B), 25+ IgG3 (C). Each distribution is the average of three replicate measurements and is normalized by area.

One possibility for the lack in change of **Ω** is that the ions probed in these experiments have already adopted the most stable equilibrium structure, rather than kinetically trapped, native-like structures. To determine whether the ions probed in this experiment are native-like,

observed $\widetilde{\Omega}_{initial}$ values can be compared to previous Ω measurements of native-like ions. The $\widetilde{\Omega}_{initial}$ values observed in these experiments are 41.9, 61.3, and 75.5 nm^2 for 16+ avidin, 21+ concanavalin A, and 25+ IgG3, respectively. For avidin and concanavalin A, observed $\widetilde{\Omega}_{initial}$ values are within 1% of reported native-like Ω values measured on an RF-confining drift cell,[45] whereas the observed $\widetilde{\Omega}_{initial}$ value for 25+ IgG3 agrees well with previous measurements that used traveling-wave IM.[52] Furthermore, these proteins have been characterized previously using CIU experiments and those studies reported significant increases in Ω with increasing energy.[46,51,53] For example, 16+ avidin exhibited a ~42% increase in $\widetilde{\Omega}$ with increasing energy.[43] With increasing energy, four distinct gas-phase populations with significantly different drift times were observed for 15+ avidin and 19+ concanavalin A.[46] Studies of the CIU of antibodies also observe the appearance of multiple extended populations, with IgG3 exhibiting an approximate 45% increase in the arrival time for its most extended population.[51,53] If the ions probed in these experiments had already adopted their global-minimum structures, observed $\widetilde{\Omega}_{initial}$ values would differ greatly from previous measurements.

Although it is possible that these protein complexes undergo small rearrangements on these timescales that do not affect the measured mobility, the well-overlaid apparent Ω distributions observed in these time-dependent experiments are evidence that these large, multimeric ions are stable in the gas-phase at near ambient temperatures for >1 s. It follows that gas-phase stability likely increases with *m*/*z*, consistent with enhanced charge solvation in the structures of larger multimeric protein ions (as well as the largest monomeric protein ion studied, β-lactoglobulin) than their smaller, monomeric counterparts.

2.4.5 Kinetics of Observed Structural Transitions and Comparison to Previous Experiments. The relative Ω values are shown as a function of delay time in Figure 2.6, revealing

the stark contrast between the ions characterized in this study. Monomeric proteins exhibit varied gas-phase stabilities, and analytes that undergo structural evolution exhibit the greatest change in apparent Ω at the shortest delay times. Conversely, the native-like structures of each of the multimeric proteins are stable for seconds in the gas phase.

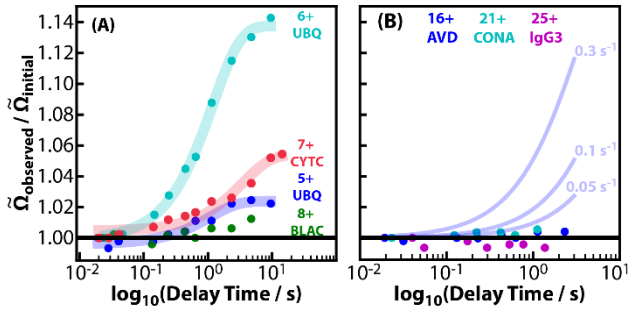

Figure 2.6. Relative $\widetilde{\Omega}$ values as a function of the delay time for monomeric (A) and multimeric (B) proteins. Transparent lines are from kinetic modeling of the data (see *Supporting Information*). For monomeric proteins, kinetic models were fit to experimental data to determine rate constants (Table S3), while the models in Panel B describe transitions from the observed $\widetilde{\Omega}_{initial}$ to a final extended state at a given rate constant.

To provide context for structural evolution observed in this study, we modeled the kinetics of structural transitions observed in time-dependent, tandem IM assuming a two-state transition and first-order kinetics (see *Supporting Information*). We parameterized this model to reproduce the $\widetilde{\Omega}$ determined as a function of delay time. This process yielded rate constants of 0.3, 0.9, and 0.8 s^{-1} for 7+ cytochrome *c*, 5+ ubiquitin, and 6+ ubiquitin, respectively. For 7+ cytochrome *c*, this rate is similar to that (0.31±0.06 s^{-1}) determined using analogous experiments (but different kinetic modeling) performed using a 6-module array.[40] Although no rate constant was reported, 7+ cytochrome *c* ions trapped in a cyclic IMS system underwent structural changes

of a similar magnitude over several hundred milliseconds.[49] In earlier investigations, the compact population of 7+ cytochrome *c* ions stored in a Paul trap exhibited a rate of depletion of 40 s^{-1},[30] which is significantly faster than the recent studies. This was attributed to possible differences in effective temperatures of ions between the experiments, [40] as well as differences in the solutions from which ions were generated.[40] Despite differences in rate constants, all studies observed time-dependent structural changes for 7+ cytochrome *c*.

For 6+ ubiquitin generated from a solution of 49:49:2 by volume water:methanol:acetic acid and stored in a Paul trap for variable amounts of time, a compact "A" state remained the dominant feature at all trapping times; an extended "B" state increased in relative abundance from 15% to 20% over the course of the experiment at a reported rate of 0.2 s^{-1}.[29] This rate is less than that determined for 6+ ubiquitin in these experiments (0.8 s^{-1}). One possibility is that different structures were probed in the two experiments. To enable a more direct comparison between the current study (based on IM in nitrogen gas) and the earlier study (based on IM in helium gas),[29] we estimated Ω_{He} values based on the Ω_{N2} values determined here using a previously reported relationship[45] as described in the *Supporting Information*. From this analysis shown in Figure S3, the most compact states in both studies are well-aligned, whereas the more extended state in our time-dependent experiments falls between the two partially unfolded "B" states observed in the previous work. It is challenging to identify a single, compelling origin for these differences, but some potential origins are discussed with Figure S3. More generally, these differences illustrate the need for future time-dependent measurements that more directly characterize the effects of solution conditions.

Because none of the larger protein ions appeared to convert to populations with larger Ω values, we instead estimated the upper limit of the depletion rate constant for the initial

population in time-dependent experiments. We used the estimated $\widetilde{\Omega}$ for the equilibrium conformation of 16+ avidin observed in previous energy-dependent experiments (50 nm^2).[43] Using first-order kinetics, we show relative $\widetilde{\Omega}$ that would be observed at various rate constants (transparent lines, Figure 2.6B). We found that 0.05 s^{-1} represents a conservative upper limit for the depletion rate of the initial population of 16+ avidin (Figure 2.6). This approach provides quantitative evidence that the multimeric protein ions probed in this study will retain elements of native-like structure even over the longest timescales envisioned for next-generation IM and other native MS-enabled structural biology techniques.

2.5 Conclusions

We surveyed the gas-phase structural stabilities of a wide range of native-like protein ions using time-dependent, tandem IM measurements on a modular instrument. Monomeric proteins exhibited a range of gas-phase stabilities, with three of the five analytes undergoing expansion to larger $\widetilde{\Omega}$ on the millisecond to second timescale (Figure 2.3, positive intensity traces). The structural changes observed in time-dependent experiments were smaller than those observed in energy-dependent experiments with monomeric proteins (Figure 2.4), which indicates that the structures retain significant memory of their solution-phase structure even after up to ~14 s in the gas phase. Whereas monomeric proteins exhibited varied gas-phase stabilities, the apparent $\boldsymbol{\Omega}$ of multimeric proteins were independent of delay time (Figure 2.5). We modeled the kinetics of the observed structural transitions (Figure 2.6) and compared rates of conversion with those reported in the literature.

These results provide context for future multidimensional IM experiments. For example, the apparent $\boldsymbol{\Omega}$ distributions of 6+ ubiquitin exhibit features for two populations, whose relative

abundance would change on the timescale of many experiments. The apparent Ω distributions of 5+ ubiquitin and 7+ cytochrome *c* exhibit comparatively subtle changes with increasing time, but the nature of the changes would be extremely challenging to identify and characterize using single-dimension IM experiments with long timescales. Although traditional IM-MS measurements have failed to differentiate closely related mAbs,[51] our findings suggest that those structures are very stable in the gas phase and may be amenable to multidimensional IM experiments that incorporate orthogonal probes of ion structure. Additionally, the results presented here indicate that native MS-enabled structural biology techniques can probe native-like structures with high resolution, especially when analyzing protein complexes with short gas-phase ion lifetimes.

Based on a meta-analysis of results from a variety of experimental and computational studies, Breuker and McLafferty proposed that most noncovalent interactions present in native biomolecules would be lost in subsecond timescales and that new gas-phase structures would be predominate in the second to minute timescales.[37] Although those predictions may be true for the highly-charged, monomeric protein ions that formed the basis of that meta-analysis, the present studies show that protein ions with larger *m*/*z* values and sizes (Figure 2.2) can have remarkable stabilities that kinetically trap elements of their original structures for seconds in the gas phase. These trends suggest that higher-*m*/*z* ions provide better solvation for excess charges and have higher isomerization barriers. With these considerations in mind, the structural evolution of large, multimeric protein ions likely occurs on the upper end of the timescales proposed by Breuker and McLafferty.[37] More generally, these results support the expanded use of next-generation IM experiments in structural MS by providing a framework for designing and interpreting the results of experiments with longer timescales.

2.6 Supporting Information. Supporting Information associated with this chapter can be found in Appendix A. Supporting Information includes Additional Methods, Tables S1 to S2, and Figures S1 to S3.

2.7 Acknowledgments. Research reported in this publication was supported by the National Institute of General Medical Sciences of the National Institutes of Health through award number R01GM130708 and by the National Science Foundation through awards 1807382 and 2203513 from the Division of Chemistry, with partial co-funding from the Division of Molecular and Cellular Biosciences.

2.8 References

(1) Liko, I.; Allison, T. M.; Hopper, J. T.; Robinson, C. V. Mass Spectrometry Guided Structural Biology. *Curr. Opin. Struct. Biol.* **2016**, *40*, 136–144. https://doi.org/10.1016/j.sbi.2016.09.008.

(2) Esser, T. K.; Böhning, J.; Fremdling, P.; Agasid, M. T.; Costin, A.; Fort, K.; Konijnenberg, A.; Gilbert, J. D.; Bahm, A.; Makarov, A.; Robinson, C. V.; Benesch, J. L. P.; Baker, L.; Bharat, T. A. M.; Gault, J.; Rauschenbach, S. Mass-Selective and Ice-Free Electron Cryomicroscopy Protein Sample Preparation via Native Electrospray Ion-Beam Deposition. *PNAS Nexus* **2022**, *1* (4), pgac153. https://doi.org/10.1093/pnasnexus/pgac153.

(3) Westphall, M. S.; Lee, K. W.; Salome, A. Z.; Lodge, J. M.; Grant, T.; Coon, J. J. Three-Dimensional Structure Determination of Protein Complexes Using Matrix-Landing Mass Spectrometry. *Nat. Commun.* **2022**, *13* (1), 2276. https://doi.org/10.1038/s41467-022-29964-4.

(4) Ochner, H.; Szilagyi, S.; Abb, S.; Gault, J.; Robinson, C. V.; Malavolti, L.; Rauschenbach, S.; Kern, K. Low-Energy Electron Holography Imaging of Conformational Variability of Single-Antibody Molecules from Electrospray Ion Beam Deposition. *Proc. Natl. Acad. Sci.* **2021**, *118* (51), e2112651118. https://doi.org/10.1073/pnas.2112651118.

(5) Hajdu, J. Single-Molecule X-Ray Diffraction. *Curr. Opin. Struct. Biol.* **2000**, *10* (5), 569–573. https://doi.org/10.1016/S0959-440X(00)00133-0.

(6) Bielecki, J.; Hantke, M. F.; Daurer, B. J.; Reddy, H. K. N.; Hasse, D.; Larsson, D. S. D.; Gunn, L. H.; Svenda, M.; Munke, A.; Sellberg, J. A.; Flueckiger, L.; Pietrini, A.; Nettelblad, C.; Lundholm, I.; Carlsson, G.; Okamoto, K.; Timneanu, N.; Westphal, D.; Kulyk, O.; Higashiura, A.; van der Schot, G.; Loh, N.-T. D.; Wysong, T. E.; Bostedt, C.; Gorkhover, T.; Iwan, B.; Seibert, M. M.; Osipov, T.; Walter, P.; Hart, P.; Bucher, M.; Ulmer, A.; Ray, D.; Carini, G.; Ferguson, K. R.; Andersson, I.; Andreasson, J.; Hajdu, J.; Maia, F. R. N. C. Electrospray Sample Injection for Single-Particle Imaging with x-Ray Lasers. *Sci. Adv.* **2019**, *5* (5), eaav8801. https://doi.org/10.1126/sciadv.aav8801.

(7) Lanucara, F.; Holman, S. W.; Gray, C. J.; Eyers, C. E. The Power of Ion Mobility-Mass Spectrometry for Structural Characterization and the Study of Conformational Dynamics. *Nat. Chem.* **2014**, *6* (4), 281–294. https://doi.org/10.1038/nchem.1889.

(8) Ben-Nissan, G.; Sharon, M. The Application of Ion-Mobility Mass Spectrometry for Structure/Function Investigation of Protein Complexes. *Curr. Opin. Chem. Biol.* **2018**, *42*, 25–33. https://doi.org/10.1016/j.cbpa.2017.10.026.

(9) Gabelica, V.; Shvartsburg, A. A.; Afonso, C.; Barran, P.; Benesch, J. L. P.; Bleiholder, C.; Bowers, M. T.; Bilbao, A.; Bush, M. F.; Campbell, J. L.; Campuzano, I. D. G.; Causon, T.; Clowers, B. H.; Creaser, C. S.; De Pauw, E.; Far, J.; Fernandez-Lima, F.; Fjeldsted, J. C.; Giles, K.; Groessl, M.; Hogan, C. J.; Hann, S.; Kim, H. I.; Kurulugama, R. T.; May, J. C.; McLean, J. A.; Pagel, K.; Richardson, K.; Ridgeway, M. E.; Rosu, F.; Sobott, F.; Thalassinos, K.; Valentine, S. J.; Wyttenbach, T. Recommendations for Reporting Ion Mobility Mass Spectrometry Measurements. *Mass Spectrom. Rev.* **2019**, *38* (3), 291–320. https://doi.org/10.1002/mas.21585.

(10) Politis, A.; Park, A. Y.; Hyung, S.-J.; Barsky, D.; Ruotolo, B. T.; Robinson, C. V. Integrating Ion Mobility Mass Spectrometry with Molecular Modelling to Determine the Architecture of Multiprotein Complexes. *PLoS ONE* **2010**, *5* (8), e12080. https://doi.org/10.1371/journal.pone.0012080.

(11) Thalassinos, K.; Pandurangan, A. P.; Xu, M.; Alber, F.; Topf, M. Conformational States of Macromolecular Assemblies Explored by Integrative Structure Calculation. *Structure* **2013**, *21* (9), 1500–1508. https://doi.org/10.1016/j.str.2013.08.006.
(12) Eschweiler, J. D.; Frank, A. T.; Ruotolo, B. T. Coming to Grips with Ambiguity: Ion Mobility-Mass Spectrometry for Protein Quaternary Structure Assignment. *J. Am. Soc. Mass Spectrom.* **2017**, *28* (10), 1991–2000. https://doi.org/10.1007/s13361-017-1757-1.
(13) Uetrecht, C.; Versluis, C.; Watts, N. R.; Wingfield, P. T.; Steven, A. C.; Heck, A. J. R. Stability and Shape of Hepatitis B Virus Capsids In Vacuo. *Angew. Chem. Int. Ed.* **2008**, *47* (33), 6247–6251. https://doi.org/10.1002/anie.200802410.
(14) Marcoux, J.; Politis, A.; Rinehart, D.; Marshall, D. P.; Wallace, M. I.; Tamm, L. K.; Robinson, C. V. Mass Spectrometry Defines the C-Terminal Dimerization Domain and Enables Modeling of the Structure of Full-Length OmpA. *Structure* **2014**, *22* (5), 781–790. https://doi.org/10.1016/j.str.2014.03.004.
(15) Pacholarz, K. J.; Burnley, R. J.; Jowitt, T. A.; Ordsmith, V.; Pisco, J. P.; Porrini, M.; Larrouy-Maumus, G.; Garlish, R. A.; Taylor, R. J.; de Carvalho, L. P. S.; Barran, P. E. Hybrid Mass Spectrometry Approaches to Determine How L-Histidine Feedback Regulates the Enzyzme MtATP-Phosphoribosyltransferase. *Structure* **2017**, *25* (5), 730-738.e4. https://doi.org/10.1016/j.str.2017.03.005.
(16) Lai, A. L.; Clerico, E. M.; Blackburn, M. E.; Patel, N. A.; Robinson, C. V.; Borbat, P. P.; Freed, J. H.; Gierasch, L. M. Key Features of an Hsp70 Chaperone Allosteric Landscape Revealed by Ion-Mobility Native Mass Spectrometry and Double Electron-Electron Resonance. *J. Biol. Chem.* **2017**, *292* (21), 8773–8785. https://doi.org/10.1074/jbc.M116.770404.
(17) Smith, D. P.; Giles, K.; Bateman, R. H.; Radford, S. E.; Ashcroft, A. E. Monitoring Copopulated Conformational States during Protein Folding Events Using Electrospray Ionization-Ion Mobility Spectrometry-Mass Spectrometry. *J. Am. Soc. Mass Spectrom.* **2007**, *18* (12), 2180–2190. https://doi.org/10.1016/j.jasms.2007.09.017.
(18) Dupuis, N. F.; Wu, C.; Shea, J.-E.; Bowers, M. T. Human Islet Amyloid Polypeptide Monomers Form Ordered β-Hairpins: A Possible Direct Amyloidogenic Precursor. *J. Am. Chem. Soc.* **2009**, *131* (51), 18283–18292. https://doi.org/10.1021/ja903814q.
(19) Österlund, N.; Moons, R.; Ilag, L. L.; Sobott, F.; Gräslund, A. Native Ion Mobility-Mass Spectrometry Reveals the Formation of β-Barrel Shaped Amyloid-β Hexamers in a Membrane-Mimicking Environment. *J. Am. Chem. Soc.* **2019**, *141* (26), 10440–10450. https://doi.org/10.1021/jacs.9b04596.
(20) Giles, K.; Ujma, J.; Wildgoose, J.; Pringle, S.; Richardson, K.; Langridge, D.; Green, M. A Cyclic Ion Mobility-Mass Spectrometry System. *Anal. Chem.* **2019**, *91* (13), 8564–8573. https://doi.org/10.1021/acs.analchem.9b01838.
(21) Deng, L.; Webb, I. K.; Garimella, S. V. B.; Hamid, A. M.; Zheng, X.; Norheim, R. V.; Prost, S. A.; Anderson, G. A.; Sandoval, J. A.; Baker, E. S.; Ibrahim, Y. M.; Smith, R. D. Serpentine Ultralong Path with Extended Routing (SUPER) High Resolution Traveling Wave Ion Mobility-MS Using Structures for Lossless Ion Manipulations. *Anal. Chem.* **2017**, *89* (8), 4628–4634. https://doi.org/10.1021/acs.analchem.7b00185.
(22) Wojcik, R.; Nagy, G.; Attah, Isaac. K.; Webb, I. K.; Garimella, S. V. B.; Weitz, K. K.; Hollerbach, A.; Monroe, M. E.; Ligare, M. R.; Nielson, F. F.; Norheim, R. V.; Renslow, R. S.; Metz, T. O.; Ibrahim, Y. M.; Smith, R. D. SLIM Ultrahigh Resolution Ion Mobility Spectrometry Separations of Isotopologues and Isotopomers Reveal Mobility Shifts Due to

Mass Distribution Changes. *Anal. Chem.* **2019**, *91* (18), 11952–11962. https://doi.org/10.1021/acs.analchem.9b02808.
(23) Koeniger, S. L.; Merenbloom, S. I.; Valentine, S. J.; Jarrold, M. F.; Udseth, H. R.; Smith, R. D.; Clemmer, D. E. An IMS−IMS Analogue of MS−MS. *Anal. Chem.* **2006**, *78* (12), 4161–4174. https://doi.org/10.1021/ac051060w.
(24) Li, H.; Bendiak, B.; Siems, W. F.; Gang, D. R.; Hill, H. H. Carbohydrate Structure Characterization by Tandem Ion Mobility Mass Spectrometry (IMMS) ^{2}. *Anal. Chem.* **2013**, *85* (5), 2760–2769. https://doi.org/10.1021/ac303273z.
(25) Liu, F. C.; Ridgeway, M. E.; Park, M. A.; Bleiholder, C. Tandem Trapped Ion Mobility Spectrometry. *The Analyst* **2018**, *143* (10), 2249–2258. https://doi.org/10.1039/C7AN02054F.
(26) Eaton, R. M.; Zercher, B.; Wageman, A.; Bush, M. F. A Flexible, Modular Platform for Multidimensional Ion Mobility of Native-like Ions.
(27) Benesch, J. L.; Ruotolo, B. T. Mass Spectrometry: Come of Age for Structural and Dynamical Biology. *Curr. Opin. Struct. Biol.* **2011**, *21* (5), 641–649. https://doi.org/10.1016/j.sbi.2011.08.002.
(28) Wyttenbach, T.; Bowers, M. T. Structural Stability from Solution to the Gas Phase: Native Solution Structure of Ubiquitin Survives Analysis in a Solvent-Free Ion Mobility–Mass Spectrometry Environment. *J. Phys. Chem. B* **2011**, *115* (42), 12266–12275. https://doi.org/10.1021/jp206867a.
(29) Myung, S.; Badman, E. R.; Lee, Y. J.; Clemmer, D. E. Structural Transitions of Electrosprayed Ubiquitin Ions Stored in an Ion Trap over ∼10 Ms to 30 s †. *J. Phys. Chem. A* **2002**, *106* (42), 9976–9982. https://doi.org/10.1021/jp0206368.
(30) Badman, E. R.; Hoaglund-Hyzer, C. S.; Clemmer, D. E. Monitoring Structural Changes of Proteins in an Ion Trap over ∼10−200 Ms: Unfolding Transitions in Cytochrome *c* Ions. *Anal. Chem.* **2001**, *73* (24), 6000–6007. https://doi.org/10.1021/ac010744a.
(31) Mao, Y.; Woenckhaus, J.; Kolafa, J.; Ratner, M. A.; Jarrold, M. F. Thermal Unfolding of Unsolvated Cytochrome c: Experiment and Molecular Dynamics Simulations. *J. Am. Chem. Soc.* **1999**, *121* (12), 2712–2721. https://doi.org/10.1021/ja980324b.
(32) Z. Steinberg, M.; Breuker, K.; Elber, R.; Benny Gerber, R. The Dynamics of Water Evaporation from Partially Solvated Cytochrome c in the Gas Phase. *Phys. Chem. Chem. Phys.* **2007**, *9* (33), 4690–4697. https://doi.org/10.1039/B705905A.
(33) Pacholarz, K. J.; Porrini, M.; Garlish, R. A.; Burnley, R. J.; Taylor, R. J.; Henry, A. J.; Barran, P. E. Dynamics of Intact Immunoglobulin G Explored by Drift-Tube Ion-Mobility Mass Spectrometry and Molecular Modeling. *Angew. Chem. Int. Ed.* **2014**, *53* (30), 7765–7769. https://doi.org/10.1002/anie.201402863.
(34) Oh, H.; Breuker, K.; Sze, S. K.; Ge, Y.; Carpenter, B. K.; McLafferty, F. W. Secondary and Tertiary Structures of Gaseous Protein Ions Characterized by Electron Capture Dissociation Mass Spectrometry and Photofragment Spectroscopy. *Proc. Natl. Acad. Sci.* **2002**, *99* (25), 15863–15868. https://doi.org/10.1073/pnas.212643599.
(35) Mihalca, R.; Kleinnijenhuis, A. J.; McDonnell, L. A.; Heck, A. J. R.; Heeren, R. M. A. Electron Capture Dissociation at Low Temperatures Reveals Selective Dissociations. *J. Am. Soc. Mass Spectrom.* **2004**, *15* (12), 1869–1873. https://doi.org/10.1021/jasms.8b02108.

(36) McLafferty, F. W.; Guan, Z.; Haupts, U.; Wood, T. D.; Kelleher, N. L. Gaseous Conformational Structures of Cytochrome c. *J. Am. Chem. Soc.* **1998**, *120* (19), 4732–4740. https://doi.org/10.1021/ja9728076.
(37) Breuker, K.; McLafferty, F. W. Stepwise Evolution of Protein Native Structure with Electrospray into the Gas Phase, 10−12 to 102 s. *Proc. Natl. Acad. Sci.* **2008**, *105* (47), 18145–18152. https://doi.org/10.1073/pnas.0807005105.
(38) Davidson, K. L.; Oberreit, D. R.; Hogan, C. J.; Bush, M. F. Nonspecific Aggregation in Native Electrokinetic Nanoelectrospray Ionization. *Int. J. Mass Spectrom.* **2017**, *420*, 35–42. https://doi.org/10.1016/j.ijms.2016.09.013.
(39) Allen, S. J.; Eaton, R. M.; Bush, M. F. Analysis of Native-Like Ions Using Structures for Lossless Ion Manipulations. *Anal. Chem.* **2016**, *88* (18), 9118–9126. https://doi.org/10.1021/acs.analchem.6b02089.
(40) Allen, S. J.; Eaton, R. M.; Bush, M. F. Structural Dynamics of Native-Like Ions in the Gas Phase: Results from Tandem Ion Mobility of Cytochrome *c*. *Anal. Chem.* **2017**, *89* (14), 7527–7534. https://doi.org/10.1021/acs.analchem.7b01234.
(41) Eaton, R. M.; Allen, S. J.; Bush, M. F. Principles of Ion Selection, Alignment, and Focusing in Tandem Ion Mobility Implemented Using Structures for Lossless Ion Manipulations (SLIM). *J. Am. Soc. Mass Spectrom.* **2019**, *30* (6), 1115–1125. https://doi.org/10.1007/s13361-019-02170-1.
(42) Allen, S. J.; Giles, K.; Gilbert, T.; Bush, M. F. Ion Mobility Mass Spectrometry of Peptide, Protein, and Protein Complex Ions Using a Radio-Frequency Confining Drift Cell. *Analyst* **2016**, *141* (3), 884–891. https://doi.org/10.1039/C5AN02107C.
(43) Hong, S.; Bush, M. F. Collision-Induced Unfolding Is Sensitive to the Polarity of Proteins and Protein Complexes. *J. Am. Soc. Mass Spectrom.* **2019**, *30* (11), 2430–2437. https://doi.org/10.1007/s13361-019-02326-z.
(44) Allen, S. J.; Bush, M. F. Radio-Frequency (RF) Confinement in Ion Mobility Mass Spectrometry: Apparent Mobilities and Effective Temperatures. *J. Am. Soc. Mass Spectrom.* **2016**, *27*, 2054–2063. https://doi.org/10.1007/s13361-016-1479-9.
(45) Bush, M. F.; Hall, Z.; Giles, K.; Hoyes, J.; Robinson, C. V.; Ruotolo, B. T. Collision Cross Sections of Proteins and Their Complexes: A Calibration Framework and Database Collision Induced Unfoldingfor Gas-Phase Structural Biology. *Anal. Chem.* **2010**, *82* (22), 9557–9565. https://doi.org/10.1021/ac1022953.
(46) Freeke, J.; Bush, M. F.; Robinson, C. V.; Ruotolo, B. T. Gas-Phase Protein Assemblies: Unfolding Landscapes and Preserving Native-like Structures Using Noncovalent Adducts. *Chem. Phys. Lett.* **2012**, *524*, 1–9. https://doi.org/10.1016/j.cplett.2011.11.014.
(47) Dixit, S. M.; Polasky, D. A.; Ruotolo, B. T. Collision Induced Unfolding of Isolated Proteins in the Gas Phase: Past, Present, and Future. *Curr. Opin. Chem. Biol.* **2018**, *42*, 93–100. https://doi.org/10.1016/j.cbpa.2017.11.010.
(48) Pierson, N. A.; Valentine, S. J.; Clemmer, D. E. Evidence for a Quasi-Equilibrium Distribution of States for Bradykinin [M + 3H]3+ Ions in the Gas Phase. *J. Phys. Chem. B* **2010**, *114* (23), 7777–7783. https://doi.org/10.1021/jp102478k.
(49) Eldrid, C.; Ujma, J.; Kalfas, S.; Tomczyk, N.; Giles, K.; Morris, M.; Thalassinos, K. Gas Phase Stability of Protein Ions in a Cyclic Ion Mobility Spectrometry Traveling Wave Device. *Anal. Chem.* **2019**, *91* (12), 7554–7561. https://doi.org/10.1021/acs.analchem.8b05641.

(50) Devine, P. W. A.; Fisher, H. C.; Calabrese, A. N.; Whelan, F.; Higazi, D. R.; Potts, J. R.; Lowe, D. C.; Radford, S. E.; Ashcroft, A. E. Investigating the Structural Compaction of Biomolecules Upon Transition to the Gas-Phase Using ESI-TWIMS-MS. *J. Am. Soc. Mass Spectrom.* **2017**, *28* (9), 1855–1862. https://doi.org/10.1007/s13361-017-1689-9.
(51) Hernandez-Alba, O.; Wagner-Rousset, E.; Beck, A.; Cianférani, S. Native Mass Spectrometry, Ion Mobility, and Collision-Induced Unfolding for Conformational Characterization of IgG4 Monoclonal Antibodies. *Anal. Chem.* **2018**, *90* (15), 8865–8872. https://doi.org/10.1021/acs.analchem.8b00912.
(52) Hansen, K.; Lau, A. M.; Giles, K.; McDonnell, J. M.; Struwe, W. B.; Sutton, B. J.; Politis, A. A Mass-Spectrometry-Based Modelling Workflow for Accurate Prediction of IgG Antibody Conformations in the Gas Phase. *Angew. Chem. Int. Ed.* **2018**, *57* (52), 17194–17199. https://doi.org/10.1002/anie.201812018.
(53) Tian, Y.; Han, L.; Buckner, A. C.; Ruotolo, B. T. Collision Induced Unfolding of Intact Antibodies: Rapid Characterization of Disulfide Bonding Patterns, Glycosylation, and Structures. *Anal. Chem.* **2015**, *87* (22), 11509–11515. https://doi.org/10.1021/acs.analchem.5b03291.

Chapter 3: Towards IM^n with Electrostatic Drift Fields: Resetting the Potential of Trapped Ions Between Dimensions of Tandem Ion Mobility Separations

3.1 Abstract

Multidimensional experiments offer the opportunity to increase the information content and thus the selectivity of ion mobility (IM) separations. However, these experiments have been difficult to realize on instruments that use constant electrostatic gradients to separate ions. Here, we report a novel strategy to manipulate the ion potential using a modular, electrostatic IM instrument. In this approach, the potentials of trapped ions are "reset" between dimensions of IM. In potential-resetting experiments, mobility-selected ions were trapped between dimensions of IM; the potentials of the trapping region were then raised by 182 V in approximately 5 ms using an incremental voltage ramp. Trapped ions are then separated in the second dimension of IM (which was held at ground potential prior to potential resetting) to generate an arrival-time distribution. Arrival-time distributions were compared to similar experiments where ion potential was not reset, which indicated that ions were neither lost nor activated during potential-resetting. Ion trajectory simulations were also used to model potential resetting; ions underwent minimal realignment and no changes in effective temperatures were observed. Finally, we demonstrate that IM information can be preserved during potential resetting by selecting conformations of a broad 9+ cytochrome *c* distribution, resetting their potential, and performing a second-dimension IM separation that shows the retention of conformers. We anticipate that this strategy will be useful in enabling flexible, multidimensional experiments on electrostatic IM instruments.

3.2 Introduction

Ion mobility mass spectrometry (IM-MS) is an analytical technique that separates ions in a neutral drift gas under the influence of a weak electric field prior to mass analysis, providing size and shape information orthogonal to the mass to charge (m/z) readout of mass analysis. Recent technological innovations have increased the scope and quality of IM-MS separations, leading to its expanded adoption.[1,2] Instrumental innovations have targeted high-resolution separations to differentiate closely related biomolecules,[3–6] as well as increased throughput and sensitivity.[7–9] More recently, new instrumental platforms have utilized unique geometries and ion manipulation techniques to push the boundaries of traditional IM experiments. Two pertinent examples are the Structures for Lossless Ion Manipulations (SLIM) architecture and the recently introduced Cyclic IMS system. The SLIM architecture has seen recent application in ultrahigh-resolution IM-MS, utilizing long serpentine separation paths to separate ions.[10] The cyclic IMS system also expands the experimental flexibility of IM-MS, employing an off-axis cyclic separator that can subject ions to both multipass and multidimensional separations.[11]

Next-generation IM separations on these instruments are performed using traveling wave (TW) separations, where ion motion is driven by a series of dynamic and transient potentials, as opposed to the electrostatic gradients used in drift tube (DT) IM.[12] Since its introduction in 2006,[13] TWIM has seen more widespread adoption as it enables flexible control of ion motion at low applied voltages relative to DT instruments.[14] Although TWIM offers several advantages, it is difficult to determine mobility directly from experimental observables without calibration due to the complex nature of the dynamic fields used for ion separation.[15] Calibration efforts also become more difficult as multidimensional experiments become more complex. Electrostatic gradients in IM separations allow for the direct measurement of mobility, which can then be

converted to collision cross section (Ω). Previously, electrostatic gradients were used in pioneering multidimensional IM experiments by interfacing two stacked ring drift tubes with a mobility-selective ion funnel.[16] At a constant electric field, the voltage range increases linearly with the length of the separation region, which can result in significant engineering challenges.[4] Furthermore, the linear geometry of traditional stacked-ring drift tubes requires large instrument footprints when implemented sequentially.[17] There remains a need for instrumentation that can enable flexible, multidimensional experiments and the direct measurement of Ω values.

The flexibility of multidimensional experiments on electrostatic IM instruments is hindered by the need for monotonically decreasing voltages across the separation region. A possible alternative is to apply electrostatic gradients only when ions are being separated within a given region. The dynamic application of monotonic DC gradients has previously been used in a mobility filtering approach referred to as overtone mobility spectrometry.[18] In that approach, only ions that are resonant with the field switching frequency are transmitted through the separation region. That innovative approach does not address the difficulties in enabling multidimensional IM experiments on electrostatic IM systems. Multidimensional experiments are enabled by the ability to select ions of interest for further dimensions of separation. In some experiments, ions are briefly trapped between dimensions of IM. This trapping between dimensions of IM offers an opportunity to manipulate the potential of ions as a monotonic DC gradient is applied to the separation region downstream of the trapped ions. In this way, ions can traverse drift regions in which drift fields were not previously applied.

In this work, we manipulate the voltage of trapped ions to reset the potential of native-like protein ions on a modular IM instrument. We have demonstrated ion trapping capabilities in tandem IM separations on this modular IM instrument.[19,20] This modular instrument uses the

SLIM architecture. Most recent implementations of SLIM in the literature use TW, but this instrument uses electrostatic gradients to separate ions. Ion trapping on the SLIM platform is well documented, enabling ion storage with minimal ion loss and activation.[21,22] We then reset the potential of mobility-selected protein ions and compared the arrival-time distributions, mass spectra, and integrated intensity from multidimensional measurements where the potential of trapped ions was not reset. To demonstrate the use of potential resetting in multidimensional IM analysis of conformers, we mobility-selected subpopulations of protein ions, reset their potential, and monitored differences in mobility in using a second dimension of IM. We also performed complementary SIMION simulations to understand the extent of ion activation and retention during potential resetting. These separations and simulations provide evidence that raising the potential of ions trapped between SLIM modules is feasible, providing a key tool in enabling future multidimensional separations.

3.3 Methods

3.3.1 Sample Preparation and Ionization. Ubiquitin, concanavalin A, and cytochrome *c* were purchased from Sigma-Aldrich. Electrokinetic nanoelectrospray ionization[23] was used to generate native-like protein ions from 10 to 20 μM protein in aqueous 200 mM ammonium acetate adjusted to pH 7.0. Denatured cytochrome *c* samples were prepared by buffer exchanging 20 μM cytochrome *c* in 200 mM ammonium acetate using Micro Bio-Spin 6 columns (Bio-Rad, Hercules, CA) that had been equilibrated with three washes of 0.1% acetic acid.

3.3.2 Instrumentation. We recently reported a 12-module array capable of tandem IM experiments.[24] This instrument utilizes the structures for lossless ion manipulations (SLIM) architecture in which pairs of printed circuit boards form modules that create the potential

landscape for IM separation.[25,26] Briefly, ions are transported through a stainless-steel capillary to two ion funnels. Ions then reach the 12-module array where they undergo IM separation in nitrogen at pressures near 4 Torr. This implementation of the SLIM architecture uses electrostatic gradients to separate ions; no traveling waves are used in the separation. Separated ions then enter a circular ion funnel that interfaces with the mass analyzer. Voltages for the 12-module array are controlled using custom-built power supplies (GAA Custom Electronics, Kennewick, WA). User programmed voltage ramps controlled the potential of different regions of the modular array in these experiments.

3.3.3 Tandem IM Separations and Resetting the Potential of Trapped Ions. A top-down view of the 12-module array is shown in Figure 3.1A. Time-dependent voltage control within the modular array enables ion packet preparation, ion mobility separation, ion selection, and ion trapping.[24,19] Figure 3.1A illustrates the separation regions that comprise tandem IM experiments. Ion packets are generated on the first module (^{1}M) and are released for separation in the first dimension of IM (^{1}D). Mobility separated ions – e.g., a specific charge state of a native-like protein – are then selected and diverted at the ^{7}M for further analysis, whereas all other ions continue down the collinear path of the ^{7}M to a collection electrode. Selected ions are trapped for a short time (~10 ms) at the interface between the ^{7}M and the ^{8}M. Ion trapping is performed at the interface of modules by biasing the input voltage of one module relative to the output voltage of the preceding module, creating a potential well referred to as a junction trap. Trapped ions are then released for separation in the second dimension of IM (^{2}D).

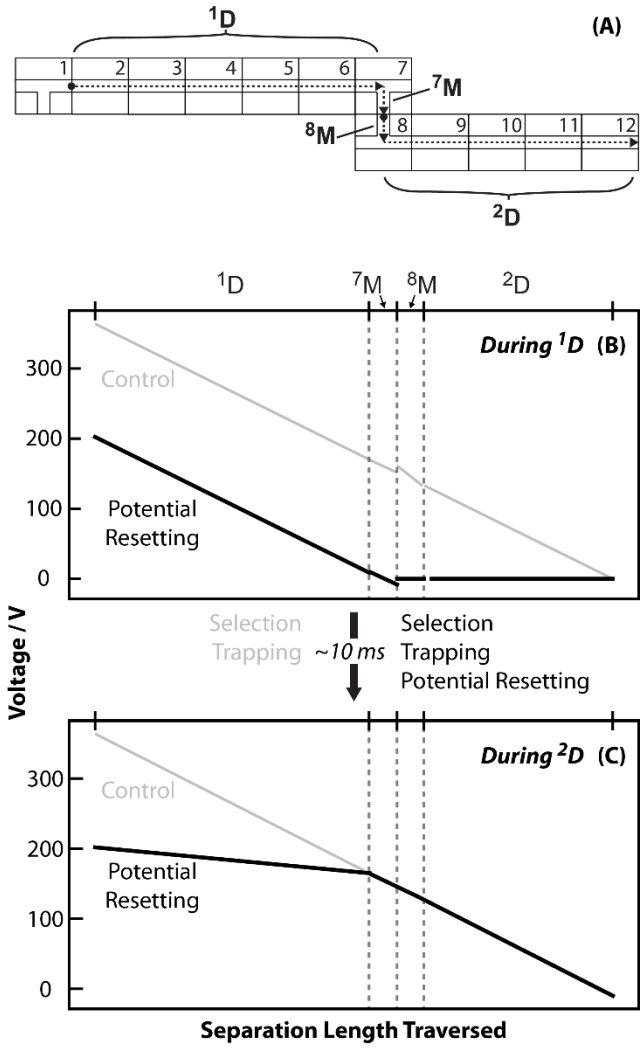

Figure 3.1. (A) A top-down view of the array of 12 SLIM modules. Module 1 (^{1}M), ^{7}M, and ^{8}M are tee modules, while $^{2\text{-}6}$M and $^{9\text{-}12}$M are straight modules. Dotted arrows represent the separation regions of the 12-module array involved in these experiments. ^{1}D and ^{2}D correspond to the first and second dimension of ion mobility separation, respectively. ^{7}M and ^{8}M represent the orthogonal paths of those modules which are used to create the junction trap that confines ions between dimensions. Voltage diagrams depict the potentials applied to these regions during in tandem IM separations during the ^{1}D separation (B) and the ^{2}D separation (C) for control (grey trace) and potential raising (black trace) separations.

In previous demonstrations of tandem IM on this instrument, drift regions are held at voltage throughout the entirety of the separation, i.e., the absolute potentials of the electrodes the comprise the drift regions continuously decrease across the separation length. Such an experiment is referred to as the control and is illustrated by the grey trace in the voltage diagrams in Figure 3.1B and 3.1C. The absolute voltages that define the ^{1}D are set to accommodate the constant application of a drift field in the ^{2}D. An alternative approach is illustrated by the black trace in Figures 1B and 1C. In these potential-resetting experiments, the ^{2}D region is held at ground while ions are separated in the ^{1}D (Figure 3.1B). After ions are selected and trapped at the ^{7}M/^{8}M junction trap, voltages of the ^{7}M, ^{8}M, and ^{2}D regions are all raised to establish a drift field in the ^{2}D. After resetting the potential, ions can be released into the newly established ^{2}D drift field for separation (Figure 3.1C).

We performed tandem IM experiments using both approaches to understand the effects of potential resetting in tandem IM experiments. In both experiments, the drift fields of the ^{1}D, ^{7}M, ^{8}M, and ^{2}D were 4 V cm^{-1}, 3.75 V cm^{-1}, 3.75 V cm^{-1}, and 5 V cm^{-1}, respectively. In both experiments, selected ions were allowed to traverse the ^{7}M and thermalize in the junction trap for 10 ms. The junction trap was created by biasing the input of ^{8}M by 10 V. In potential-resetting experiments, the voltages of the ^{7}M, ^{8}M, and ^{2}D were raised during ion trapping using programmed voltage ramps that incremented the voltage by 5 V every 125 μs. The voltage ramps raised the potential of the ions by 147 V over the course of 4.75 ms. After an additional 10 ms delay, ions were released into the ^{2}D. Although potentials were not reset using voltage ramps in

control experiments, the ions were trapped for the same amount of time as potential-resetting experiments to ensure ions had the same gas-phase lifetime in both experiments.

3.3.4 Ion Trajectory Simulations. Trajectories were modeled in SIMION (Scientific Instrument Services, Ringoes, NJ). 5+ ubiquitin and 15+ concanavalin A dimer trajectories were simulated using the hard-spheres collision model, which explicitly models each collision using neutral gas velocities sampled from a Boltzmann distribution and mean free path values calculated from ion collision cross sections.[27] Relative ion-gas velocities and a previously reported statistical approach[28] were used to estimate the effective temperatures of these ions in the trap in control and potential resetting experiments.

3.4 Results and Discussion

To enable flexible IM experiments on instruments that use electrostatic gradients to separate ions, we sought to raise the potential of trapped ions between dimensions of tandem IM. We will refer to this strategy as "potential-resetting". This strategy lowers the absolute voltages required for multidimensional separations, as ions can be separated in dimensions of IM that were previously held at ground during preceding dimensions of IM. Ion trapping using the SLIM architecture has been reported in SLIM development[21] and subsequently used in tandem IM separations in our lab,[19,20,22] but raising the potential of ions in the trap in this manner has not been demonstrated.

The voltage diagrams in Figure 3.1B and 3.1C illustrate two approaches for tandem IM separations. The grey trace depicts a standard tandem IM separation, referred to as the control experiment, where the ^{1}D and ^{2}D are held at constant drift fields for the entirety of the experiment; only voltages in the selection and trapping regions of the ^{7}M and the ^{8}M are

modulated during the experiment. These experiments are compared to potential-resetting experiments, which are depicted in the black trace in Figures 1B and 1C. In the potential-resetting experiments, the ^{2}D is initially held at ground as ions are separated in the ^{1}D, which allows for the ^{1}D drift field to be established using lower absolute potentials relative to ground. After the ^{1}D, ions are mobility selected and trapped between ^{7}M and ^{8}M as in control experiments; programmed voltage ramps are used to raise voltages in the junction trap voltages and on the electrodes used for the ^{2}D.

Scheme 1 illustrates possible scenarios when resetting the potential of trapped ions. An ideal case is shown in Scheme 1A. Ideally, ions are neither activated nor lost through this process. This scenario may be achieved when ions held within a junction trap remain unperturbed as the voltages that comprise the junction trap are raised in unison, i.e., there is no change in potentials in the ion's frame of reference. This scenario may also occur if any changes are small and slow relative to rethermalization of the ions through collisions with the gas. Possible limitations of the potential-resetting strategy are illustrated in Scheme 1B and 1C. Scheme 1B illustrates possible equilibrium effects caused by changing the potential profile of the junction trap in response to the application of downstream drift fields. At the beginning of the experiment, the junction trap is formed by biasing the ^{8}M by 10 V; at this point, there is no drift field applied in the ^{8}M. After potential resetting, the ^{8}M has an applied drift field of 3.75 V cm^{-1}. Should the application of this downstream drift field affect the shape of the potential well in the junction trap, ions that had thermalized in the junction trap at the beginning of the experiment may now experience a different potential environment. For example, the new junction trap profile may increase ion confinement, resulting in increased coulombic repulsion that could push ions toward confining RF voltages, resulting in activation. Beyond equilibrium effects, Scheme

1C illustrates possible dynamic effects of implementing this strategy on a high impedance RC circuit. The voltage divider networks used to create stepwise voltage profiles on our SLIM instrument are manipulated by simultaneously incrementing respective input and output voltages. Lag in the response time of the central electrodes in the circuit would cause non-linear drift fields, distorting potentials in the ion's frame of reference. Such distortion could result in inadequate ion confinement and subsequent ion loss or in ion activation.

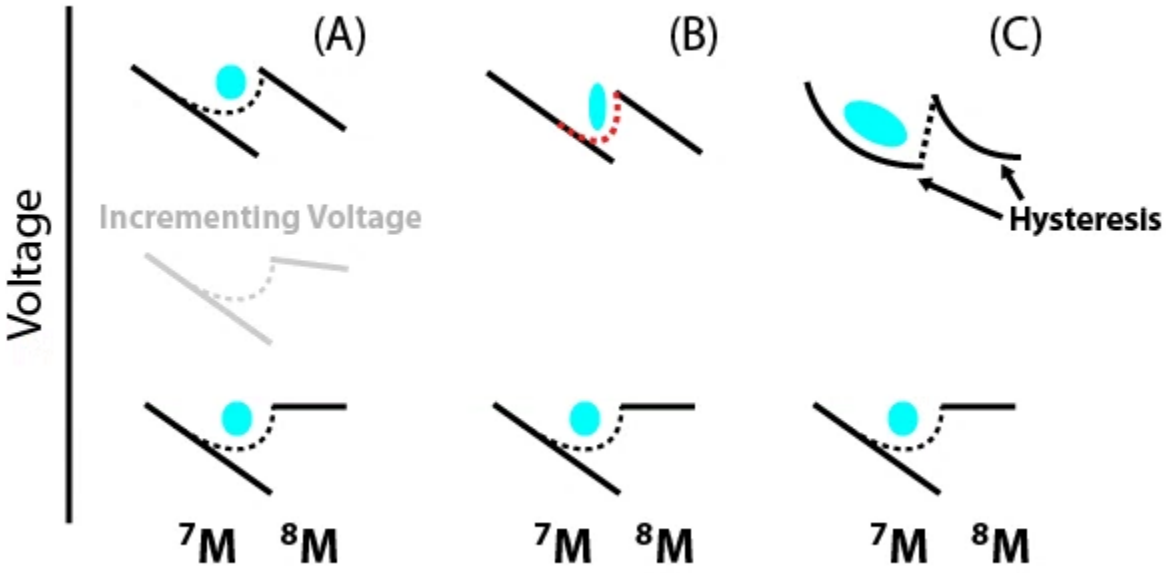

Scheme 3.1. Illustrative voltage diagrams of potential scenarios in PR experiments; diagrams are not drawn to scale. Solid lines represent DC potentials applied to the labeled separation region of the module, while the dotted lines at the interface represent the potential well formed by biasing the input of ^{8}M relative to the output of ^{7}M. The cyan oval represents the ion cloud. (A) An idealized case where the potential well remains

constant in the ion's frame of reference. The effect of applying downstream drift fields (B) and possible hysteresis effects (C).

3.4.1 Resetting Ion Potential. We sought to demonstrate potential resetting on our modular IM instrument by comparing potential-resetting experiments to control experiments. Single charge states were isolated after the ^{1}D by performing mobility-dependent ion selection at the ^{7}M.[19] Ions were then either trapped at a constant absolute potential (control experiment) or trapped at a potential near earth ground prior to raising the junction trap potentials by 182 V (potential-resetting experiment). Ions were then released into the ^{2}D and their arrival-time distributions (ATD) were measured. Figure 3.2 shows a comparison of the ^{2}D ATDs and mass spectra generated in both control and potential-resetting experiments for 5+ ubiquitin (Figure 3.2A and 3.2B) and 15+ concanavalin A (Figure 3.2D and 3.2E). For both 5+ ubiquitin and 15+ concanavalin A, we observed nearly indistinguishable ^{2}D ATDs and mass spectra between the control and potential-resetting experiments. The ATDs and mass spectra were taken in triplicate and averaged; intensities are not normalized.

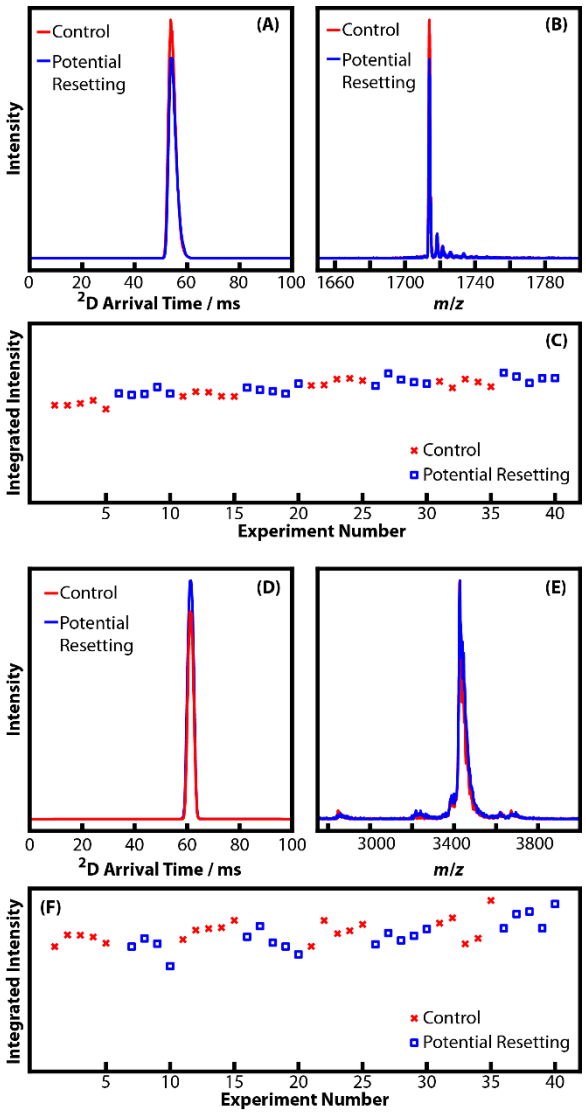

Figure 3.2. ^{2}D arrival-time distributions (A) and mass spectra (B) in control and potential resetting experiments for 5+ ubiquitin. Integrated intensities of 5+ ubiquitin in replicates for both experiments (C). ^{2}D arrival-time distributions (D) and mass spectra (E) of 15+ concanavalin A in control and potential resetting experiments, respectively. Integrated intensities of replicates of both experiment types (F).

We performed these experiments to evaluate the feasibility of potential resetting in tandem IM experiments. First, if potential resetting were to result in significant ion activation,

we would expect the native-like protein ions probed in these experiments to undergo gas-phase unfolding toward their extended equilibrium structures, which would shift the ^{2}D ATD shifting to longer arrival times. The well overlaid ^{2}D ATDs observed in these experiments indicate that potential resetting does not induce activation that corresponds to observable differences in mobilities of ion populations in the two experiments. Furthermore, both ATDs appear at very similar drift times, indicating that ions are released from similar locations within the junction trap. Additionally, if potential resetting were to introduce an *m*/*z* bias where either lower or higher mass ions are preferentially retained within the junction trap through the potential-resetting process, we would observe this in the mass spectra; once again, the mass spectra from both experiments are in good agreement, indicating that potential resetting does not introduce an *m*/*z* bias.

Although well overlaid, the ATDs and mass spectra in Figure 3.2 do exhibit slightly different intensities between the two experiments. To gain a better understanding of ion utilization and retention in potential-resetting experiments, we performed twenty replicates of each experimental mode, switching between control and potential-resetting experiments every five replicates. The integrated intensities of the ATDs from these measurements of 5+ ubiquitin and 15+ concanavalin A are shown in Figures 2C and 2F, respectively. To collect this data, a single electrospray emitter was loaded with protein solution and voltages were applied to achieve an electrospray current near 20 nanoamps. Five replicates were taken in one experimental mode before stopping electrospray to adjust instrument voltages. A voltage was then applied to the emitter to achieve the same electrospray current and five replicates were taken in the other experimental mode. This process was repeated until 20 replicates were taken in each experimental mode. For both analytes, ion intensities appear to be independent of two

experimental modes. There are small differences in the intensities across the range of experiment numbers, which we attribute to small drifts in the ion source. Importantly, these data indicate that potential resetting does not result in significant ion loss.

3.4.2 Ion Trajectory Simulations. The preceding experiments provide evidence that the potential-resetting strategy does not perturb ions in such a way that is observable in a ^{2}D separation. Nevertheless, ions may still undergo positional shifts within the junction trap should the shape of the potential well change as the ^{8}M drift field is applied. To better understand the positions of ions in the junction trap before and after potential resetting, ion trajectories were simulated using SIMION 8.1. We modeled potential arrays using instrumental and electrode geometries and programmed potential ramps to mimic the incremental voltage increase used in potential-resetting separations. Ions were initiated 6.50 mm upstream of a 10 V junction trap formed at the interface of two modules. Ions drifted into the junction trap in a drift field of 4 V cm^{-1}, while no drift field was applied beyond the interface of the junction trap at the beginning of the simulation. Ions reached the junction trap and were held for approximately 5 ms prior to raising the potentials of the junction trap by 5 V every 125 μs. Voltages were raised a total of 182 V over 4.75 ms to replicate potential-resetting experiments. Ions were held in the junction trap with the new voltage profile for an additional 4.75 ms after potential resetting. Ion positions and relative ion-gas velocities were sampled prior to every collision. Ion trajectories were analyzed prior to, during, and after potential resetting. Prior to potential resetting, ion position and relative ion-gas velocities were sampled only after the ion was given ample time to thermalize within the trap so that initial drifting of ions did not affect calculated effective temperatures.

The histograms of ion position are shown in Figure 3.3 for 15+ concanvalin A, 5+ ubiquitin, and 1+ GRGDS, a small peptide that has a higher mobility relative to native-like

protein ions. The binned positional coordinate corresponds to the axis of transmission – i.e., this dimension defines proximity to the module interface where a junction trap is created. Ions reside in different areas of the potential well according to their mobility; concanavalin A, the least mobile ion, resides nearest the junction trap interface, whereas GRDGS resides furthest from the interface. Ions also sample larger areas within the junction trap during the simulation according to mobility, as GRGDS samples the largest area within the junction trap. The histograms are broken down into three segments that correspond to the time prior to, during, and after potential resetting. For each analyte, ions realign nearer the junction trap interface as a drift field is applied to the module downstream of the bias that creates the junction trap. Comparisons of the average positions during time segments prior to and after potential resetting show that GRGDS, ubiquitin, and concanavalin A are positioned 0.15 mm, 0.14 mm, and 0.13 mm closer to the module interface, respectively.

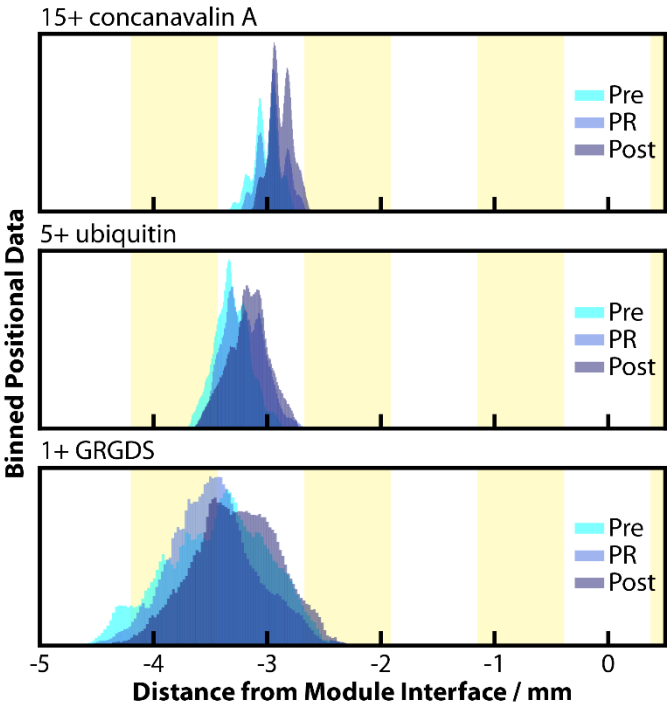

Figure 3.3. Histograms of ion positions for 1+ GRGDS (A), 5+ ubiquitin (B), and 15+ concanavalin A (C). Ion positions are binned along the axis of transmission, i.e., this dimension describes proximity to the junction trap formed at the module interface.

The realignment within the junction trap in these experiments is a concern mainly if it corresponds to a change in position that causes ions to interact more strongly with electrodynamic potentials and experience higher-energy collisions with gas molecules. To understand ion activation, relative ion-gas velocities were sampled prior to each collision and a previously reported statistical approach[28] was used to estimate the effective temperatures of ions in the junction trap. Effective temperatures for the three analytes in each portion of the simulation are shown in Table 1. The effective temperatures of trapped ions are elevated slightly relative to ambient temperature, which aligns with previous work that analyzed ions within a similar junction trap profile.[19] Ion temperature differences across the three segments of the simulation are negligible.

Analyte	T_{eff} Prior to Potential Resetting (K)	T_{eff} During Potential Resetting (K)	T_{eff} After Potential Resetting (K)
15+ conncanavalin A	310.1 ± 0.5	310.3 ± 0.2	310.2 ± 0.2
5+ ubiquitin	318.0 ± 0.5	317.8 ± 0.7	317.9 ± 0.6
1+ GRGDS	367.0 ± 3.3	362.3 ± 3.9	366.8 ± 3.3

Table 3.1. Estimated effective temperatures (T_{eff}) of trapped ions at different time points within the potential resetting simulations. Effective temperatures are averaged from five replicate trajectories. The range spans the 95% confidence interval.

These trajectory simulations probe the effect of dynamically applying a downstream drift field on ions within the junction trap. The results indicate that this process does change the profile of the junction trap as ions undergo a slight positional realignment; this realignment does not result in elevated effective temperatures of single ions within the trap. Although informative, these simulations do not capture all practical elements of junction trapping in potential-resetting experiments. For one, these simulations probe single ions, whereas potential-resetting experiments will trap larger populations of ions. It is possible that the realignment observed in these experiments coincides with a decrease in trap capacity after potential resetting. Such an effect could result in deleterious effects arising from coulombic repulsion if the junction trap is overfilled prior to potential resetting. To minimize this, the number of ions in potential-resetting experiments can be controlled by modulation of the ion beam at the [1]M. Furthermore, each electrode in these simulations is controlled directly by user programming and no attempt was

made to represent the hysteresis of the actual high-impedance, resistor-capacitor circuit. Therefore, these simulations may not capture the effects that could contribute to the scenario depicted in Scheme 1C.

3.4.3 Subpopulations of Conformations Remain Resolved After Potential Resetting. Initial experiments and ion trajectory simulations demonstrate the feasibility of resetting the potential of ions within a junction trap. We plan to leverage this strategy on our multidimensional IM instrument to increase the experimental flexibility of IM instruments that utilize electrostatic gradients. To demonstrate the utility of resetting the potential on an electrostatic instrument, we used the ion selection capabilities of our tandem instrument to select mobility-resolved subpopulations of a broader distribution, raise their potential, and measure apparent Ω in a ^{2}D IM measurement. Electrostatic gradients enable the calculation of an analyte's collision cross section (Ω) using mobility (K) values measured directly from experiment.

Denaturing conditions were used to generate the 9+ charge state of cytochrome *c*, which exhibited evidence for multiple conformations in previous IM studies.[29] Figure 3.4 shows the results from tandem IM separations of 9+ cytochrome *c*. We performed a potential-resetting experiment on the entire population of 9+ cytochrome. Then, by changing the time-dependent selection of ions at the ^{7}M, we selected subpopulations of the broader distribution of 9+ cytochrome *c* ions and reset their potential. The ^{2}D arrival-time axis was then converted to an apparent Ω axis (see *Appendix A*). The apparent Ω distributions are shown in Figure 3.4 for the different experiments and subpopulations. The distributions of selected subpopulations are well resolved in the ^{2}D separation, demonstrating that mobility-encoded information from ion selection in the ^{1}D is preserved in the ^{2}D separation even when ion potential is reset. Furthermore, the mobility of ions in potential-resetting experiments can be easily converted to

apparent Ω values without calibration, which enables inter-instrumental comparisons of the results from multidimensional IM experiments.

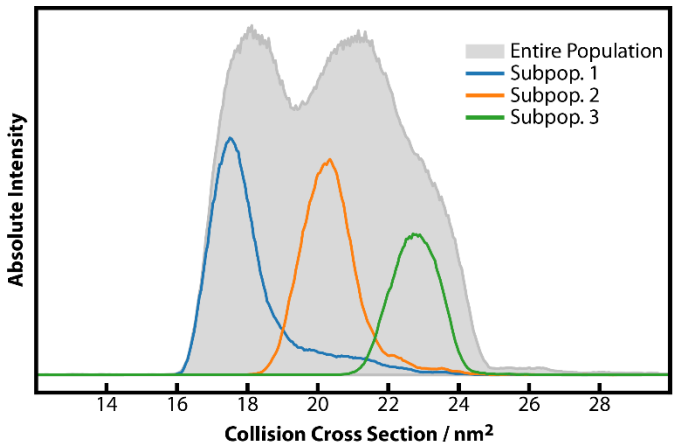

Figure 3.4. ^{2}D apparent Ω measurements of the entire population of 9+ cytochrome *c* in control and potential resetting experiments. Subpopulations were selected by modifying the selection at the ^{7}M; subpopulations had their potential reset prior to measurement in the ^{2}D.

3.5 Conclusions and Future Direction.

We have outlined a strategy to reset ion potential in IM separations on architectures that use electrostatic gradients. Using the tandem IM capabilities of our modular IM instrument, we compared tandem IM separations where drift fields were held constant through the entire experiment to experiments in which ion potential was reset as drift fields were dynamically applied to regions previously held at ground. The results from these experiments indicate that potential resetting does not activate ions, nor are ions lost during potential-resetting experiments. Rather, ion intensities are consistent between the two experiments, as are the ^{2}D arrival-time distributions and mass spectra. Simulation data supported these conclusions, as ions underwent a small realignment in the junction trap after potential resetting that did not result in differences in

ion activation. Lastly, potential-resetting experiments were performed on subpopulations of a distribution of 9+ cytochrome *c* ions. Selected ions were separated in the ^{2}D, demonstrating that mobility information from the ^{1}D was preserved after potential resetting. ^{2}D drift times were then converted into collision cross sections without calibration, demonstrating the utility of multidimensional experiments on electrostatic IM instruments. We believe the potential-resetting strategy presented here will be of great utility in the pursuit of next-generation IM experiments that use electrostatic gradients for separation.

3.6 Acknowledgments. Research reported in this publication was supported by the National Institute of General Medical Sciences of the National Institutes of Health through award number R01GM130708.

References

(1) May, J. C.; McLean, J. A. Ion Mobility-Mass Spectrometry: Time-Dispersive Instrumentation. *Anal. Chem.* **2015**, *87* (3), 1422–1436. https://doi.org/10.1021/ac504720m.

(2) Lanucara, F.; Holman, S. W.; Gray, C. J.; Eyers, C. E. The Power of Ion Mobility-Mass Spectrometry for Structural Characterization and the Study of Conformational Dynamics. *Nat. Chem.* **2014**, *6* (4), 281–294. https://doi.org/10.1038/nchem.1889.

(3) Baker, E. S.; Clowers, B. H.; Li, F.; Tang, K.; Tolmachev, A. V.; Prior, D. C.; Belov, M. E.; Smith, R. D. Ion Mobility Spectrometry—Mass Spectrometry Performance Using Electrodynamic Ion Funnels and Elevated Drift Gas Pressures. *J. Am. Soc. Mass Spectrom.* **2007**, *18* (7), 1176–1187. https://doi.org/10.1016/j.jasms.2007.03.031.

(4) Kemper, P. R.; Dupuis, N. F.; Bowers, M. T. A New, Higher Resolution, Ion Mobility Mass Spectrometer. *Int. J. Mass Spectrom.* **2009**, *287* (1–3), 46–57. https://doi.org/10.1016/j.ijms.2009.01.012.

(5) Ibrahim, Y. M.; Baker, E. S.; Danielson, W. F.; Norheim, R. V.; Prior, D. C.; Anderson, G. A.; Belov, M. E.; Smith, R. D. Development of a New Ion Mobility Time-of-Flight Mass Spectrometer. *Int. J. Mass Spectrom.* **2015**, *377*, 655–662. https://doi.org/10.1016/j.ijms.2014.07.034.

(6) Ujma, J.; Giles, K.; Morris, M.; Barran, P. E. New High Resolution Ion Mobility Mass Spectrometer Capable of Measurements of Collision Cross Sections from 150 to 520 K. *Anal. Chem.* **2016**, *88* (19), 9469–9478. https://doi.org/10.1021/acs.analchem.6b01812.

(7) Kelly, R. T.; Tolmachev, A. V.; Page, J. S.; Tang, K.; Smith, R. D. The Ion Funnel: Theory, Implementations, and Applications. *Mass Spectrom. Rev.* **2009**, n/a-n/a. https://doi.org/10.1002/mas.20232.

(8) Baker, E. S.; Burnum-Johnson, K. E.; Jacobs, J. M.; Diamond, D. L.; Brown, R. N.; Ibrahim, Y. M.; Orton, D. J.; Piehowski, P. D.; Purdy, D. E.; Moore, R. J.; Danielson, W. F.; Monroe, M. E.; Crowell, K. L.; Slysz, G. W.; Gritsenko, M. A.; Sandoval, J. D.; LaMarche, B. L.; Matzke, M. M.; Webb-Robertson, B.-J. M.; Simons, B. C.; McMahon, B. J.; Bhattacharya, R.; Perkins, J. D.; Carithers, R. L.; Strom, S.; Self, S. G.; Katze, M. G.; Anderson, G. A.; Smith, R. D. Advancing the High Throughput Identification of Liver Fibrosis Protein Signatures Using Multiplexed Ion Mobility Spectrometry. *Mol. Cell. Proteomics* **2014**, *13* (4), 1119–1127. https://doi.org/10.1074/mcp.M113.034595.

(9) Reinecke, T.; Naylor, C. N.; Clowers, B. H. Ion Multiplexing: Maximizing Throughput and Signal to Noise Ratio for Ion Mobility Spectrometry. *TrAC Trends Anal. Chem.* **2019**, *116*, 340–345. https://doi.org/10.1016/j.trac.2019.03.014.

(10) Wojcik, R.; Nagy, G.; Attah, Isaac. K.; Webb, I. K.; Garimella, S. V. B.; Weitz, K. K.; Hollerbach, A.; Monroe, M. E.; Ligare, M. R.; Nielson, F. F.; Norheim, R. V.; Renslow, R. S.; Metz, T. O.; Ibrahim, Y. M.; Smith, R. D. SLIM Ultrahigh Resolution Ion Mobility Spectrometry Separations of Isotopologues and Isotopomers Reveal Mobility Shifts Due to Mass Distribution Changes. *Anal. Chem.* **2019**, *91* (18), 11952–11962. https://doi.org/10.1021/acs.analchem.9b02808.

(11) Giles, K.; Ujma, J.; Wildgoose, J.; Pringle, S.; Richardson, K.; Langridge, D.; Green, M. A Cyclic Ion Mobility-Mass Spectrometry System. *Anal. Chem.* **2019**, *91* (13), 8564–8573. https://doi.org/10.1021/acs.analchem.9b01838.

(12) Shvartsburg, A. A.; Smith, R. D. Fundamentals of Traveling Wave Ion Mobility Spectrometry. *Anal. Chem.* **2008**, *80* (24), 9689–9699. https://doi.org/10.1021/ac8016295.
(13) Pringle, S. D.; Giles, K.; Wildgoose, J. L.; Williams, J. P.; Slade, S. E.; Thalassinos, K.; Bateman, R. H.; Bowers, M. T.; Scrivens, J. H. An Investigation of the Mobility Separation of Some Peptide and Protein Ions Using a New Hybrid Quadrupole/Travelling Wave IMS/Oa-ToF Instrument. *Int. J. Mass Spectrom.* **2007**, *261* (1), 1–12. https://doi.org/10.1016/j.ijms.2006.07.021.
(14) Campuzano, I. D. G.; Giles, K. Historical, Current and Future Developments of Travelling Wave Ion Mobility Mass Spectrometry: A Personal Perspective. *TrAC Trends Anal. Chem.* **2019**, *120*, 115620. https://doi.org/10.1016/j.trac.2019.115620.
(15) Gabelica, V.; Marklund, E. Fundamentals of Ion Mobility Spectrometry. *Curr. Opin. Chem. Biol.* **2018**, *42*, 51–59. https://doi.org/10.1016/j.cbpa.2017.10.022.
(16) Koeniger, S. L.; Merenbloom, S. I.; Valentine, S. J.; Jarrold, M. F.; Udseth, H. R.; Smith, R. D.; Clemmer, D. E. An IMS−IMS Analogue of MS−MS. *Anal. Chem.* **2006**, *78* (12), 4161–4174. https://doi.org/10.1021/ac051060w.
(17) Merenbloom, S. I.; Koeniger, S. L.; Valentine, S. J.; Plasencia, M. D.; Clemmer, D. E. IMS−IMS and IMS−IMS−IMS/MS for Separating Peptide and Protein Fragment Ions. *Anal. Chem.* **2006**, *78* (8), 2802–2809. https://doi.org/10.1021/ac052208e.
(18) Kurulugama, R. T.; Nachtigall, F. M.; Lee, S.; Valentine, S. J.; Clemmer, D. E. Overtone Mobility Spectrometry: Part 1. Experimental Observations. *J. Am. Soc. Mass Spectrom.* **2009**, *20* (5), 729–737. https://doi.org/10.1016/j.jasms.2008.11.022.
(19) Zercher, Ben. Enduring or Ephemeral.
(20) Allen, S. J.; Eaton, R. M.; Bush, M. F. Structural Dynamics of Native-Like Ions in the Gas Phase: Results from Tandem Ion Mobility of Cytochrome. *Anal. Chem.* **2017**, *89* (14), 7527–7534. https://doi.org/10.1021/acs.analchem.7b01234.
(21) Zhang, X.; Garimella, S. V. B.; Prost, S. A.; Webb, I. K.; Chen, T.-C.; Tang, K.; Tolmachev, A. V.; Norheim, R. V.; Baker, E. S.; Anderson, G. A.; Ibrahim, Y. M.; Smith, R. D. Ion Trapping, Storage, and Ejection in Structures for Lossless Ion Manipulations. *Anal. Chem.* **2015**, *87* (12), 6010–6016. https://doi.org/10.1021/acs.analchem.5b00214.
(22) Eaton, R. M.; Allen, S. J.; Bush, M. F. Principles of Ion Selection, Alignment, and Focusing in Tandem Ion Mobility Implemented Using Structures for Lossless Ion Manipulations (SLIM). *J. Am. Soc. Mass Spectrom.* **2019**, *30* (6), 1115–1125. https://doi.org/10.1007/s13361-019-02170-1.
(23) Davidson, K. L.; Oberreit, D. R.; Hogan, C. J.; Bush, M. F. Nonspecific Aggregation in Native Electrokinetic Nanoelectrospray Ionization. *Int. J. Mass Spectrom.* **2017**, *420*, 35–42. https://doi.org/10.1016/j.ijms.2016.09.013.
(24) Eaton, R. M.; Zercher, B.; Wageman, A.; Bush, M. F. A Flexible, Modular Platform for Multidimensional Ion Mobility of Native-like Ions.
(25) Tolmachev, A. V.; Webb, I. K.; Ibrahim, Y. M.; Garimella, S. V. B.; Zhang, X.; Anderson, G. A.; Smith, R. D. Characterization of Ion Dynamics in Structures for Lossless Ion Manipulations. *Anal. Chem.* **2014**, *86* (18), 9162–9168. https://doi.org/10.1021/ac502054p.
(26) Webb, I. K.; Garimella, S. V. B.; Tolmachev, A. V.; Chen, T.-C.; Zhang, X.; Norheim, R. V.; Prost, S. A.; LaMarche, B.; Anderson, G. A.; Ibrahim, Y. M.; Smith, R. D. Experimental Evaluation and Optimization of Structures for Lossless Ion Manipulations

for Ion Mobility Spectrometry with Time-of-Flight Mass Spectrometry. *Anal. Chem.* **2014**, *86* (18), 9169–9176. https://doi.org/10.1021/ac502055e.

(27) Dahl, D. *SIMION Version 8.0*.

(28) Allen, S. J.; Bush, M. F. Radio-Frequency (RF) Confinement in Ion Mobility Mass Spectrometry: Apparent Mobilities and Effective Temperatures. *J. Am. Soc. Mass Spectrom.* **2016**, *27*, 2054–2063. https://doi.org/10.1007/s13361-016-1479-9.

(29) May, J. C.; Jurneczko, E.; Stow, S. M.; Kratochvil, I.; Kalkhof, S.; McLean, J. A. Conformational Landscapes of Ubiquitin, Cytochrome c, and Myoglobin: Uniform Field Ion Mobility Measurements in Helium and Nitrogen Drift Gas. *Int. J. Mass Spectrom.* **2018**, *427*, 79–90. https://doi.org/10.1016/j.ijms.2017.09.014.

Chapter 4: Development and Evaluation of an Interactive Tool to Compare Ion Mobility Data in Different Drift Gases

4.1 Introduction

Ion mobility (IM) mass spectrometry (MS) is a hybrid technique that has emerged as a complementary tool for structural biology.[1] In IM, ions are separated in a buffer gas under an applied electric field according to their mobility (*K*), which depends on an the size, shape, and charge of the ion. From *K*, one can determine an ion's collision cross section (Ω), which to a first-approximation depends on the rotationally averaged, projected area of the ion-neutral collision pair.[2] Ω values are useful for restraining structural models,[3–5] e.g., the incorporation of IM data into an integrative structural modelling approach within the Rosetta software suite[6] improved the quality of predicted protein structures.[7]

One challenge in the development of integrative modelling approaches arises from the use of two different buffer gases – N_2 and He – in different techniques. As IM samples the ion-neutral collision pair, it follows that Ω values derived from separations in N_2 (Ω_{N2}) and helium (Ω_{He}) will differ, owing not only to intrinsic size differences but also due to longer-range interactions between the ion and neutral.[8,9] One current challenge is that nearly all separations performed on commercial instruments use N_2 gas, whereas computational methods for calculating Ω_{He} values have been more extensively developed.[9] Additionally, many early IM-MS studies of biomolecules measured Ω_{He} values.[10] Although the physical properties of the drift gases might preclude a rigorous relationship between Ω_{He} and Ω_{N2} values,[11] empirical comparisons between Ω_{He} and Ω_{N2} values converted to reduced *K* have exhibited linear correlations.[8,12] This presents the opportunity to convert between the two values, enabling

comparisons between contemporary Ω_{N2} values with both computational and experimental Ω_{He} values.

To this end, we have developed an interactive Jupyter Notebook that converts experimental Ω_{N2} input values to estimated Ω_{He} values (and vice versa) for native-like and denatured protein cations. To convert these values, we first compiled experimental data for protein ions for which Ω_{He} and Ω_{N2} values have been measured on RF-confining drift cells.[12] These values were converted to reciprocal reduced K (K_0^{-1}) using constants from the Mason-Schamp equation[13] represented in SI units,[14] the reduced mass of the ion-neutral collision pair, and charge of the ion. The linear relationship that described the correlation between the reduced K values in each drift gas is then used to convert Ω_{N2} to Ω_{He} values. To evaluate the feasibility of this approach, we used this Jupyter Notebook and the derived relationships to analyze independent data[15] that contained both Ω_{He} and Ω_{N2} values for native-like and denatured protein cations.

4.2 Methods

4.2.1 Data Processing. Data processing was performed using Python in an interactive Jupyter Notebook environment. This notebook is available for download from the Bush Lab Github (github.com/bushgroup). Linear regressions were performed using the SciPy library.[16]

4.3 Results and Discussion

4.3.1 Establishing an Empirical Relationship Between Mobilities in He and N2 Gas. Experimental Ω values were used to establish the relationship between K_0^{-1} values in different drift gases. All Ω values for native-like protein cations and denatured protein cations were

obtained using a low-pressure, RF-confining drift tube.[12] This device uses electrostatic gradients to separate ions and does not require mobility calibration. Two separate classes of analytes were defined: native-like and denatured protein cations. The proteins in the native-like class ranged from 12 kDa (cytochrome *c*) to 801 kDa (GroEL). For the denatured protein cations, proteins ranged in mass from 8 kDa (ubiquitin) to 17kDa (myoglobin). These datasets were obtained from an online database and were cleaned to include only protein ions that had both Ω_{He} and Ω_{N2} values available for a given state. These data are available as .csv files in the github repository in a folder labeled "Cleaned Datasets".

4.3.2 Converting **Ω** *Values to Reduced Mobilities.* To establish the relationship between **Ω** measurements in different drift gases, experimental **Ω** were first converted to K_0 using the Mason-Schamp equation:

$$\Omega = \frac{3e}{16N_0}\sqrt{\frac{2\pi}{\mu k_B T}}\frac{z}{K_0} \tag{4.1}$$

where μ is the reduced mass of the ion-neutral collision pair, k_B is the Boltzmann constant, z is the charge of the ion, e is the unit of elementary charge, T is temperature, and N is Loschmidt's number. Equation 4.1 was rearranged by grouping values that are not unique to the analyte into an A term as follows:

$$\Omega = \frac{Az}{\sqrt{\mu}K_0} \tag{4.2}$$

where:

$$A = \frac{3e}{16N_0}\sqrt{\frac{2\pi}{k_B T}} \tag{4.3}$$

This *A* term has units of $A \cdot s^2 \cdot m^2 \cdot kg^{-0.5}$ when using SI base units.[14] Standard temperature (273.15 K) was used to calculate the *A* term. Using Equation 4.2, the *A* term, reduced mass *u*, and ion charge state *z* were used to convert reported Ω values to K_0 values in both helium and nitrogen ($K_{0,He}$ and $K_{0,N2}$, respectively).

4.3.3 Determining Correlations Between Reciprocal Reduced Mobilities. To determine the correlation of experimental data collected in different drift gases, K_0^{-1} values were plotted and exhibit a linear relationship (Figure 4.1). Independent linear regressions were performed for native-like and denatured protein cations. These relationships can then be used to directly convert observed Ω values by substituting a rearranged form of Equation 4.2:

$$\frac{\Omega\sqrt{\mu}}{Az} = \frac{1}{K_0} \tag{4.4}$$

For native-like protein complexes, this yields the following relationship that can be used to convert observed Ω_{N2} values to effective Ω_{He} values (and vice versa)

$$\text{Effective } \Omega_{He} = \frac{0.432 \cdot \Omega_{N2} \cdot \sqrt{u_{N2}} - 1204.89 \cdot A \cdot z}{\sqrt{u_{He}}} \tag{4.5}$$

Here, 0.432 is a unitless constant, whereas the term 1204.89 has units of $m^2 \cdot s^2 \cdot kg^{-1/2}$, which cancels the combined units of the *A* term and the reduced mass to give an effective Ω_{He} value in m^2. For denatured protein cations, we obtained the following relationship:

$$\text{Effective } \Omega_{He} = \frac{0.359 \cdot \Omega_{N2} \cdot \sqrt{u_{N2}} - 652.57 \cdot A \cdot z}{\sqrt{u_{He}}} \tag{4.6}$$

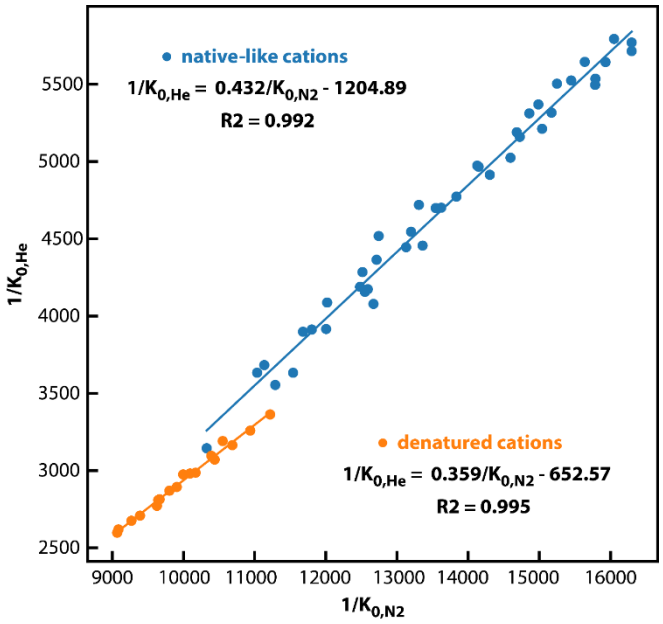

Figure 4.1. Correlations of reduced mobilities from Ω values measured in both helium and nitrogen drift gases. Although the reduced mobilities are often reported with units of $cm^2 \cdot V^{-1} \cdot s^{-1}$, these reduced mobilities use SI base units of $m^2 \cdot V^{-1} \cdot s^{-1}$.

4.3.4 Applying Modeled Relationships to Experimental Data from Other Platforms. To understand the extent to which the relationships described here can describe the relationship between Ω_{N2} and Ω_{He} values measured elsewhere, we sought to analyze independent data that reported Ω values in both helium and nitrogen under similar experimental conditions. These comparisons are limited by the small number of reports of Ω values determined from measurements performed in both drift gases for similar ions under similar experimental conditions.[12] Recently, Ω values for ubiquitin, cytochrome *c*, and myoglobin were reported in both helium and nitrogen.[15] Ω values were reported for a wide range of charge states for each protein ion, encompassing compact native-like structures and extended, highly charged structures generated from aqueous and acidic solution conditions, respectively. The instrument used in this study used a uniform-field drift tube to perform the IM separation, enabling the determination of

K values without calibration. Measured drift times were plotted versus the inverse drift voltage to determine *K*, referred to as the stepped-field method[17] that is analogous to the acquisition method[18] for **Ω** data used to establish the relationships reported here. This set of experimental data will be referred to as the "test data".

Figure 4.2 shows the correlation between K_0^{-1} determined from **Ω** values in the test data. The blue dashed line in Figure 4.2 corresponds to the linear relationship determined from the correlation of database data (Figure 4.1; Equation 4.5). The bottom panel of Figure 4.2 shows the residuals, which were calculated by subtracting the predicted K_0^{-1} from the experimental K_0^{-1}. As shown in the residual plot, the test data consistently appears at larger $K_{0,He}^{-1}$ values than predicted by our model. As K_0^{-1} varies directly with **Ω**, experimental $\mathbf{\Omega}_{He}$ values from the test data are larger than the $\mathbf{\Omega}_{He}$ values predicted by our model. The slope of the linear model does align generally with the slope observed in the test data.

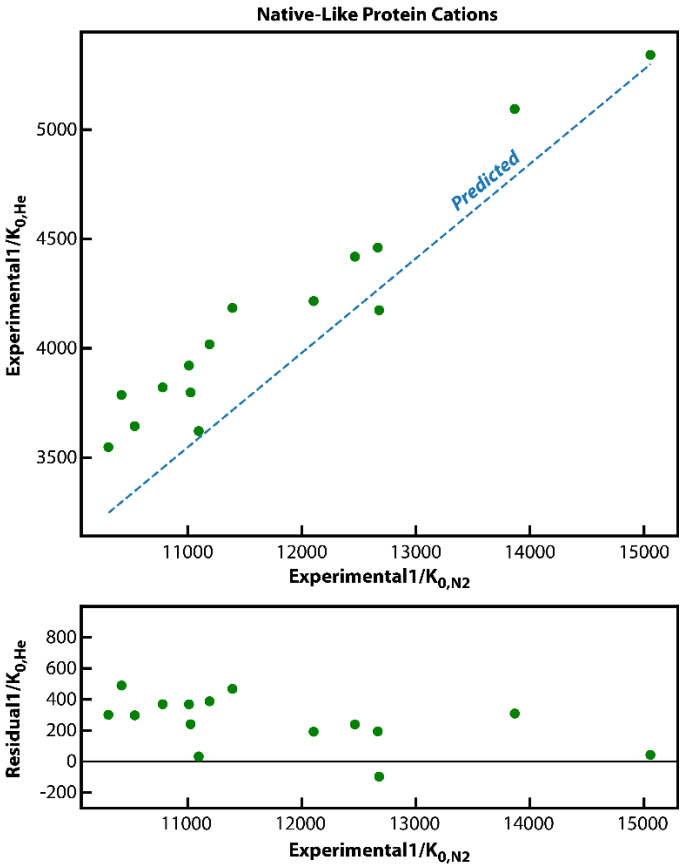

Figure 4.2. (*Top*) Experimental Ω_{N2} and Ω_{He} data for native-like cations were converted to reciprocal reduced mobilities (K_0^{-1}) using Equation 4.4. The dotted line labeled "Predicted" corresponds to the effective $K_{0,He}^{-1}$ predicted by the model for native-like cations shown in Figure 4.1. (*Bottom*) Residuals of the reciprocal reduced mobility were calculated by subtracting the predicted K_0^{-1} from the that value determined from experimental data.

Figure 4.3 shows the K_0^{-1} in nitrogen and helium converted from the experimental Ω values from the test data. The orange dotted line corresponds to the linear relationship of the database data (Figure 4.1; Equation 4.6). The bottom panel shows the residual plot, which is calculated by subtracting the predicted K_0^{-1} value from the experimental value. Once again,

experimental K_0^{-1} values are consistently larger than those predicted by the model, i.e., experimental Ω_{He} values are larger than those effective Ω_{He} values calculated by converting experimental Ω_{N2} values. Even more strikingly than the native-like protein ions, the denatured protein cations in the test data very closely reproduce the slope of the model from database data.

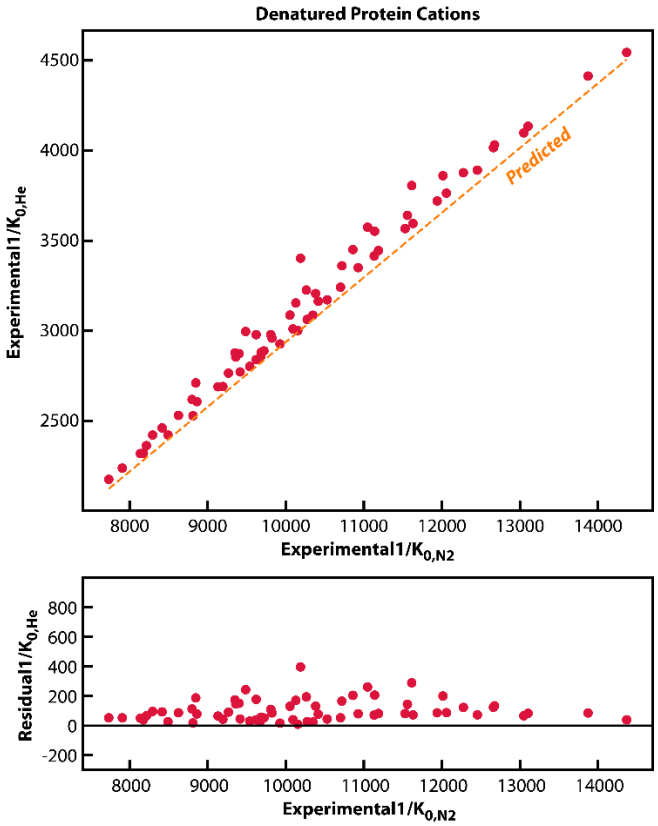

Figure 4.3. (*Top*) Experimental Ω_{N2} and Ω_{He} data for denatured protein cations were converted to reciprocal reduced mobilities using Equation 4.4. The dotted line labeled "Predicted" corresponds to the K_0^{-1} predicted by the model for denatured cations shown in Figure 4.1. (*Bottom*) Residuals of the K_0^{-1} values in helium.

Figure 4.4 shows the relative residuals for both native-like and denatured protein cations from the test data. Relative residuals were calculated as follows

$$Relative\ Residual = \frac{K_{0,He,experimental}^{-1} - K_{0,He,effective}^{-1}}{K_{0,He,effective}^{-1}} \quad (4.7)$$

where *experimental* describes values in the test data converted directly from Ω values and *effective* describes K_0^{-1} values predicted using the models that describe the database data.

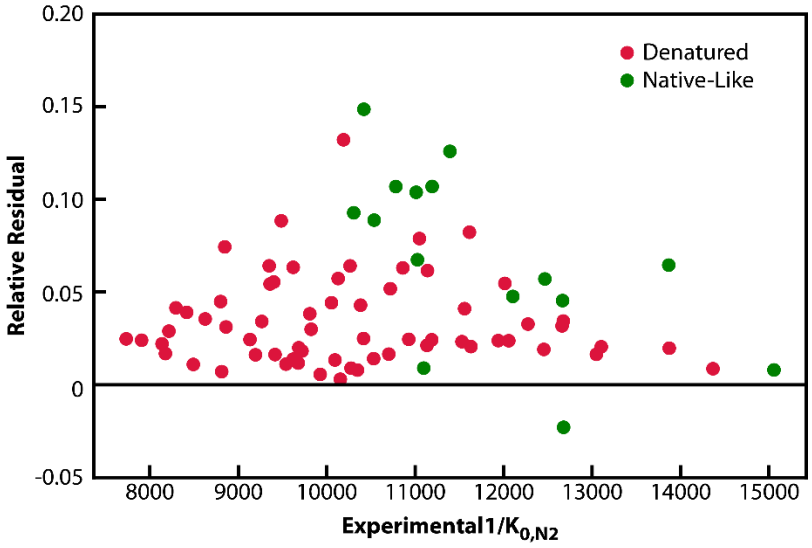

Figure 4.4. Relative residuals for native-like and denatured protein cations as a function of reciprocal reduced mobilities converted from experimental Ω_{N2} values. Relative residuals were calculated using Equation 4.7.

For denatured protein cations, the relative residuals are primarily clustered between 0 and 5%. Native-like values exhibit greater variation, with more data clustered between relative residuals of 5 to 10%. As described in Figures 2 and 3, all but one of the relative residuals for the two classes of ions exhibit positive values, indicating that experimental Ω_{He} values in the test data are larger than those predicted by the model.

The differences between experimental Ω_{He} values and effective Ω_{He} values predicted by our model could arise from a variety of factors. The mass range of the proteins that comprise the test data and database data differs significantly. The database data covers a wide mass range; the majority of Ω values are for proteins and protein complexes with masses exceeding 100 kDa. The test data is comprised only of the native-like charge states of ubiquitin, cytochrome *c*, and myoglobin. In comparison, the database data and test data for denatured protein cations both consist of denatured charge states for only ubiquitin, cytochrome *c*, and myoglobin. Constraining the experimental data by mass range might provide a more robust correlation between Ω_{N2} and Ω_{He} values, as evidenced by the close alignment of the slope of experimental denatured $K_{0,He}^{-1}$ values with the slope of our prediction model.

Additionally, differences between Ω measurements for the test and database data could contribute to the observed effects. For example, the IM separations that generated the test data are much higher resolution than the separations associated with database data. In many cases, test data separations identified multiple conformers that were unresolved in the separations used to produce the database data. Whereas the database data is likely averaging the contributions of these unresolved conformers, the test data contains multiple Ω values for many charge states. In some cases, different numbers of conformations were observed between separations in N_2 and He for the test data; these data were omitted, as the assignment of which conformers correspond to the opposite value in the other drift gas could not be made with confidence. Furthermore, the uniformly positive residuals indicate that there is a systematic bias between the two measurements, which is especially clear in the denatured protein cation dataset (Figure 4.3). Such a systematic bias could arise from methodological differences in measuring *K* values in the two versions of the stepped-field measurements.

4.4 Conclusions and Future Direction

We have developed an interactive notebook implemented using Python that converts experimental Ω_{N2} values to effective Ω_{He} values to facilitate the comparison between experimental and computational data in both drift gases. Although the linear correlation between $K_{0,He}^{-1}$ and $K_{0,N2}^{-1}$ has been reported previously, challenges in the representation of units and uncertainties hindered the broader use of this empirical relationship. We then used our models to predict effective K_0^{-1} values from experimental Ω_{N2} values obtained independently on a separate instrument.[15] These comparisons show that the model is able to roughly reproduce experimental K_0^{-1} values for native-like protein cations (residuals ranged primarily from 5-10%) and more accurately for denatured protein cations (residuals <5%). Further refinement of the database data and identification of biases between measurements could enable more accurate prediction. Although the IM community generally exercises caution in the use of empirical relationships to convert between Ω values in different drift gases, the consistent observation of linear relationship between K_0^{-1} values in the two drift gases indicates that such a comparison is useful. Although this method does not represent a rigorous conversion between Ω values, we anticipate that it will be useful to the broader biomolecular IM community as a first step in understanding the relationships of conformations observed in different drift gases.

4.5 Acknowledgments. Research reported in this publication was supported by the National Institute of General Medical Sciences of the National Institutes of Health through award number R01GM130708 and by the National Science Foundation through award 2203513 from the

Division of Chemistry, with partial co-funding from the Division of Molecular and Cellular Biosciences.

4.6 References

(1) Lanucara, F.; Holman, S. W.; Gray, C. J.; Eyers, C. E. The Power of Ion Mobility-Mass Spectrometry for Structural Characterization and the Study of Conformational Dynamics. *Nat. Chem.* **2014**, *6* (4), 281–294. https://doi.org/10.1038/nchem.1889.

(2) Marklund, E. G.; Degiacomi, M. T.; Robinson, C. V.; Baldwin, A. J.; Benesch, J. L. P. Collision Cross Sections for Structural Proteomics. *Structure* **2015**, *23* (4), 791–799. https://doi.org/10.1016/j.str.2015.02.010.

(3) Eschweiler, J. D.; Farrugia, Mark. A.; Dixit, S. M.; Hausinger, R. P.; Ruotolo, B. T. A Structural Model of the Urease Activation Complex Derived from Ion Mobility-Mass Spectrometry and Integrative Modeling. *Structure* **2018**, *26* (4), 599-606.e3. https://doi.org/10.1016/j.str.2018.03.001.

(4) D'Atri, V.; Porrini, M.; Rosu, F.; Gabelica, V. Linking Molecular Models with Ion Mobility Experiments. Illustration with a Rigid Nucleic Acid Structure: Ion Mobility Calculations and Experiments. *J. Mass Spectrom.* **2015**, *50* (5), 711–726. https://doi.org/10.1002/jms.3590.

(5) Landreh, M.; Sahin, C.; Gault, J.; Sadeghi, S.; Drum, C. L.; Uzdavinys, P.; Drew, D.; Allison, T. M.; Degiacomi, M. T.; Marklund, E. G. Predicting the Shapes of Protein Complexes through Collision Cross Section Measurements and Database Searches. *Anal. Chem.* **2020**, *92* (18), 12297–12303. https://doi.org/10.1021/acs.analchem.0c01940.

(6) Leaver-Fay, A.; Tyka, M.; Lewis, S. M.; Lange, O. F.; Thompson, J.; Jacak, R.; Kaufman, K. W.; Renfrew, P. D.; Smith, C. A.; Sheffler, W.; Davis, I. W.; Cooper, S.; Treuille, A.; Mandell, D. J.; Richter, F.; Ban, Y.-E. A.; Fleishman, S. J.; Corn, J. E.; Kim, D. E.; Lyskov, S.; Berrondo, M.; Mentzer, S.; Popović, Z.; Havranek, J. J.; Karanicolas, J.; Das, R.; Meiler, J.; Kortemme, T.; Gray, J. J.; Kuhlman, B.; Baker, D.; Bradley, P. Rosetta3. In *Methods in Enzymology*; Elsevier, 2011; Vol. 487, pp 545–574. https://doi.org/10.1016/B978-0-12-381270-4.00019-6.

(7) Turzo, S. B. A.; Seffernick, J. T.; Rolland, A. D.; Donor, M. T.; Heinze, S.; Prell, J. S.; Wysocki, V. H.; Lindert, S. Protein Shape Sampled by Ion Mobility Mass Spectrometry Consistently Improves Protein Structure Prediction. *Nat. Commun.* **2022**, *13* (1), 4377. https://doi.org/10.1038/s41467-022-32075-9.

(8) May, J. C.; Goodwin, C. R.; Lareau, N. M.; Leaptrot, K. L.; Morris, C. B.; Kurulugama, R. T.; Mordehai, A.; Klein, C.; Barry, W.; Darland, E.; Overney, G.; Imatani, K.; Stafford, G. C.; Fjeldsted, J. C.; McLean, J. A. Conformational Ordering of Biomolecules in the Gas Phase: Nitrogen Collision Cross Sections Measured on a Prototype High Resolution Drift Tube Ion Mobility-Mass Spectrometer. *Anal. Chem.* **2014**, *86* (4), 2107–2116. https://doi.org/10.1021/ac4038448.

(9) Canzani, D.; Laszlo, K. J.; Bush, M. F. Ion Mobility of Proteins in Nitrogen Gas: Effects of Charge State, Charge Distribution, and Structure. *J. Phys. Chem. A* **2018**, *122* (25), 5625–5634. https://doi.org/10.1021/acs.jpca.8b04474.

(10) Bohrer, B. C.; Merenbloom, S. I.; Koeniger, S. L.; Hilderbrand, A. E.; Clemmer, D. E. Biomolecule Analysis by Ion Mobility Spectrometry. *Annu. Rev. Anal. Chem.* **2008**, *1* (1), 293–327. https://doi.org/10.1146/annurev.anchem.1.031207.113001.

(11) Bleiholder, C.; Johnson, N. R.; Contreras, S.; Wyttenbach, T.; Bowers, M. T. Molecular Structures and Ion Mobility Cross Sections: Analysis of the Effects of He and N_2 Buffer

Gas. *Anal. Chem.* **2015**, *87* (14), 7196–7203. https://doi.org/10.1021/acs.analchem.5b01429.

(12) Bush, M. F.; Hall, Z.; Giles, K.; Hoyes, J.; Robinson, C. V.; Ruotolo, B. T. Collision Cross Sections of Proteins and Their Complexes: A Calibration Framework and Database for Gas-Phase Structural Biology. *Anal. Chem.* **2010**, *82* (22), 9557–9565. https://doi.org/10.1021/ac1022953.

(13) Revercomb, H. E.; Mason, E. A. Theory of Plasma Chromatography/Gaseous Electrophoresis. Review. *Anal. Chem.* **1975**, *47* (7), 970–983. https://doi.org/10.1021/ac60357a043.

(14) Gabelica, V.; Shvartsburg, A. A.; Afonso, C.; Barran, P.; Benesch, J. L. P.; Bleiholder, C.; Bowers, M. T.; Bilbao, A.; Bush, M. F.; Campbell, J. L.; Campuzano, I. D. G.; Causon, T.; Clowers, B. H.; Creaser, C. S.; De Pauw, E.; Far, J.; Fernandez-Lima, F.; Fjeldsted, J. C.; Giles, K.; Groessl, M.; Hogan, C. J.; Hann, S.; Kim, H. I.; Kurulugama, R. T.; May, J. C.; McLean, J. A.; Pagel, K.; Richardson, K.; Ridgeway, M. E.; Rosu, F.; Sobott, F.; Thalassinos, K.; Valentine, S. J.; Wyttenbach, T. Recommendations for Reporting Ion Mobility Mass Spectrometry Measurements. *Mass Spectrom. Rev.* **2019**, *38* (3), 291–320. https://doi.org/10.1002/mas.21585.

(15) May, J. C.; Jurneczko, E.; Stow, S. M.; Kratochvil, I.; Kalkhof, S.; McLean, J. A. Conformational Landscapes of Ubiquitin, Cytochrome c, and Myoglobin: Uniform Field Ion Mobility Measurements in Helium and Nitrogen Drift Gas. *Int. J. Mass Spectrom.* **2018**, *427*, 79–90. https://doi.org/10.1016/j.ijms.2017.09.014.

(16) Virtanen, P.; Gommers, R.; Oliphant, T. E.; Haberland, M.; Reddy, T.; Cournapeau, D.; Burovski, E.; Peterson, P.; Weckesser, W.; Bright, J.; van der Walt, S. J.; Brett, M.; Wilson, J.; Millman, K. J.; Mayorov, N.; Nelson, A. R. J.; Jones, E.; Kern, R.; Larson, E.; Carey, C. J.; Polat, İ.; Feng, Y.; Moore, E. W.; VanderPlas, J.; Laxalde, D.; Perktold, J.; Cimrman, R.; Henriksen, I.; Quintero, E. A.; Harris, C. R.; Archibald, A. M.; Ribeiro, A. H.; Pedregosa, F.; van Mulbregt, P.; SciPy 1.0 Contributors; Vijaykumar, A.; Bardelli, A. P.; Rothberg, A.; Hilboll, A.; Kloeckner, A.; Scopatz, A.; Lee, A.; Rokem, A.; Woods, C. N.; Fulton, C.; Masson, C.; Häggström, C.; Fitzgerald, C.; Nicholson, D. A.; Hagen, D. R.; Pasechnik, D. V.; Olivetti, E.; Martin, E.; Wieser, E.; Silva, F.; Lenders, F.; Wilhelm, F.; Young, G.; Price, G. A.; Ingold, G.-L.; Allen, G. E.; Lee, G. R.; Audren, H.; Probst, I.; Dietrich, J. P.; Silterra, J.; Webber, J. T.; Slavič, J.; Nothman, J.; Buchner, J.; Kulick, J.; Schönberger, J. L.; de Miranda Cardoso, J. V.; Reimer, J.; Harrington, J.; Rodríguez, J. L. C.; Nunez-Iglesias, J.; Kuczynski, J.; Tritz, K.; Thoma, M.; Newville, M.; Kümmerer, M.; Bolingbroke, M.; Tartre, M.; Pak, M.; Smith, N. J.; Nowaczyk, N.; Shebanov, N.; Pavlyk, O.; Brodtkorb, P. A.; Lee, P.; McGibbon, R. T.; Feldbauer, R.; Lewis, S.; Tygier, S.; Sievert, S.; Vigna, S.; Peterson, S.; More, S.; Pudlik, T.; Oshima, T.; Pingel, T. J.; Robitaille, T. P.; Spura, T.; Jones, T. R.; Cera, T.; Leslie, T.; Zito, T.; Krauss, T.; Upadhyay, U.; Halchenko, Y. O.; Vázquez-Baeza, Y. SciPy 1.0: Fundamental Algorithms for Scientific Computing in Python. *Nat. Methods* **2020**, *17* (3), 261–272. https://doi.org/10.1038/s41592-019-0686-2.

(17) Stow, S. M.; Causon, T. J.; Zheng, X.; Kurulugama, R. T.; Mairinger, T.; May, J. C.; Rennie, E. E.; Baker, E. S.; Smith, R. D.; McLean, J. A.; Hann, S.; Fjeldsted, J. C. An Interlaboratory Evaluation of Drift Tube Ion Mobility–Mass Spectrometry Collision Cross Section Measurements. *Anal. Chem.* **2017**, *89* (17), 9048–9055. https://doi.org/10.1021/acs.analchem.7b01729.

(18) Kemper, P. R.; Dupuis, N. F.; Bowers, M. T. A New, Higher Resolution, Ion Mobility Mass Spectrometer. *Int. J. Mass Spectrom.* **2009**, *287* (1–3), 46–57. https://doi.org/10.1016/j.ijms.2009.01.012.

Appendix A: Supporting Information for Chapter 2

A.1 Additional Methods.

A.1.1 Ion Packet Generation. Packets of ions are aligned prior to time-dependent, tandem IM experiments on the first module (^{1}M). The ^{1}M is a tee module, which has an additional path of electrodes that are orthogonal to the collinear electrodes that bisect the module. Following desolvation in the inlet capillary and transfer through two ion funnels, the incident ion beam enters the ^{1}M. During most of the experiment, the incident ion beam is discarded by directing it to a collection electrode at the end of the orthogonal path of the ^{1}M. Immediately prior to each experiment, voltages are modulated at the intersecting paths of electrodes to transmit 12.5 ms of the incident ion beam down the collinear path to the end of the ^{1}M. Here, the ions enter a junction trap.[1]

At the beginning of each experiment, ions are released from the junction trap at the end of the ^{1}M and separated along the first dimensions of ion mobility (^{1}D). Mobility-separated ions of interest are then selected at the ^{7}M and trapped at the interface of the ^{7}M and the ^{8}M. After these trapped ions are released and separated in the ^{2}D, a new packet of ions is prepared at the ^{1}M immediately prior to the next separation to minimize gas-phase ion lifetimes. The next packet of ions is released into the ^{1}D and the sequence is repeated 100-200 times to generate the arrival-time distribution (ATD) from the ^{2}D. Each ^{2}D ATD is the average of three replicate measurements to minimize any contributions originating from synchronization between the ion transport in the MS and the TOF pusher.

A.1.2 Ion Confinement and Junction Trap Conditions. Throughout the entire 12-module array, guard electrodes confine ions laterally, while alternating RF potentials create an effective

potential that repel ions from electrodes.[2] Guard biases and RF waveforms used in these experiments are unchanged from the previous report.[3] A junction trap prevents ions from traversing in the direction of the applied drift field by biasing electrodes at the interface of modules. Ions encounter two junction traps in the course of time-dependent, tandem IM experiments. First, portions of the incident ion beam are aligned in a junction trap on the ^{1}M. Here, the input voltages of the ^{2}M are biased 5 V relative to the output voltage of the ^{1}M. Ions are released into the ^{1}D by raising all potentials on the ^{1}M by 5 V. Mobility-selected ions of interest are then trapped in a junction trap at the interface of the orthogonal paths of ^{7}M and ^{8}M. Here, a voltage bias of +10 V applied to the input of the orthogonal path of ^{8}M prevents ions from entering the ^{2}D.

A.1.3 Apparent Collision Cross Sections. The drift time (t_D) of ions in an IM separation depends on the ion's mobility (K), the length of the separation region (L), and the electric field (E):

$$t_D = \frac{L}{E}\frac{1}{K} \tag{S1}$$

The arrival time of ions at the detector in the ^{2}D is given by the following equation, which sums the residence times of ions in each region of the instrument following the release from the junction trap between the ^{7}M and ^{8}M:

$$t_A = \left(\frac{L_{^{8}M}}{E_{^{8}M}}\frac{1}{K} + \frac{L_{^{2}D}}{E_{^{2}D}}\frac{1}{K} + \frac{L_{CIF}}{E_{CIF}}\frac{1}{K}\right) + t_{MS} \tag{S2}$$

where ^{8}M corresponds to the orthogonal region of the tee module at position 8, ^{2}D corresponds to the collinear paths of the ^{8}M to ^{12}M, *CIF* refers to the circular ion funnel that precedes the mass spectrometer, and t_{MS} refers to the time the ions spend in the mass spectrometer. Factoring out the mobility (K) term and rearranging yields the following equation:

$$K = \left(\frac{L_{^8M}}{E_{^8M}} + \frac{L_{^2D}}{E_{^2D}} + \frac{L_{CIF}}{E_{CIF}}\right)\frac{1}{(t_A - t_{MS})} \quad \text{(S3)}$$

Each value for L and E in the preceding equation depends on the geometry of the instrument or parameters controlled by the analyst. The t_{MS} has been measured for the instrument settings used in these experiments and is expected to be independent of the ion's mobility. Finally, the t_A is determined by representing the measured ATD as a cumulative distribution function and extracting the 50% value. When combining known instrumental parameters, an ion's mobility K can be determined from a ^{2}D arrival time (t_A) at a corresponding ^{2}D drift field ($E_{^2D}$) by the following equation:

$$K = \left(2.718\ cm^2 \cdot V^{-1} + \frac{33.99\ cm}{E_{^2D}}\right)\frac{1}{(t_{A,} - 1)} \quad \text{(S4)}$$

We performed field-dependent measurements in the ^{2}D on the selected charge state of each analyte using the shortest delay time from time-dependent experiments. Specifically, the electric fields of the collinear paths of the ^{8}M through the ^{12}M were varied, while the drift fields of the orthogonal path of the ^{8}M and the circular ion funnel were held constant. ^{2}D ATDs were generated using 5 drift fields ranging from 4.5-6.5 V cm^{-1}. The extracted t_A and the ^{2}D drift field were then used to calculate K using Equation S3, which was then converted to reduced mobility and subsequently **Ω** according to the Mason-Schamp equation.[4] **Ω** values from each drift field measurement were then averaged and are shown in Table S1 with a comparison to literature values. Equation S3 was then used to convert the arrival time axis in time-dependent, tandem IM experiments to apparent **Ω** values for the ^{2}D ATDs generated from time-dependent, tandem IM experiments.

Previously, we determined K values for related experiments[2,5] using field-dependent measurements and the slope of the linear regression of t_A values plotted as a function of the

reciprocal drift voltage. The y-intercept of that linear regression is often referred to as the t_0 and is subtracted from t_A values to obtain drift times that describe the time ions spend in the separation region. However, because the ^{2}D separation in our time-dependent, tandem IM experiment includes several mobility-dependent regions in which drift fields are not typically varied – i.e., the orthogonal path of the ^{8}M and the circular ion funnel – that t_0 value will also depend on mobility. This modified approach allows us to account for mobility-dependent residence times in each region of the ^{2}D separation. This approach could be applied to other IM instruments where field-dependent measurements are used to determine a t_0 value that is mobility-dependent – e.g., constant-field drift tubes followed by refocusing ion funnels.

A.1.4 Kinetic Modeling of Structural Transitions Observed in Time-Dependent, Tandem IM Experiments. We modeled the structural transitions observed in time-dependent, tandem IM experiments for 5+ and 6+ ubiquitin and 7+ cytochrome *c* using tools in the astropy library (The Astropy Project, astropy.org) in Python. We modeled a two-state transition assuming first order kinetics. The two states correspond to a compact initial conformation and final extended conformation, each assigned a single Ω value. The integrated form of the first-order rate law was used to determine relative abundances, which were then used to calculate a median Ω for that two-state population as a function of time. Using a Levenberg Marquardt Least Squares fitter, we parameterized this model using the observed median Ω values at each delay time to determine the rate constant that best explained the observations. Observed median Ω values were obtained by extracting the 50% value of the cumulative distribution function of the apparent Ω distribution.

A.1.5 Converting ΩN2 to ΩHe values. We used data from previous Ω measurements for native-like protein cations[6] where Ω values were measured in both nitrogen (Ω^{N2}) and helium

(Ω^{He}). We first converted Ω values to reduced mobility values using the Mason-Schamp equation:

$$\Omega = \frac{3e}{16N_0}\sqrt{\frac{2\pi}{\mu k_B T}}\frac{z}{K_0} \tag{S5}$$

where μ is the reduced mass of the ion-neutral collision pair, k_B is the Boltzmann constant, z is the charge of the ion, e is the unit of elementary charge, T is temperature, and N is Loschmidt's number. Rearranging Equation S5 by grouping values not unique to the analyte ion yields

$$\Omega = \frac{Az}{\sqrt{\mu}K_0} \tag{S6}$$

where

$$A = \frac{3e}{16N_0}\sqrt{\frac{2\pi}{k_B T}} \tag{S7}$$

Equation S6 was used to convert both Ω^{N2} and Ω^{He} values to reduced mobility. We then performed a linear regression on the correlation of reduced mobility values in helium and nitrogen and obtained the following relationship:

$$\frac{1}{K_0^{He}} = \frac{0.432}{K_0^{N2}} - 1204.89\, V \cdot s \cdot m^{-2} \tag{S8}$$

Substituting Equation S6 into Equation S8 yields

$$\Omega^{He} = \frac{0.432 \cdot \Omega^{N2}\sqrt{\mu^{N2}} - 1204.89 \cdot A \cdot z}{\sqrt{\mu^{He}}} \tag{S9}$$

which we used to convert both individual Ω^{N2} values to Ω^{He} as well as the apparent Ω^{N2} axis from time-dependent measurements (Figure S2). In this relationship, Ω values have units of meters, while the constant value that precedes the A term has the same units as shown in Equation S8.

A.2 Additional Results

A.2.1 Effective Temperatures. To understand potential activation in time-dependent, tandem IM experiments, the ion trajectory software SIMION and a statistical approach were used to estimate the effective translational temperature of ions in the junction trap.7 Each analyte was modeled in SIMION 8.1 (Scientific Instrument Services, Ringoes, NJ) using the HS1 collision model with electric potentials used in time-dependent, tandem IM experiments. The board-to-board spacing was 5.56 mm. Guard voltages that confine ions laterally within the trap were set to +2.5 V relative to central electrodes that create the drift field. The drift field in these simulations was 6.2 V cm–1, which is elevated relative to the drift field used to transmit ions. This is caused by the application of a voltage bias to the input of the orthogonal path of the 7M to prevent unwanted ions from entering the junction trap. The alternating RF waveforms applied to adjacent electrodes had a frequency of 1.257 MHz and an amplitude of 100 Volts peak to peak.

The effective temperatures for each ion are listed in Table S2 and range from 313.2 K for 25+ IgG3 to 346.7 K for 4+ insulin. The small, monomeric proteins exhibited higher effective temperatures than their larger, multimeric counterparts, as higher mobility ions are accelerated more by RF potentials used to confine ions.[7] Ion temperatures in these experiments are higher than in the previous implementation of time-dependent, tandem IM on SLIM in our lab (308 K for 7+ cytochrome *c* vs 325 K in this report).[5] This can be attributed to differences in the instrument geometry and voltage optimizations that occurred when expanding to the 12-module array. Briefly, the drift fields and guard voltages were optimized to maximize trap capacity and ion survival over the range of delay times. These effective temperatures, which were ~15-30 degrees above ambient temperature, are to some extent the result of a tradeoff between measurement sensitivity and ion activation.

*Table S1***.** Effective Translational Temperatures of Each Analyte in the SLIM Trap. Voltage settings and electrode design aligned with instrumental settings.

Analyte	**Mass / kDa**	**n**	**Temperature (K)**
4+ insulin	5.8	1	331.8
5+ ubiquitin	8.6	1	326.6
6+ ubiquitin	8.6	1	333.8
7+ cytochrome *c*	12.0	1	325.6
8+ β-lactoglobulin	18.0	1	323.2
16+ avidin	64	4	319.4
21+ concanavalin A	103	4	315.0
25+ IgG1	150	4	313.2

Table S2. ^{2}D Ω Values of Initial Populations of Ions from Time-Dependent, Tandem IM Experiments

Analyte	**Ω_{N2} from ^{2}D field-dependent measurements (nm^2)**	**Literature Ω_{N2} values (nm2)**
5+ ubiquitin	12.0	12.0[2]
6+ ubiquitin	12.5	12.6[2]
7+ cytochrome *c*	15.8	15.9[6]
8+ β-lactoglobulin	20.5	20.3[6]
16+ avidin	41.9	41.6[6]
21+ concanavalin A	61.3	60.8[6]
25+ IgG3	75.5	74[8,a]

Ω values obtained in ^{2}D field-dependent measurements compared to literature values. Ω values at each ^{2}D drift field were determined using Equation S3 and were averaged.

[a] Estimated from Ω distribution for 25+ IgG3 in the Supporting Information from Reference 8.

*Table S3***.** Rates of Unfolding

Analyte	**Rate Constant (s^{-1})**
7+ cytochrome *c*	0.3
5+ ubiquitin	0.9
6+ ubiquitin	0.8

First-order rates of unfolding calculated for ions that underwent structural evolution in time-dependent, tandem IM experiments.

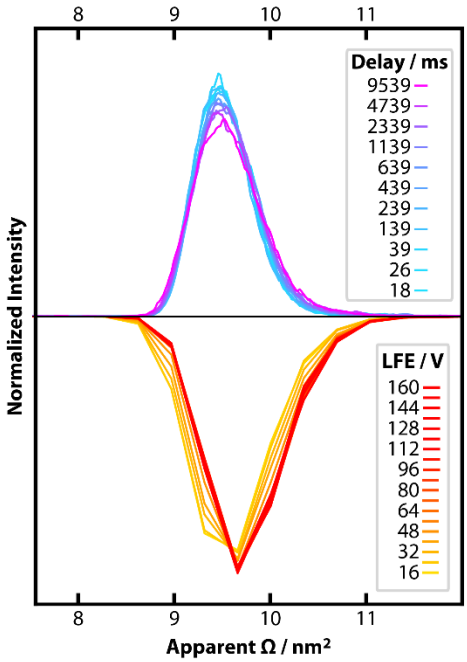

Figure S1. The apparent Ω distributions of 4+ insulin as a function of delay time in time-dependent, tandem IM experiments (*top pane*, positive intensity) and as a function of lab-frame energy in energy-dependent CIU experiments (*bottom pane*, negative intensity).

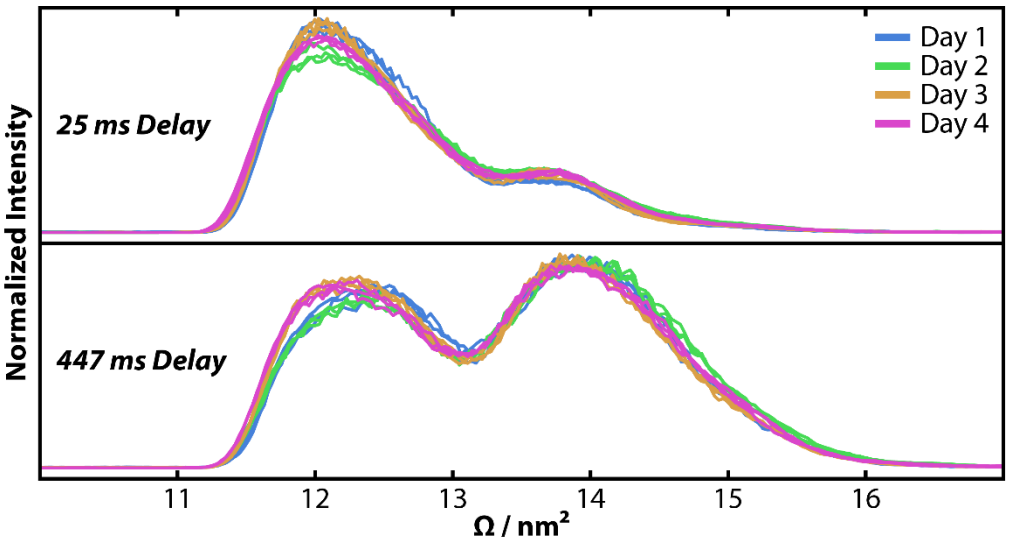

Figure S2. Technical replicates for time-dependent experiments of 6+ ubiquitin were collected on four different days. On each day, three data sets for selected delay times were taken in triplicate. Each triplicate set was averaged prior to plotting.

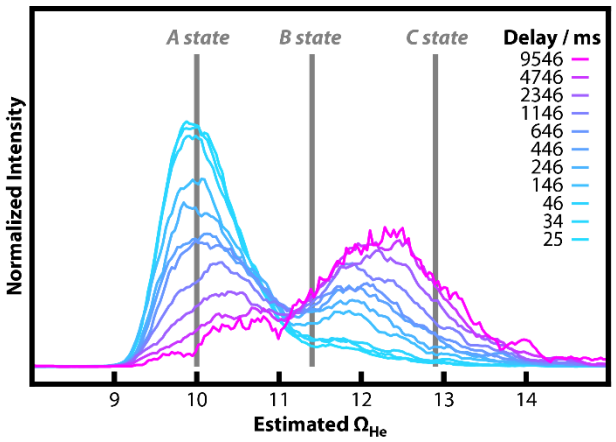

Figure S3. Time-dependent data of 6+ ubiquitin converted from Ω^{N2} values to Ω^{He} values for comparison to Myung et al.[9] Vertical lines are plotted to represent the conformational states observed in the previous study. The A state is the most compact observed in the previous work, while B and C states were defined as partially unfolded conformers. The most compact states in both studies are well-aligned, whereas the more extended state in our time-dependent experiments falls between the two partially unfolded "B" states reported previously.[9] One possibility is that these differences are a consequence of the solution conditions used in the two experiments. 6+ was the lowest charge state of ubiquitin observed directly from electrospray from the solution used in the previous experiment,[9] whereas 5+ was the most intense ubiquitin ion in the present experiments using aqueous 200 mM ammonium acetate. It is possible that a less-stable conformation of ubiquitin (that does not necessarily have a significantly different mobility) preferentially ionizes as the 6+ ion in the present experiments and that conformer is depleted more rapidly. Another possibility is that the faster rate in the current experiments is a consequence of higher effective temperatures, although other experiments suggest higher effective temperatures in the Paul trap relative to these modular instruments.[5]

A.3 Supporting Information References.

(1) Eaton, R. M.; Allen, S. J.; Bush, M. F. Principles of Ion Selection, Alignment, and Focusing in Tandem Ion Mobility Implemented Using Structures for Lossless Ion Manipulations (SLIM). *J. Am. Soc. Mass Spectrom.* **2019**, *30* (6), 1115–1125. https://doi.org/10.1007/s13361-019-02170-1.

(2) Allen, S. J.; Eaton, R. M.; Bush, M. F. Analysis of Native-Like Ions Using Structures for Lossless Ion Manipulations. *Anal. Chem.* **2016**, *88* (18), 9118–9126. https://doi.org/10.1021/acs.analchem.6b02089.

(3) Eaton, R. M.; Zercher, B.; Wageman, A.; Bush, M. F. A Flexible, Modular Platform for Multidimensional Ion Mobility of Native-like Ions.

(4) Gabelica, V.; Afonso, C.; Barran, P. E.; Benesch, J. L. P.; Bleiholder, C.; Bowers, M. T.; Bilbao, A.; Bush, M. F.; Campbell, J. L.; D. G. Campuzano, I.; Causon, T. J.; Clowers, B. H.; Creaser, C.; De Pauw, E.; Far, J.; Fernandez-Lima, F.; Fjeldsted, J. C.; Giles, K.; Groessl, M.; Hogan, Jr., C. J.; Hann, S.; Kim, H. I.; Kurulugama, R. T.; May, J. C.; McLean, J. A.; Pagel, K.; Richardson, K.; Ridgeway, Mark. E.; Rosu, F.; Sobott, F.; Shvartsburg, A. A.; Thalassinos, K.; Valentine, S. J.; Wyttenbach, T. Recommendations for Reporting Ion Mobility Mass Spectrometry Measurements. *Mass Spectrom. Rev.* **2019**, *38*, 291–320. https://doi.org/10.1002/mas.21585.

(5) Allen, S. J.; Eaton, R. M.; Bush, M. F. Structural Dynamics of Native-Like Ions in the Gas Phase: Results from Tandem Ion Mobility of Cytochrome *c*. *Anal. Chem.* **2017**, *89* (14), 7527–7534. https://doi.org/10.1021/acs.analchem.7b01234.

(6) Bush, M. F.; Hall, Z.; Giles, K.; Hoyes, J.; Robinson, C. V.; Ruotolo, B. T. Collision Cross Sections of Proteins and Their Complexes: A Calibration Framework and Database for Gas-Phase Structural Biology. *Anal. Chem.* **2010**, *82* (22), 9557–9565. https://doi.org/10.1021/ac1022953.

(7) Allen, S. J.; Bush, M. F. Radio-Frequency (RF) Confinement in Ion Mobility Mass Spectrometry: Apparent Mobilities and Effective Temperatures. *J. Am. Soc. Mass Spectrom.* **2016**, *27*, 2054–2063. https://doi.org/10.1007/s13361-016-1479-9.

(8) Tian, Y.; Lippens, J. L.; Netirojjanakul, C.; Campuzano, I. D. G.; Ruotolo, B. T. Quantitative Collision-Induced Unfolding Differentiates Model Antibody-Drug Conjugates: Quantitative CIU of ADCs. *Protein Sci.* **2019**, *28* (3), 598–608. https://doi.org/10.1002/pro.3560.

(9) Myung, S.; Badman, E. R.; Lee, Y. J.; Clemmer, D. E. Structural Transitions of Electrosprayed Ubiquitin Ions Stored in an Ion Trap over ~10 Ms to 30 s. *J. Phys. Chem. A* **2002**, *106* (42), 9976–9982. https://doi.org/10.1021/jp0206368.